

Computational Fracture Modeling and Design of Encapsulation-Based Self-Healing Concrete Using XFEM and Cohesive Surface Technique

Doctoral Thesis

Submitted in fulfillment of the requirements for the degree of
Doctor of Philosophy in Computational Mechanics
to the Faculty of Civil Engineering at
Bauhaus University Weimar

Submitted by

M.Sc. John Nabil Mikhail Hanna

from Egypt

Assessors:

Supervisor: Prof. Dr.-Ing. Timon Rabczuk, Bauhaus University Weimar

Prof. Dr.-Ing. habil. Carsten Könke, Bauhaus University Weimar

Prof. dr hab. inż. Mieczysław Kuczma, Poznan University of Technology

Prof. dr. ir. Magd Abdel Wahab, Ghent University

Defense date: 10th November 2022, Weimar

Computermodellierung des Bruchverhaltens und Entwurf von kapselungsbasiertem selbstheilendem Beton mit XFEM und Kohäsionsflächenverfahren

DISSERTATION

Zur Erlangung des akademischen Grades eines
Doktor-Ingenieur
an der Fakultät Bauingenieurwesen
der Bauhaus Universität Weimar

vorgelegt von

M.Sc. John Nabil Mikhail Hanna

aus Ägypten

Gutachter:

Mentor: Prof. Dr.-Ing. Timon Rabczuk, Bauhaus-Universität Weimar

Prof. Dr.-Ing. habil. Carsten Könke, Bauhaus-Universität Weimar

Prof. dr hab. inż. Mieczysław Kuczma, Technische Universität Posen

Prof. dr. ir. Magd Abdel Wahab, Universität Gent

Tag der Disputation: 10. November 2022, Weimar

Abstract

Encapsulation-based self-healing concrete (SHC) is the most promising technique for providing a self-healing mechanism to concrete. This is due to its capacity to heal fractures effectively without human interventions, extending the operational life and lowering maintenance costs. The healing mechanism is created by embedding capsules containing the healing agent inside the concrete. The healing agent will be released once the capsules are fractured and the healing occurs in the vicinity of the damaged part. The healing efficiency of the SHC is still not clear and depends on several factors; in the case of microcapsules SHC the fracture of microcapsules is the most important aspect to release the healing agents and hence heal the cracks. This study contributes to verifying the healing efficiency of SHC and the fracture mechanism of the microcapsules. Extended finite element method (XFEM) is a flexible, and powerful discrete crack method that allows crack propagation without the requirement for re-meshing and has been shown high accuracy for modeling fracture in concrete. In this thesis, a computational fracture modeling approach of Encapsulation-based SHC is proposed based on the XFEM and cohesive surface technique (CS) to study the healing efficiency and the potential of fracture and debonding of the microcapsules or the solidified healing agents from the concrete matrix as well. The concrete matrix and a microcapsule shell both are modeled by the XFEM and combined together by CS. The effects of the healed-crack length, the interfacial fracture properties, and microcapsule size on the load carrying capability and fracture pattern of the SHC have been studied. The obtained results are compared to those obtained from the zero thickness cohesive element approach to demonstrate the significant accuracy and the validity of the proposed simulation. The present fracture simulation is developed to study the influence of the capsular clustering on the fracture mechanism by varying the contact surface area of the CS between the microcapsule shell and the concrete matrix. The proposed fracture simulation is expanded to 3D simulations to validate the 2D computational simulations and to estimate the accuracy difference ratio between 2D and 3D simulations. In addition, a proposed design method is developed to design the size of the microcapsules consideration of a sufficient volume of healing agent to heal the expected crack width. This method is based on the configuration of the unit cell (UC), Representative Volume Element (RVE), Periodic Boundary Conditions (PBC), and associated them to the volume fraction (V_f) and the crack width as variables. The proposed microcapsule design is verified through computational fracture simulations.

Table of Contents

	page
Table of Contents	I
List of Figures	IV
List of Tables.....	IX
1 Introduction	1
1.1 Background and Research Problem Statement	1
1.2 Research Objectives	1
1.3 Methodology	2
1.4 Thesis Organization.....	3
2 Self-Healing Concrete	4
2.1 Introduction	4
2.2 Definitions	4
2.2.1 Intelligent Materials	4
2.2.2 Smart Materials	4
2.2.3 Smart Structures	5
2.2.4 Sensory Structures.....	5
2.3 Concepts of Self-Healing Concrete.....	5
2.3.1 Autogenic Healing of Concrete.....	5
2.3.2 Autonomic Healing of Concrete	7
2.4 Passive and Active Modes of Self-healing.....	9
2.5 Encapsulation Techniques.....	9
2.5.1 Capsule Materials.....	10
2.5.2 Capsule Geometries.....	10
2.5.2.1 Continuous Supply Pipes / Vascular Tubes	11
2.5.2.2 Capillary Tubes	12
2.5.2.3 Tabular Capsules / Cylindrical Tubes (Macro-capsules).....	12
2.5.2.4 Microcapsules.....	13
2.6 Types of Healing Agents.....	14
2.6.1 Bacterial	15
2.6.2 Super Absorbent Polymers (SAP).....	15
2.6.3 Alkali–Silica Solution (Mineral Admixtures)	16
2.6.4 Polymeric (Epoxy, Cyanoacrylate, Polurethane, MMA)	16
2.7 Applications of Self-Healing Concrete	17
3 The eXtended Finite Element Method (XFEM) and Cohesive Surface Technique	19
3.1 Introduction	19
3.2 The eXtended Finite Element Method (XFEM)	19
3.2.1 Partition of Unity Method (PUM).....	19
3.2.2 The concept of enrichment	20
3.2.3 Modeling moving cracks	23

	page
3.2.3.1 Phantom Node Method.....	23
3.2.3.2 Level set method	24
3.2.4 XFEM based on cohesive zone model	26
3.3 The Interfacial Transition Zone (ITZ).....	29
3.3.1 Cohesive contact/surface (CS)	30
3.3.2 Cohesive element	34
4 Proposed Design of Microcapsules	36
4.1 Introduction	36
4.2 Representative Volume Element (RVE)	36
4.3 Unit Cell	36
4.4 Boundary Conditions (BC) types:	37
4.4.1 Dirichlet boundary condition (e.g Displacement)	37
4.4.2 Neumann boundary condition (e.g Pressure)	37
4.4.3 Mixed boundary condition (Combination of Dirichlet and Neuman BC)	37
4.4.4 Periodic Boundary Conditions (PBC)	37
4.4.4.1 Implementation of PBC within FEM	38
4.5 Proposed Design Method of Microcapsules.....	41
4.5.1 Virtual domain of the unit cell	41
4.5.2 The expected crack width of the unit cell.....	42
5 Computational Modeling.....	43
5.1 Introduction	43
5.2 Healing Efficiency.....	43
5.2.1 The effects of the healed crack length.....	43
5.2.1.1 Description of the model	43
5.2.1.2 Study of the mesh size.....	44
5.2.1.3 Parametric studies	44
5.2.1.4 Results and discussion.....	46
5.2.2 The effects of the interfacial fracture properties	48
5.2.2.1 Description of the model	48
5.2.2.2 Study of the mesh size.....	49
5.2.2.3 Parametric studies	49
5.2.2.4 Results and discussion.....	51
5.3 2D Microcapsules Fracture	58
5.3.1 The Effects of interfacial fracture energy.....	58
5.3.1.1 Description of the model	58
5.3.1.2 Parametric studies	59
5.3.1.3 Results and discussion.....	60
5.3.2 Effects of Microcapsule Size and Interfacial Fracture Properties: Verification Study	65

	page
5.3.2.1 Description of the model	65
5.3.2.2 Study of the mesh size	66
5.3.2.3 Parametric studies	67
5.3.2.4 Results and discussion	67
5.4 Effects of Microcapsule Clustering	74
5.4.1 Description of the model	74
5.4.2 Parametric studies	75
5.4.3 Results and discussion	76
5.5 3D Microcapsule Fracture	79
5.5.1 Description of the model	79
5.5.2 Parametric studies	80
5.5.3 Results and discussion	81
5.6 Microcapsules Design	84
5.6.1 Volume Fraction ($V_f = 5\%$)	84
5.6.1.1 Description of the model	84
5.6.1.2 Parametric studies	85
5.6.1.3 Results and discussion	86
5.6.2 Volume Fraction ($V_f = 25\%$)	90
5.6.2.1 Description of the model	90
5.6.2.2 Parametric studies	91
5.6.2.3 Results and discussion	92
6 Conclusions	97
6.1 Summary and Conclusions	97
6.2 Future Work	101
References	102

List of Figures

	page
Figure 2.1: Main mechanisms of autogenous self-healing in concrete [18]	6
Figure 2.2: Automomous self-healing using microcapsules	7
Figure 2.3: Schematic diagram illustrating self-healing mechanisms [18].....	8
Figure 2.4: Active release mode of self-healing concrete (Dry [4]).	9
Figure 2.5: Passive release mode of self-healing concrete by cracking (Dry [4]).	9
Figure 2.6: Replacing adhesive inside continuous supply pipes by vacuum (Dry [4]).	11
Figure 2.7: Release of healing agent via vascular tubes without vacuum pressure system [8].	11
Figure 2.8: capillary tube specimen loading configuration [1].	12
Figure 2.9: Tabular capsules from different materials [42].	13
Figure 2.10: Microcapsule based self-healing techniques. Reaction of encapsulated healing agent due different contact with (A&B) moisture or air or heating (C&D) cementitious matrix (E&F) second component present in the matrix (G,H) second component provided by additional microcapsules [8].	14
Figure 3.1: One opportunity to close the crack in XFEM [55].	22
Figure 3.2: Example of enriched nodes when crack closure is realized by closing the crack .	22
Figure 3.3: Crack with enriched elements [55].	22
Figure 3.4: Enrichment criteria for cracks that are close to a node [55].	23
Figure 3.5: the discontinuous jump function across the crack surfaces; $H(x)$ [58].	23
Figure 3.6: The principle of the phantom node method [55, 58].	24
Figure 3.7: Signed distance function to describe an implicit surface [55].	26
Figure 3.8: Representation of a nonplanar crack in three dimensions by two signed distance functions ϕ and ψ [58].	26
Figure 3.9: Schematic sketch of cohesive zone model (CZM) [70]	27
Figure 3.10: Traction-separation response.	28
Figure 3.11: Centroidal and crack tip locations [58].	29
Figure 3.12: Typical traction-separation law.	30
Figure 3.13: Schematic comparison of cohesive element and cohesive contact approaches[58].	30
Figure 3.14: Adjustment of time incrementation in Abaqus Step module.	33
Figure 3.15: Adjustment of general solution controls in Abaqus Step module.	33
Figure 4.1: Typical periodic boundary conditions and the associated deformation shape [78].	37
Figure 4.2: Virtual domain of RVE with PBC defined by displacements [78].	38
Figure 4.3: Periodic mesh (a) versus non-periodic mesh (b) [78].	39
Figure 4.4: Implementation of PBC within periodic FEM mesh [78].	39
Figure 4.5: Constraint equations of PBC (x direction) in Abaqus interaction module.	40
Figure 4.6: Constraint equations of PBC (y direction) in Abaqus interaction module.	40
Figure 4.7: Geometry dimensions of (a) RVE and (b) UC of the proposed design method of microcapsules.	41
Figure 5.1: Specimens geometry dimensions and modeling techniques (a) virgin concrete sample (b) healed concrete sample.....	44

	page
Figure 5.2: The mesh discretization with three different densities (a) Coarse mesh (5200 elements) (b) Medium mesh (20800 elements) (c) Fine mesh (33050 elements).....	45
Figure 5.3: Healed samples with different healed-crack length L_h ratios (a) L_h 100% ($L_h= 25$ mm) (b) L_h 75% ($L_h= 18.75$ mm) (c) L_h 50% ($L_h= 12.5$ mm) (d) L_h 25% ($L_h= 6.25$ mm). ...	45
Figure 5.4: Force displacement curves from different mesh discretization.	46
Figure 5.5: Crack pattern of virgin sample.....	46
Figure 5.6: Crack pattern of four healed samples with different L_h ratios (a) L_h 100% ($L_h= 25$ mm) (b) L_h 75% ($L_h= 18.75$ mm) (c) L_h 50% ($L_h= 12.5$ mm) (d) L_h 25% ($L_h= 6.25$ mm).....	46
Figure 5.7: Force displacement curve of virgin sample.	47
Figure 5.8: Force displacement curves of four healed samples with different L_h ratios.	47
Figure 5.9: Effects of the L_h ratio to the maximum load of the specimens.....	48
Figure 5.10: Specimens geometry dimensions and modeling techniques.....	49
Figure 5.11: The mesh discretization with three different densities (a) Coarse mesh (42900 elements) (b) Medium mesh (56400 elements) (c) Fine mesh (87750 elements).....	50
Figure 5.12: Healed samples with different healed-crack length L_h ratios (a) L_h 100% ($L_h= 25$ mm) (b) L_h 75% ($L_h= 18.75$ mm) (c) L_h 50% ($L_h= 12.5$ mm) (d) L_h 25% ($L_h= 6.25$ mm).....	50
<i>Figure 5.13: Force displacement curves from different mesh discretization.....</i>	51
Figure 5.14: Force displacement curves of healed-crack length ratio L_h 100% with different itz ratios.	52
Figure 5.15: Force displacement curves of healed-crack length ratio L_h 75% with different itz ratios.	52
Figure 5.16: Force displacement curves of healed-crack length ratio L_h 50% with different itz ratios.	53
Figure 5.17: Force displacement curves of healed-crack length ratio L_h 25% with different itz ratios.	53
Figure 5.18: Force displacement curves of interfacial fracture ratio itz 100% with different L_h ratios.	54
Figure 5.19: Force displacement curves of interfacial fracture ratio itz 75% with different L_h ratio.....	54
Figure 5.20: Force displacement curves of interfacial fracture ratio itz 50% with different L_h ratio.....	55
Figure 5.21: Force displacement curves of interfacial fracture ratio itz 25% with different L_h ratio.....	55
Figure 5.22: Effects of the healed-crack length ratio L_h and the itz percentage on the maximum load.....	56
Figure 5.23: Crack pattern of L_h 100% specimen with different itz ratios. (a) itz = 100% (b) itz = 75% (c) itz = 50% (d) itz = 25%.	57
Figure 5.24: Crack pattern of L_h 75% specimen with different itz ratios. (a) itz = 100% (b) itz = 75% (c) itz = 50% (d) itz = 25%.	57
Figure 5.25: Crack pattern of L_h 50% specimen with different itz ratios. (a) itz = 100% (b) itz = 75% (c) itz = 50% (d) itz = 25%.	57
<i>Figure 5.26: Crack pattern of L_h 25% specimen with different itz ratios. (a) itz = 100% (b) itz = 75% (c) itz = 50% (d) itz = 25%.</i>	57
Figure 5.27: Specimens geometry dimensions and modeling techniques.....	58

	page
Figure 5.28: The meshing of the specimens.....	59
Figure 5.29: Force displacement curves with different itz values.....	60
Figure 5.30: Force displacement curves with different G_f values. (a) σ^* 100% (b) σ^* 75% (c) σ^* 50% (d) σ^* 25% (e) σ^* 10% (f) σ^* 5%.....	61
Figure 5.31: Force displacement curves with different σ^* values. (a) G_f 100% (b) G_f 75% (c) G_f 50% (d) G_f 25% (e) G_f 10% (f) G_f 5%.....	62
Figure 5.32: Crack pattern specimens with different itz values. (a) itz 100% (b) itz 75% (c) itz 50% (d) itz 25% (e) itz 10% (f) itz 5%.....	63
Figure 5.33: Crack pattern of σ^* 100% specimen (6 Mpa) with different G_f ratios. (a) G_f 100% (b) G_f 75% (c) G_f 50% (d) G_f 25% (e) G_f 10% (f) G_f 5%.....	64
Figure 5.34: Crack pattern of σ^* 75% specimen (4.5 Mpa) with different G_f ratios. (a) G_f 100% (b) G_f 75% (c) G_f 50% (d) G_f 25% (e) G_f 10% (f) G_f 5%.....	64
Figure 5.35: Crack pattern of σ^* 50% specimen (3 Mpa) with different G_f ratios. (a) G_f 100% (b) G_f 75% (c) G_f 50% (d) G_f 25% (e) G_f 10% (f) G_f 5%.....	64
Figure 5.36: Crack pattern of σ^* 25% specimen (1.5 Mpa) with different G_f ratios. (a) G_f 100% (b) G_f 75% (c) G_f 50% (d) G_f 25% (e) G_f 10% (f) G_f 5%.....	64
Figure 5.37: Crack pattern of σ^* 10% specimen (0.6 Mpa) with different G_f ratios. (a) G_f 100% (b) G_f 75% (c) G_f 50% (d) G_f 25% (e) G_f 10% (f) G_f 5%.....	64
Figure 5.38: Crack pattern of σ^* 5% specimen (0.3 Mpa) with different G_f ratios. (a) G_f 100% (b) G_f 75% (c) G_f 50% (d) G_f 25% (e) G_f 10% (f) G_f 5%.....	64
Figure 5.39: Specimens geometry dimensions and modeling techniques.....	65
Figure 5.40: Three meshes with different discretization (a) Coarse mesh (5219 elements) (b) Medium mesh (16435 elements) (c) Fine mesh (32217 elements).....	66
Figure 5.41: Damage dissipation energy from different mesh discretization.....	66
Figure 5.42: Samples with different microcapsule core shell thickness ratios, (a) Ratio 1:1 (b) Ratio 5:1 (c) Ratio 10:1 (d) Ratio 15:1.....	67
Figure 5.43: Load displacement curves for microcapsule core-shell ratio 1:1 with different itz values.....	68
Figure 5.44: Load displacement curves for microcapsule core-shell ratio 5:1 with different itz values.....	69
Figure 5.45: Load displacement curves for microcapsule core-shell ratio 10:1 with different itz values.....	69
Figure 5.46: Load displacement curves for microcapsule core-shell ratio 15:1 with different itz values.....	70
Figure 5.47: Effects of itz ratios to the maximum load with different microcapsule core-shell ratios.....	71
Figure 5.48: Crack pattern of microcapsule ratio 1:1 with different itz ratios. (a) itz 10% (b) itz 25% (c) itz 50% (d) itz 75% (e) itz 100%.....	72
Figure 5.49: Crack pattern of microcapsule ratio 5:1 with different itz ratios. (a) itz 10% (b) itz 25% (c) itz 50% (d) itz 75% (e) itz 100%.....	72
Figure 5.50: Crack pattern of microcapsule ratio 10:1 with different itz ratios. (a) itz 10% (b) itz 25% (c) itz 50% (d) itz 75% (e) itz 100%.....	72
Figure 5.51: Crack pattern of microcapsule ratio 15:1 with different itz ratios. (a) itz 10% (b) itz 25% (c) itz 50% (d) itz 75% (e) itz 100%.....	72

	page
Figure 5.52: Specimens geometry dimensions and modeling techniques.....	74
Figure 5.53: The meshing of the specimens.....	75
Figure 5.54: Specimens with different capsular circumferential contact length ratios L_{cs} ratios (a) L_{cs} 100% ($L_{cs}= 6.28$ mm) (b) L_{cs} 75% ($L_{cs}= 4.71$ mm) (c) L_{cs} 50% ($L_{cs}= 3.14$ mm) (d) L_{cs} 25% ($L_{cs}= 1.57$ mm).....	76
Figure 5.55: Load displacement curves for specimens with different L_{cs} ratios.....	77
Figure 5.56: Effects of the L_{cs} ratio on the maximum load of the specimens.....	77
Figure 5.57: <i>Crack pattern of specimens with different L_{cs} ratios. (a) L_{cs} 100% (b) L_{cs} 75% (c) L_{cs} 50% (d) L_{cs} 25% (e) L_{cs} 0%.</i>	78
Figure 5.58: Specimens geometry dimensions and modeling techniques.....	79
Figure 5.59: The meshing of the specimens.....	80
Figure 5.60: Load displacement curves for strong interface in 3D and 2D.	81
Figure 5.61: Load displacement curves for weak interface in 3D and 2D.....	82
Figure 5.62: Crack pattern specimens with strong interface in 3D.....	83
Figure 5.63: Crack pattern specimens with weak interface in 3D.....	83
Figure 5.64: RVE geometry dimensions and modeling techniques.	84
Figure 5.65: The mesh discretization with different microcapsule core-shell ratios, (a) Ratio 1:1 (b) Ratio 5:1 (c) Ratio 10:1 (d) Ratio 15:1.....	85
Figure 5.66: Load displacement curves for microcapsule core-shell ratio 1:1 with different itz values.....	86
Figure 5.67: Load displacement curves for microcapsule core-shell ratio 5:1 with different itz values.....	87
Figure 5.68: Load displacement curves for microcapsule core-shell ratio 10:1 with different itz values.....	87
Figure 5.69: Load displacement curves for microcapsule core-shell ratio 15:1 with different itz values.....	88
Figure 5.70: Effects of itz ratios to the maximum load with different microcapsule core-shell ratios.	88
Figure 5.71: <i>Crack pattern of microcapsule ratio 1:1 with different itz ratios. (a) itz 10% (b) itz 25% (c) itz 50% (d) itz 75% (e) itz 100%.</i>	89
Figure 5.72: <i>Crack pattern of microcapsule ratio 5:1 with different itz ratios. (a) itz 10% (b) itz 25% (c) itz 50% (d) itz 75% (e) itz 100%.</i>	90
Figure 5.73: <i>Crack pattern of microcapsule ratio 10:1 with different itz ratios. (a) itz 10% (b) itz 25% (c) itz 50% (d) itz 75% (e) itz 100%.</i>	90
Figure 5.74: <i>Crack pattern of microcapsule ratio 15:1 with different itz ratios. (a) itz 10% (b) itz 25% (c) itz 50% (d) itz 75% (e) itz 100%.</i>	90
Figure 5.75: RVE geometry dimensions and modeling techniques.	91
Figure 5.76: The mesh discretization with different microcapsule core-shell ratios, (a) Ratio 1:1 (b) Ratio 5:1 (c) Ratio 10:1 (d) Ratio 15:1.....	91
Figure 5.77: Load displacement curves for microcapsule core-shell ratio 1:1 with different itz values.....	92
Figure 5.78: Load displacement curves for microcapsule core-shell ratio 5:1 with different itz values.....	93

	page
Figure 5.79: Load displacement curves for microcapsule core-shell ratio 10:1 with different itz values.....	93
Figure 5.80: Load displacement curves for microcapsule core-shell ratio 15:1 with different itz values.....	94
Figure 5.81: Effects of itz ratios to the maximum load with different microcapsule core-shell ratios.	94
Figure 5.82: <i>Crack pattern of microcapsule ratio 1:1 with different itz ratios. (a) itz 10% (b) itz 25% (c) itz 50% (d) itz 75% (e) itz 100%.</i>	96
Figure 5.83: <i>Crack pattern of microcapsule ratio 5:1 with different itz ratios. (a) itz 10% (b) itz 25% (c) itz 50% (d) itz 75% (e) itz 100%.</i>	96
Figure 5.84: <i>Crack pattern of microcapsule ratio 10:1 with different itz ratios. (a) itz 10% (b) itz 25% (c) itz 50% (d) itz 75% (e) itz 100%.</i>	96
Figure 5.85: <i>Crack pattern of microcapsule ratio 15:1 with different itz ratios. (a) itz 10% (b) itz 25% (c) itz 50% (d) itz 75% (e) itz 100%.</i>	96

List of Tables

	page
Table 3.1: Comparison between cohesive element and cohesive surface approaches.	35
Table 5.1: The material properties.	44
Table 5.2: The material properties.	49
Table 5.3: The material properties.	59
Table 5.4: The imaterial properties.	65
Table 5.5: The material properties.	75
Table 5.6: The material properties.	80
Table 5.7: The imaterial properties.	85

1 Introduction

1.1 Background and Research Problem Statement

Concrete is the most-used building material in the world, with about 2.5 tons per person per year and is made especially attractive due to its cheap price. Concrete structures have been built since the discovery of Portland cement in the mid-nineteenth century. It is a quasi-brittle material that is strong in compression but weak in tension. That is why the reinforcement is usually used with it for construction [1]. However, its weakest point is that its subject to cracking and deterioration with time, and the renovation of concrete buildings is costly, especially for infrastructure maintenance, which is not easily accessible. Recently, the biological systems have become the inspiration for material scientists. This fundamental change in material design philosophy has resulted in the creation of ‘smart’ materials, including self-healing materials. There are many strategies and techniques for self-healing concrete and they are classified in different ways. However the encapsulation-based self-healing concrete has lately received much interest because of its capacity to effectively heal fractures without human interventions, extending the operational life and lowering maintenance costs. Once the propagating cracks hit capsules shell releasing the healing agents to heal the cracks in the vicinity of the damaged part. Because of this, SHC has great perspectives for infrastructures exposed to water and corrosion such as tunnels and bridges. Several experimental studies have been carried out in the literature to investigate the fracture of the capsules and healing capability of the capsules. These studies have revealed that the bond between the capsule shell and the cement matrix isn't always perfect and the efficiency of healing depends on the fracture of microcapsules and releasing of the healing agent in order to heal the cracks. Computational modeling of self-healing concrete is still the earlier stages and most of them used zero thickness cohesive element approach. However that approach has significant drawbacks such as introducing artificial compliance and mesh dependency. Extended finite element method (XFEM) is a promising, flexible, and powerful discrete crack method and it allows crack propagation without the requirement for re-meshing [2]. XFEM has been shown high accuracy for modeling fracture in concrete [3].

1.2 Research Objectives

The aim of this thesis is to develop a computational fracture modeling approach to study the fracture mechanism of encapsulation-based self-healing concrete using XFEM and cohesive surface techniques. In addition, it will study the physical phenomena that are challenging and difficult to investigate experimentally, which led to the innovative studies of capsular clustering and microcapsules design. To achieve the overall aims of this study, the following objectives are defined as follows:

- a. Study the healing efficiency of self-healing concrete on the loading capacity of healed specimens. Also investigate the effects of partial healed cracks, and the interfacial bond between the concrete and the solidified healing agents on the overall healing efficiency.
- b. Study the interaction between the microcapsule and the concrete in order to determine the factors which cause fracture and debonding of the microcapsule from the concrete matrix such as the interfacial strength, the interfacial fracture energy, and the microcapsule size.

- c. Perform a comparative study between the results obtained from the proposed modeling techniques and the most used modeling approach in the literature; zero thickness cohesive element approach in order to illustrate significant accuracy of the proposed modeling. That is considered also one of the key novelties from this research.
- d. Develop a computational modeling approach to study the capsular clustering effects on the fracture process of microcapsule self-healing concrete. That is also considered to be another key novelty of this research.
- e. Extend the proposed modeling to 3D simulation in order to investigate and validate the 2D simulations which are less computationally expensive. In addition, to estimate an accuracy reduction factor between 3D and 2D simulations.
- f. Develop a design method for microcapsules to design its size with the consideration of the sufficient volume of healing agent to heal a specific crack width. This is also regarded as a significant innovation from this study.

1.3 Methodology

Several computational techniques are employed in this thesis in order to perform computational fracture modeling of encapsulation-based self-healing concrete and study the healing efficiency, the fracture mechanism, and microcapsule design. The computational techniques and the methodology of the research are described in the following:

- i. The proposed fracture modeling approach for studying the healing efficiency of self-healing concrete built in the commercial software Abaqus. In case assuming that crack propagating only inside the solidified healing agent, 2D specimens consist of two parts; a concrete matrix modeled by FEM and a solidified healing agent is modeled by the eXtended Finite Element Method (XFEM) and tied together by tie constraints. In order to investigate where the crack will initiate, 2D specimens consists of two parts; a concrete matrix and a solidified healing agent. Both are modeled by XFEM and combined together by cohesive surface technique (CS).
- ii. The proposed modeling approach for studying the fracture of the encapsulation self-healing concrete built in Abaqus. 2D specimens consist of two parts; a concrete matrix and a microcapsule shell- both are modeled by the XFEM and combined together by CS.
- iii. The previous proposed fracture modeling approach is developed to study the capsular clustering effect by varying the contact surface area of the CS between the microcapsule shell and the concrete matrix.
- iv. The proposed microcapsule fracture modeling simulations is expanded to 3D simulations. In addition the obtained results are compared with the results of obtained from 2D simulations in order to validate the 2D computational simulations and to estimate the accuracy difference ratio between 2D and 3D simulations.
- v. The proposed design method is developed to design the microcapsules size by considering a sufficient volume of healing agent to heal a specific crack width. It is based on the configuration of the unit cell (UC), Representative Volume Element (RVE), Periodic Boundary Conditions (PBC), and associated them to the volume fraction (V_f) and the crack width as variables. In addition, the validation of this proposed design is performed with the previous proposed computational fracture simulations.

1.4 Thesis Organization

This thesis consists of six chapters presented as follows:

Chapter 1: Introduction

This is the introductory chapter and provides a comprehensive summary of the research work done in this thesis. The background, objectives, the methodology of the research are presented in this chapter.

Chapter 2: Self-Healing Concrete

In this chapter, the development, definitions, concepts, and techniques of self-healing concrete are reviewed in detail. The encapsulation techniques including the types of capsules and healing agents are classified. Additionally, applications of self-healing concrete in practical projects are discussed.

Chapter 3: The eXtended Finite Element Method (XFEM) and Cohesive Surface Technique

This chapter addresses the theoretical aspects and formulation of the extended finite element method (XFEM) that allows crack propagation without requiring re-meshing. Partition of Unity Method (PUM), the concept of enrichment, modeling moving cracks based on phantom mode method and level set method are included in this chapter. The cohesive zone model, the interfacial transition zone (ITZ) including the cohesive surface technique and cohesive element approach are reviewed. General comparison between the cohesive element and cohesive surface approaches is summarized. In addition to the implementations of these techniques in Abaqus software are discussed in detail.

Chapter 4: Proposed Design of Microcapsules

In this chapter, a simple proposed design method is developed to design the microcapsules size consideration of the sufficient volume of healing agent to heal the expected crack width. It is based on the configuration of the unit cell (UC), Representative Volume Element (RVE), Periodic Boundary Conditions (PBC), and associates them with the volume fraction (V_f) and the crack width as variables. Additionally, a short review about the used techniques in this proposed design method is presented, including the implementation of PBC within FEM.

Chapter 5: Computational Modeling

This chapter presents the proposed computational modeling and simulations to study the healing efficiency and the potential of fracture and debonding of the microcapsules and the solidified healing agents as well. The accuracy of these proposed techniques are illustrated by a comparative study with the zero thickness cohesive elements (CIE). The effects of microcapsule clustering on the fractured microcapsule are performed computationally. 3D computational simulations are performed and the obtained results are compared with the results of obtained from 2D simulations in previous sections to estimate the difference in accuracy. In addition to computational simulations of the proposed microcapsule design with different volume fraction (V_f) are performed and validated.

Chapter 6: Conclusions

In this chapter, a short review of the entire research work in this thesis is given. Conclusions from the entire computational simulations are presented and the engineering contributions are emphasized. Finally, some prospective future research works are demonstrated.

2 Self-Healing Concrete

2.1 Introduction

Although numerous studies on self-healing materials are focused on polymers and polymer composites for high-tech applications in space and aeroplane areas, the idea of self-healing function was first explored in the field of civil engineering field with the study by Dry [4] for cementitious materials. However, in recent years, as the concept of sustainable materials has become increasingly popular, self-healing concrete has emerged as an appealing topic as a potential solution to the sustainability challenge. In this chapter, the development, definitions, concepts, and techniques of the self-healing concrete are reviewed in detail. The encapsulation techniques, including the types of capsules and healing agents, are outlined and classified. In addition, applications of self-healing concrete in practical projects are discussed.

2.2 Definitions

Self-healing concrete is mostly defined as the ability of concrete to heal or repair its cracks automatically and autonomously without any external intervention [1]. A number of terms, such as intelligent materials, smart materials, smart structures, and sensory structures have been used in the literature for this new field of self-healing materials. There is some confusion regarding the definition of these terms within the literature. However, short clarifications on these definitions are provided as the following:

2.2.1 Intelligent Materials

Intelligent materials are materials that “incorporate the notion of information as well as physical index such as strength and durability” [5]. This higher level function or “intelligence” is achieved through the systematic corporation of various individual functions. As a result, intelligent materials exhibit a self-control capability whereby they are not only able to sense and respond to various external stimuli but also to conduct this response in a regulated manner. This is analogous to the behaviour exhibited by many natural materials such as skin, bone, and tendons [1].

2.2.2 Smart Materials

Smart materials are engineered materials that are able to provide a unique beneficial response when a particular change occurs in its surrounding environment [6]. Examples of smart materials include piezoelectric materials, magnetostrictive materials, shape memory materials, temperature-responsive polymers that are able to change color with temperature, and smart gels that are able to shrink or swell by factors of up to 1000 in response to chemical or physical stimuli. The difference between a smart material and an intelligent material is therefore defined by the degree to which the material can gather information, process this information, and react accordingly [1].

2.2.3 Smart Structures

Smart structures differ from smart materials in that they are engineered composites of conventional materials, which exhibit sensing and actuation properties, due to the properties of the individual components. Many self-healing materials fall into the category of smart structures, since they contain encapsulated healing agents that are released when damage occurs, thereby “healing” the “injury” and increasing the materials’ functional life. Self-healing studies have been performed on polymers, coatings, composites, and concrete; however, all these “structures” rely on previous knowledge of the damage mechanisms to which they are susceptible, and are therefore classed as smart rather than intelligent [1]. Further details of Self-healing concrete will be discussed in section 2.3.

2.2.4 Sensory Structures

Sensory structures have sensing capabilities but lack actuating properties. Examples of sensory structures include smart brick, which are able to monitor temperature, vibration, and movements within buildings; smart optical fibers, which are able to sense undesirable chemicals, moisture, and strain; and smart paints, which contain silicon-microsphere sensors, and are able to monitor their condition and protection effectiveness [1].

2.3 Concepts of Self-Healing Concrete

There are many strategies and techniques for self-healing concrete and they are classified in different ways. Two interesting studies comparing different healing techniques were carried out in TU Delft [7] and in Ghent University [8]. Also, recently there are many review studies done to summarize the different strategies and techniques of self-healing concrete such as [9, 10]. But all of them are based on only two main concepts of self-healing, namely autogenous and autonomous self-healing.

2.3.1 Autogenic Healing of Concrete

If the healing properties of a material are generic to that material, then the material could potentially be classed as a smart material, and the healing process is termed autogenic healing. It could also happen without the need of any additional healing agents, because cementitious materials have a natural autogenic potential to self-repair, as rehydrating a concrete specimen in water can initiate the hydration process by reacting with pockets of dehydrated cement in the matrix. The autogenic healing of cementitious materials is a natural phenomenon that has been known about for many years. This effect is generally acknowledged as one of the reasons as to why so many old buildings and structures have survived for so long with limited servicing and maintenance. This contributes to the unexpected longevity of many old bridges in Amsterdam [11]. It is believed that this longevity is due to the high levels of chalk or calcium in the cement of that area. In the presence of water, this calcium is believed to dissolve and then deposit in cracks, thus partially healing them and hindering their propagation. Recently, the autogenic healing of microcracks has been the suggested reason for the reduction in the diffusion coefficient of concrete marine structures with time. However, the durability benefit that the self-healing of microcracks affords is reduced for non-

submerged concrete structures. Periodic “wetting” of structures may improve this situation; however, such a process is expensive and generally impracticable for most situations [1]. The primary causes of autogenous self-healing are considered to be based on chemical, physical, and mechanical processes. The main processes are (i) swelling and hydration of cement pastes, (ii) precipitation of calcium carbonate crystals, and (iii) blockage of flow paths due to deposition of water impurities or movement of concrete fragments that detach during the cracking process [12], see Figure 2.1. Many researchers have investigated this phenomenon. Investigation of the effect of the degree of damage on the self-healing ability of normal strength and high strength concrete [13]. Examination of the effect of temperature on permeability and self-healing of cracked concrete [14]. Consideration of the effect of autogenous healing on engineered cementitious composites (ECCs) [15]. Examination of the efficacy of autogenous healing on strength recovery of complete cured concrete beams exposed to rapid freeze/thaw cycles [16], in that paper it concluded that only a 4–5% recovery of compressive strength by means of autogenous healing was possible. However, the greatest potential for autogenous healing exists in early age concrete [17].

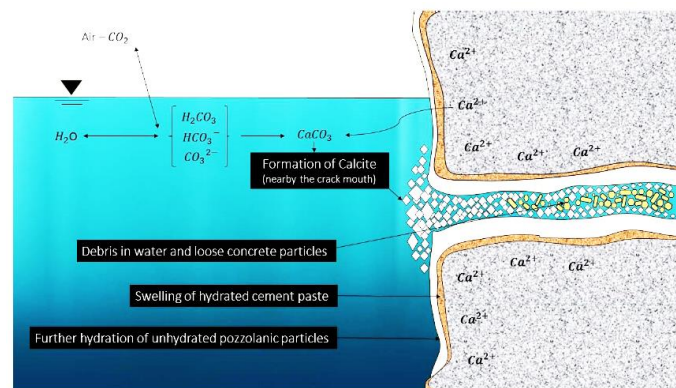


Figure 2.1: Main mechanisms of autogenous self-healing in concrete [18]

Researchers have found out that autogenous healing is limited to small cracks and is only effective when water is available and is difficult to control [19]. The limit of healable crack width by autogenous healing was found to be 200 μm and 300 μm . Several examinations were undertaken to investigate the autogenous healing in concrete, which tried to resolve the problem of the limitation of healable crack widths. As a suggested resolution, they proposed to apply compressive forces [20]. Also, others proposed using engineered cementitious composites (ECC) containing synthetic fibers, such as polypropylene (PP) and polyvinyl alcohol (PVA), to restrain crack width [20]. Other alternatives were proposed to activate hydration by adding supplement water using superabsorbent polymers (SAP) in the concrete mixture, which can store and supply moisture over a longer period of time. However, when water is released from SAP, pores or voids are formed in concrete that become weak links in the matrix. Cracks may even propagate through them during the service life of the structure [1]. Other studies are attempted at using supplementary cementitious materials, such as fly ash and blast furnace slag, to stimulate autogenous healing. Materials like fly ash and slag hydrate at a slower rate than cement, and therefore, unhydrated particles of such minerals promote autogenous healing at the later stage of concrete. However, the disadvantage of this approach is that the healing agent is consumed in the process and may not be available for further hydration at a later stage [1]. The concept of using bacteria spores to mediate the healing process by precipitation of calcium carbonate was proposed by Jonkers [21]. Although the bacteria initiated the precipitation and deposition of calcium carbonate at the crack faces, but

when added to the fresh concrete mix, they did not survive for a long period due to two reasons: the strongly alkaline environment of the concrete mixture and the shrinkage of pores due to cement hydration. It is worth to mention that aforementioned modifications of autogenous self-healing known as well as improved autogenous self-healing [18]. In summary, autogenous healing mechanism has several inherent weaknesses, including (1) dependency on age of concrete; (2) need for a long-lasting internal source of water; (3) survival of bacteria for carbonate precipitation; and (4) need for limitation on the width of the crack that can be healed [1].

2.3.2 Autonomic Healing of Concrete

If the self-healing function is created by embedding self-healing units consisting of the container; like capsule or tube containing the healing agent in the host concrete and the healing agent released as a result of cracking. Hence the healing occurs in the vicinity of the damaged part, then healing process is termed autonomic healing. The concept of autonomic healing in concrete was originally proposed for cementitious materials by Dry [22] using hollow glass tubes as containers and methyl methacrylate as a healing agent. Recent intense research has been drawn to an autonomous type of self-healing method using microcapsules for more accurate healing location and better healing capabilities [23]. The healing agents are placed inside discrete microcapsules embedded in the substrate material. Approaching cracks break the capsule shell to release the healing agent and hence the healing occurs in the vicinity of the damaged part, see Figure 2.2. The healing is more localized in comparison to the uniform hydration of autogeneous healing. Various healing agents, such as polymer, bacteria, sodium silicate, and various capsule shells materials, e.g. gelatin, silicon and glass, have been developed and tested, aiming to extend the life of the healing agent, accelerate the reaction after cracking and improve the healing capability [24, 25].

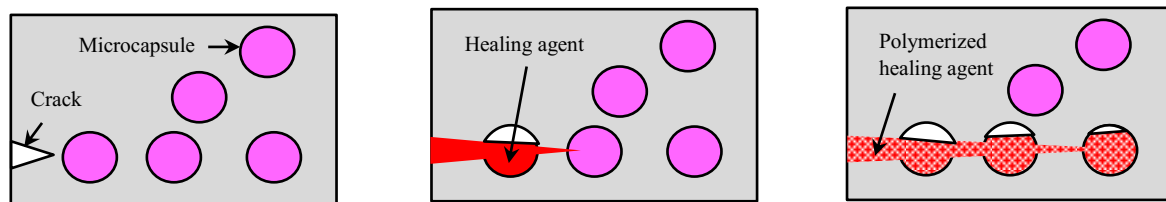


Figure 2.2: Automomous self-healing using microcapsules

While the autogenous healing relies on the presence of water, and bacteria based autogenous healing has problems of bacteria survival and a low recovered strength of the repaired concrete, the microcapsule self-healing technique using polymer healing agents appear to be the most promising due to improved high healing capability [8, 26]. Another technique based on autonomic healing concept is called vascular self-healing which mimics the vascular network system in the human body. A network of tubes can be installed in concrete to deliver a healing agent to the cracked/damaged regions. In this technique, healing agents are supplied by an external source through hollow tubes or network of tubes. There are two means of achieving self-healing by vascular approach: single-channel and multiple-channel systems. When only a single-component healing agent is used, the single-channel vascular approach is used; when it involves healing by the reaction of two healing agents, multiple channels are used. Moreover, although feasible at laboratory scale, it is difficult to

cast concrete with a network of pipes for vascular self-healing on actual construction sites. In many ways, the problems encountered by these two aforementioned methods can be addressed by capsule-based self-healing [9]. That's why the proposed modeling in this thesis focused on the autonomous self-healing with encapsulation technique. It should be noted that the performance of the autonomous healing mechanism is affected by several factors including the strength of the healing agent, size and percentage of microcapsules, shell thickness and encapsulation technique [8]. Present developments are mainly focused on laboratory testing. In most experiments, the healing efficiency is tested for pre-notched specimen where the direction of crack propagation can be controlled well. However, in engineering applications, the crack location will not be known in advance. Moreover, certain physical phenomena are difficult to detect experimentally. It's worth mentioning that the defining of the healing mechanism has become more complex with the introduction of the advantages of the autonomic mechanism to the autogenic, in order to decrease its disadvantages, as is well known by improved autogenous self-healing. A simple diagram is presented in [18], to illustrate the interaction between the self-healing mechanisms, see Figure 2.3.

Engineering the self-healing concrete involves the design and optimization of the concrete where the microcapsules are driven to burst and discharge their entire payload at a damaged region, thereby delivering a high concentration of healing agents to a small area. Fluidity is necessary for the transport of the agents to a damaged site or to spread the healing agents throughout the affected region. For an efficient SHC design, it is of utmost importance to introduce fluidic components into concrete without sacrificing the mechanical properties of the concrete structure. Therefore, it is essential to understand the rupture behavior of the capsules and the release of the encapsulated solution [27]. Computational modeling of the interaction between the concrete matrix and the capsule surface can provide useful information about the probability of fracture or debond the capsule when it counters the crack. The interface strength between the capsule and the concrete should be high enough to avoid interface failure, so studying the cracking process is very important to guarantee that the capsules will break in order to release the healing agent hence the transportation and solidification process can begin properly.

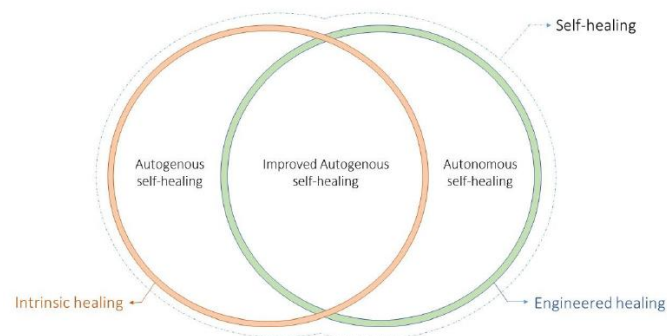


Figure 2.3: Schematic diagram illustrating self-healing mechanisms [18]

2.4 Passive and Active Modes of Self-healing

Self-healing mechanism may also be classified depending on the passive or active nature of their healing abilities. A passive mode self-healing has the ability to react to an external stimulus without the need for human intervention, whereas an active mode smart structure requires intervention in order to complete the healing process. Both systems have been tested, with respect to concrete by Dry [4], and are illustrated in Figure 2.4 for active release mode and are illustrated through the melting of a wax coating on porous fibers containing methylmethacrylate healing agent and Figure 2.5 for passive release mode illustrated through only the physical cracking of the brittle fiber under loading. A fully passive release system draws its main benefits from no need for human inspection, repair, and maintenance.

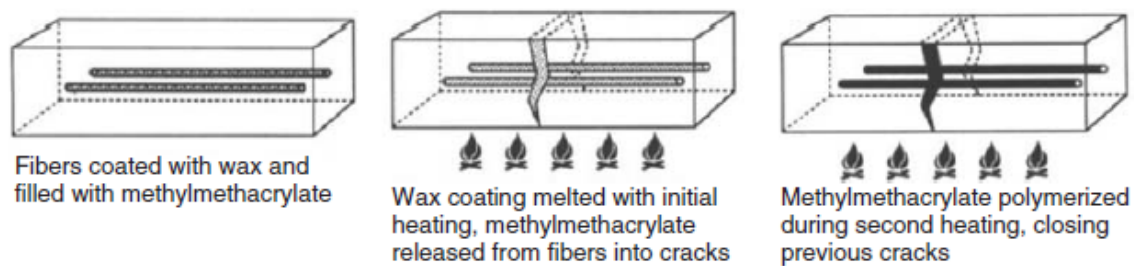


Figure 2.4: Active release mode of self-healing concrete (Dry [4]).

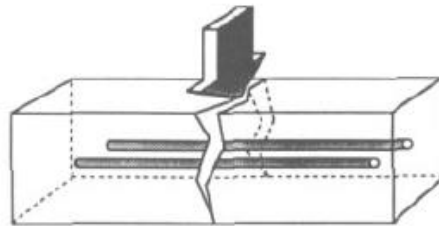


Figure 2.5: Passive release mode of self-healing concrete by cracking (Dry [4]).

2.5 Encapsulation Techniques

Various encapsulation techniques have been proposed in the literature. Suitable encapsulation techniques and materials should preferably be able to survive the concrete mixing process, so a certain flexibility and strength of the capsules is required at the time of concrete mixing. In addition, the influence of the capsules on the workability of the fresh concrete needs to remain limited. Once the concrete has hardened, the capsules need to be able to release the healing agent upon crack formation. If the self-healing mechanism should be triggered upon crack formation, this means that once the concrete has hardened, the capsules need to become brittle enough to break as soon as a crack appears. Moreover, the influence of the capsules on the mechanical and physical properties of the hardened concrete need to remain limited. The shape and dimensions of the capsules need to be such that the chance of a crack going through the capsules is maximized and that optimal release efficiency from the capsules into the crack is obtained. Moreover, the capsules' dimensions need to allow complete filling of the created crack. Although the list of requirements for the encapsulation material is already quite extended, it is also important to notice that capsules can only result in successful self-healing if the encapsulation material can withstand the harsh conditions inside the concrete matrix and is compatible with the healing agent which it should protect against the concrete matrix [28].

2.5.1 Capsule Materials

There are a variety of encapsulating materials, such as gelatin, silicon, glass, ceramic, expanded clay, cementitious, and polymers have been used in developing self-healing mechanism in concrete. Polymeric microcapsules are very frequently used and they are prepared by an oil-in-water dispersion mechanism of the polymer material, based mainly on the miniemulsion polymerization technique [29]. Urea and formaldehyde are made to react in the liquid phase, which eventually becomes cross-linked to form the urea formaldehyde (UF) capsule shell wall. The prepolymer that is formed by reaction in the water phase can be deposited to give a rough texture to the microcapsules. This can help to improve bonding with the cementitious matrix. Such capsules with healing agent have been used in [30-34]. Polyurethane (PU) capsule materials have also been used in self-healing applications [35]. Melamineurea-formaldehyde (MUF) microcapsules have been reported to demonstrate properties superior than those made only from UF; synthesis of the former is also easier [36]. An interesting summary comparison for capsule materials have been used in the literature, and can be found in [8, 9]. Once the capsules survived the concrete mixing and casting process, it is important that they remain stable within the highly alkaline cementitious matrix and that the shell is not affected by the encapsulated material. Therefore, the use of inert encapsulation materials, such as glass, may be beneficial. Although glass is used frequently as encapsulation material, it should be noted that this may induce alkali-silica reaction when a high amount of alkalis are present in the cementitious matrix. This drawback is avoided when inert ceramic capsules are used as proposed by [37]. A comparative study for the efficiency of cylindrical capsules made from glass and perspex (PMMA) has been done by [38]. This study has revealed that although perspex is stronger and more ductile than glass, this material was not suitable as it reacted with the healing agent. Other organic materials such as PP, PU, UF, EVA and gelatin gave good results when used as encapsulation material. Silica capsules have been used instead of their polymeric counterparts, since the chemical nature of these microcapsules makes them more likely to be compatible with the cementitious matrix and may result in a better interface [8].

Cement-based tubes is an alternative recently introduced in the literature that gains ground due to its great interfacial bonding features with concrete [39]. Also, a recent study focused on the use of additive manufacturing techniques as a possible way to produce novel types of macro-capsules, suitable to be filled with different healing agents and subsequently embedded in cementitious materials to introduce self-healing properties and deal with the sensitivity of these materials to crack formation. Specifically, tubular macro-capsules were produced by 3D printing and filled either with an expansive polyurethane resin or with a liquid sodium silicate [40]. Polymeric capsules possess the advantageous possibility of altering their properties and can thus fulfill the contradictory requirements of being flexible at the moment of concrete mixing and becoming more brittle at the moment of crack formation [28]. That is why the proposed modeling in this thesis focuses on polymeric capsules.

2.5.2 Capsule Geometries

The shape of the embedded capsule is a factor that should be considered. A spherically shaped capsule will provide a more controlled and enhanced release of the healing agent upon breakage, and will also reduce the stress concentrations around the void left from the empty capsule. A tubular capsule, however, will cover a larger internal area of influence on the

concrete for the same volume of healing agent (higher surface area to volume ratio). The potential release of the healing agent upon cracking, however, will be reduced since localized and multiple cracking may occur, thus inhibiting the effective distribution of the healing agent [1].

2.5.2.1 Continuous Supply Pipes / Vascular Tubes

The vascular approach of self-healing closely mimics the vascular network system in the human body [9]. In early work presented by Dry [4], the active provision of a healing agent was proposed by the use of an internal delivery vacuum pressure system, as shown in Figure 2.6. Continuous glass supply pipes, with or without vacuum pumps, have the advantage of being able to allow the type of repairing agent to be varied, and additional supply to be provided. In a case, without a vacuum pressure system the release of the healing agent will be driven from the tank via the vascular into the crack due to gravitational and capillary forces. When this approach is used in combination with a one-component healing agent, a one channel vascular system is applied Figure 2.7(A), while a multiple channel system is used in combination with a multi-component healing agent, Figure 2.7(B) [8]. This allows larger fractures to be healed compared with other encapsulation methods. The significant disadvantage of the method is the care that must be taken during casting to avoid tube breakages. Hence, this method is not suitable for in situ casting of concrete. It does, however, provide an interesting feasibility test for the concept of self-healing in cementitious materials [1]. Air-curing Cyanoacrylate healing agent provided in glass tubes has been used in other experimental studies [8].

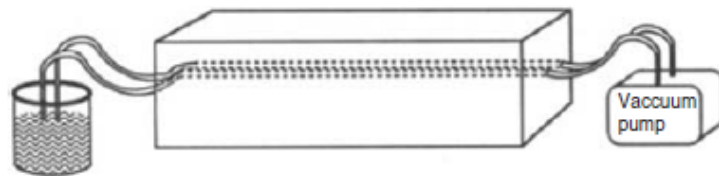


Figure 2.6: Replacing adhesive inside continuous supply pipes by vacuum (Dry [4]).

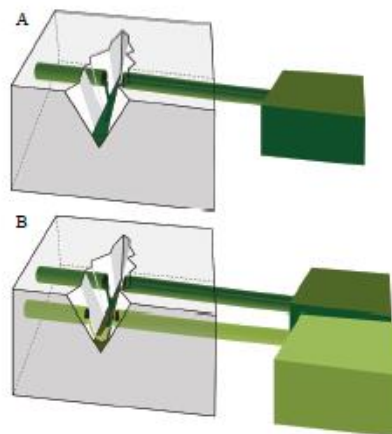


Figure 2.7: Release of healing agent via vascular tubes without vacuum pressure system [8].

Although additional healing agents can be provided when the vascular based approach is used and thus even large cracks can be healed, the healing agent will leak out of the cracks when they become too wide. Therefore, some studies combined this approach with a mechanism to reduce the crack width. They included both shape-memory alloy (SMA) wires and continuous adhesive filled glass tubes. Upon damage, the glass tubes break. Immediately after unloading, the deflection of the structural member is recovered due to the super elasticity of the SMA wire. At the same time the switch of the repairing vessel, containing healing agent, is turned on and the healing agent flows out of the broken, open fibers to fill and repair the cracks [8].

2.5.2.2 Capillary Tubes

The capillary tubes which developed for blood testing in the medical industry are utilized as encapsulating containers for an ethyl cyanoacrylate healing agent. Their initial test regime was aimed at confirming the sensing and actuation mechanisms of engineered cementitious composites (ECC), through forced cracking of single hollow capillary tubes, under the eye of an environmental scanning electron microscope (ESEM) [41]. Custom made hollow capillary tubes, 500 μm in diameter and 60 μm wall thickness embedded inside ECC specimens with dimensions 10mm \times 10mm \times 1.5 mm, were used, as illustrated in Figure 2.8 [1].

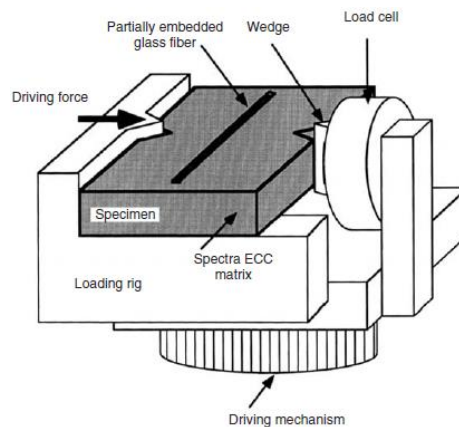


Figure 2.8: capillary tube specimen loading configuration [1].

2.5.2.3 Tabular Capsules / Cylindrical Tubes (Macro-capsules)

Recently a research group at Ghent university conducted experimental studies on macro-capsules made from different materials; thin glass, thick glass, and cementitious, as illustrated in Figure 2.9. Acoustic emission is applied to assess the capsules' effect on fracture processes. Events localization indicates fracture process zone expansion by 40%. It is demonstrated that the capsules contribute beneficially as local reinforcement by disturbing the crack route and creating several microcracks, which is further validated by digital picture correlation [42]. Although the advantage of this system is that the chance of a crack hitting the tubes is higher, the tubular encapsulation technique will only be applicable for precast concrete elements as a manual introduction of tubular capsules is required [8].

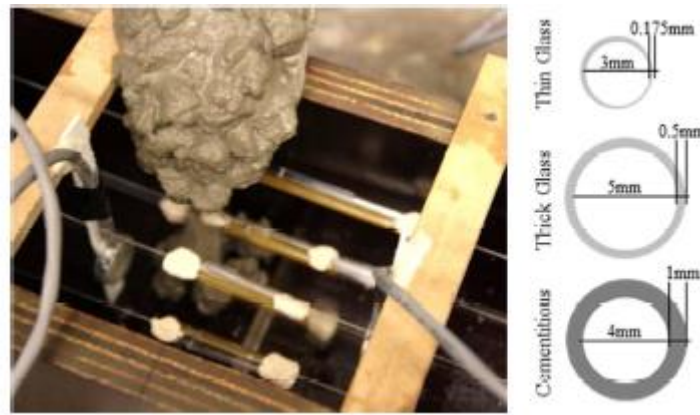


Figure 2.9: Tabular capsules from different materials [42].

2.5.2.4 Microcapsules

The microcapsule based system may have different shapes of capsules e.g. spherical, cylindrical etc. The advantage of dispersed microcapsule inclusion is that the concrete can react to diffuse cracking at multiple locations, leakage of healing agent from the capsules into the crack due to gravitational and capillary forces. The disadvantage is that additional repairing agent cannot be supplied once the original agent has been exhausted [1]. Microcapsule based self-healing is triggered when the damage or crack propagates to rupture the capsule shell then releases the healing agent. Healing agent reaction can be induced in various ways. The reaction can be done upon contact with moisture or air or by heating (Figure 2.10A&B) or upon contact with the cementitious matrix itself (Figure 2.10C&D), other way to occur the reaction is by making contact with a second component which is already present in the matrix (Figure 2.10E&F) or provided by additional capsules (Figure 2.10G&H). The microcapsule based system may have different shapes of capsules e.g. spherical (Figure 2.10A,C,E&G), cylindrical (Figure 2.10B,D,F&H) [8].

In preliminary investigations, urea-formaldehyde microcapsules (diameter 20–70 μm) filled with epoxy resin and gelatin microcapsules (diameter 125–297 μm) filled with acrylic resin were used in compression and splitting tests. In addition to the problems of blending two-agent epoxies, it is concluded that the quantity of repairing agent provided by microencapsulation is very small and limited, and the bond strength between the microcapsule and the matrix needs to be stronger than the strength of the microcapsule [5]. Inclusion of hollow capsules filled with a healing agent may influence the tensile and compressive strength of concrete. Moreover, after the release of the healing agent, spherical, cylindrical or tubular holes remain in the structure. Therefore, capsule dimensions need to be small enough in order not to change the properties of the structure too much [8]. In a study used UF spherical microcapsules with a diameter of 120 μm and concluded that the concrete compressive strength remained unaffected by the presence of these capsules [32]. Also another study noted that the compressive strength remained unaffected when spherical PU microcapsules were embedded [35]. In general, spherical capsules will have less influence on the mechanical properties as their shape reduces the stress concentrations around the void left from empty capsules [43]. That's why the proposed modeling in this thesis focused on spherical microcapsules.

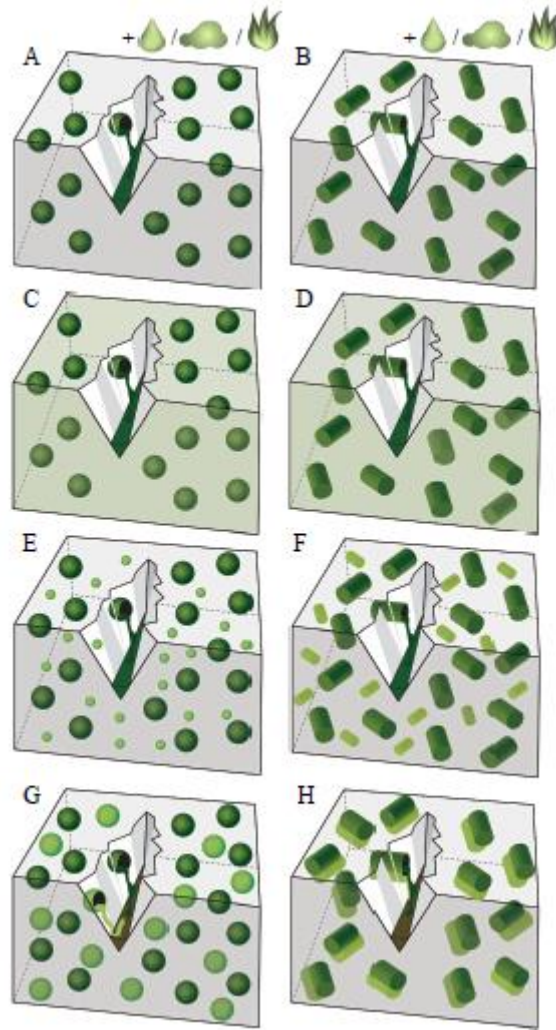


Figure 2.10: Microcapsule based self-healing techniques. Reaction of encapsulated healing agent due different contact with (A&B) moisture or air or heating (C&D) cementitious matrix (E&F) second component present in the matrix (G,H) second component provided by additional microcapsules [8].

2.6 Types of Healing Agents

Healing agents play a very important role in the self-healing process, especially in autonomic self-healing. Various healing agents have been proposed in the studies that have been undertaken on the self-healing of concrete. The effectiveness of the healing process is not only dependent on the capillary forces that are forced by the crack width [1]. In order to suit as healing agent for self-healing concrete, several requirements need to be fulfilled. At first, the shelf life of the healing agent is a very important factor: it should be as long as possible. While the healing agent will be embedded inside the cementitious matrix at the time of casting, its reactivity should remain until cracks appear. Not only the reactivity, but also the viscosity of the healing agent at the moment of capsule breakage is of utmost importance. The viscosity should be low enough to allow the agent to flow out of the capsules and to fill narrow micro-cracks. On the other hand, if the viscosity is too low the healing agent will not remain inside the crack as it will be absorbed by the pores of the cementitious matrix or seep

out of the crack. A third requirement is that the polymerization reaction should preferably take place without human intervention. Furthermore, the reaction time of the healing agent is an important parameter which needs to be taken into account. When the healing agent reacts too fast, not enough time is left for the agent to fill the crack. Conversely, the reaction time should be limited in order to stabilize the crack and prevent further growth. As a last requirement, it is important that the released healing agent completely fills the cracks, to prevent ingress of aggressive substances. Therefore, expansion of the healing agent upon reaction is a desired property, as bigger crack spaces can be filled in this way [28].

2.6.1 Bacterial

The potential of bacteria to act as a self-healing agent in concrete is investigated in the literature. Bacteria naturally occur virtually everywhere on earth, not only on the surface but also deep within, for example, in sediment and rock at a depth of more than 1 km. Various species of so-called extremophilic bacteria, that is, bacteria that love the extreme, are found in highly desiccated environments such as deserts, inside rocks, and even in ultrabasic environments that can be considered suitable for the internal concrete environment. In some previously published studies, the application of bacteria for cleaning of concrete surfaces and improving the strength of cement–sand mortar was reported. Furthermore, in some studies, the crack-healing potential by mineral-precipitating bacteria on degraded lime-stone and ornamental stone surfaces as well as on concrete surfaces was investigated and reported [1]. This approach utilizes bacteria to induce calcium carbonate (CaCO_3) precipitation resulting from bacterial metabolism in highly calcium environment. The concrete environment should ensure the availability of nutrients for bacteria. The bacteria type should be chosen in a way that it can withstand the highly alkaline environment of cement and internal compressive pressure [44]. It is worth to mention, that the encapsulation technique is applied with bacteria as well. In this technique, the spores of *Bacillus pseudofirmus* and *Bacillus cohnii*, calcium lactate and yeast extract encapsulated in porous expanded clay [45]. Self-healing was visually observed from the presence of calcium carbonate precipitates on the cracked surface [44]. Porous clay aggregates (lightweight aggregates (LWA) act as an internal source of moisture that is necessary to support bacterial precipitation action. However, the efficiency depends on a number of parameters, such as the amount of water in the aggregate, aggregate spacing, and aggregate pore structure. There is a limitation to the use of expanded clay encapsulation. When natural aggregates are replaced with clay LWA, there is substantial reduction in the mechanical strength of concrete. Aggregates form the bulk of concrete and the compressive strength of concrete is substantially determined by their toughness. As much as 50% strength reduction was observed after 28 days, which is not desirable for structural applications. When the clay particles ruptured, calcium precipitation by microbial action occurred as a result of the bacteria spores coming in contact with air. After 100 days of immersion in tap water, the maximum crack width that could be healed completely was about 0.46 mm. Activity up to 6 months has been observed so far [9].

2.6.2 Super Absorbent Polymers (SAP)

Several research works have investigated the possibility of mixing super absorbent polymers (SAP), also known as hydrogels, into cementitious materials to provide additional water. SAP

are cross-linked polymers that can absorb a large amount of liquid and swell substantially to form a soft and insoluble gel. Their swelling capacity is highly dependent on the alkalinity and ionic concentration of the solution, so SAP particles show reduced swelling when mixed into fresh concrete. Upon cement hydration, SAP release the absorbed water and shrink, leaving behind small macro-pores. When cracks arise, they are likely to propagate through the pores and ingress of moisture via the crack, causing the SAP to swell again. If the external fluid has a low ionic concentration, the SAP will swell more than in the concrete pore solution, hence expanding beyond the pore into the crack leading to a direct physical blocking effect. During dry periods, SAP release their water content again, stimulating autogenous healing. It has been revealed that the initial swelling of SAP particles during concrete mixing causes the formation of pores and thus a reduction in strength. Several further studies were performed in order to overcome this drawback [8].

2.6.3 Alkali–Silica Solution (Mineral Admixtures)

The usage of a diluted and undiluted alkali–silica solution as a healing agent in concrete is presented by [5]. The alkali–silica solution in the presence of oxygen causes hydration, thereby bonding the original crack faces together. The strength of the bond is less than that of glue, although this is unimportant as long as the bond strength is greater than the tensile strength of the surrounding material [1]. An experimental study of involving a sodium silicate solution stored in polyurethane microcapsules present in the concrete matrix. The flexural strength recovery, the improved toughness, and the reduction of corrosion make it a promising material for construction [35]. Also, Employed sodium silicate solution encapsulated in 5 mm wax capsules for self-healing in a cementitious composite which demonstrated recovery of mechanical properties including flexural stiffness and strength after damage induced by three-point bending tests [46].

2.6.4 Polymeric (Epoxy, Cyanoacrylate, Polurethane, MMA)

Various types of polymeric healing agents have already been encapsulated and embedded in concrete to obtain self-healing properties because the polymeric agents are also used for traditional, manual crack injection. Most polymeric healing agents are available in one or two-part systems which are also known as single-component or multicomponent. Single-component healing agents, which require the application of heat in order to cure, are less suited. Single-component agents which polymerize upon contact with moisture are much more appropriate for encapsulation. In addition, multicomponent agents which harden at room temperature upon contact with a second component can be used. In the latter case, both components will be embedded in separate capsules which may result in an extended shelf life. However, the reaction and the final properties of the cured agent should be insensitive to the mix ratio and should not require proper mixing of both components [28].

Initial trials to obtain self-healing concrete were performed with encapsulated methyl methacrylate (MMA) which is a multicomponent healing agent [4, 47]. Later, other researchers reported the use of MMA as a healing agent [25, 26]. Silicone as single-component agent has also been used as a healing agent in self-healing concrete [48]. Cyanoacrylate (CA) which is also known as superglue is used also as single-component agent in self-healing concrete. Low-viscosity epoxy resins are currently the principle healing agent

used for repairing concrete floors, bridge decks etc. Epoxy resins are considered to be durable materials as they have good thermal, moisture and light resistance. They are available in one or two-part systems. A one-part epoxy is activated by the presence of heat to cure the material and a two-part system is cured by the presence of both a hardener and resin component [1]. Single- or multicomponent epoxy used as healing agent inside self-healing concrete [28]. The main problem with the application of two-part epoxy resins to the autonomic healing of concrete is that the probability of presenting both the components simultaneously at a crack location is too low. In order to overcome this by manually place the two components in adjacent tubes. Despite both the tubes cracking and releasing their respective agents, poor mechanical behavior was observed due to insufficient mixing of the fluid blend [5]. The encapsulation of single- and multicomponent polyurethane has also been reported as promising healing agent. The main goal of self-healing concrete is to improve the durability of concrete structures, which requires complete crack filling and expansion of the encapsulated healing agent upon polymerization. As polyurethane is the only of the above mentioned polymeric healing agents which expands upon polymerization. Both, the single- and multicomponent polyurethane react upon contact with moisture but the reaction of the multicomponent polyurethane is accelerated upon contact with the second component. Moreover, polyurethanes with a very low viscosity were selected to allow the agent to flow easily into the crack [28]. An interesting summary comparison for most healing agent materials have used in the literature, can be found in [8, 9].

2.7 Applications of Self-Healing Concrete

The World's first self-healing concrete building was constructed in Netherlands using self-healing concrete with bacteria acting as self-healing agents (organic concrete). This pilot project is a lifeguard station by a lake developed by Delft University of Technology[49]. Recently the same Delft research group reported that two full scale demonstrator projects with bacteria-based self-healing concrete had been executed. The first one concerned the construction of a wastewater purification tank consisting of precast concrete elements. The second full scale self-healing concrete demonstrator project involved an in situ cast rectangular concrete water reservoir. In addition they reported the developed bacteria-based self-healing repair mortar which was applied in two full-scale projects in order to demonstrate structural repair applicability and delivery of water tightness of cracked concrete basement walls respectively [50]. Recently the first Large Scale Application with self-healing concrete was built in Belgium which is a roof slab of an inspection pit that was cast with bacterial self-healing concrete and is now in normal operation [51].

Materials for Life (M4L) was a 3 year, EPSRC funded, research project carried out by the Universities of Cardiff, Bath, and Cambridge to investigate the development of self-healing cementitious construction materials. In this project the UK's first site trial of self-healing concrete, which was the culmination of that project. The trial comprised the in-situ construction of five concrete panels using a range of self-healing technologies within the site compound of the A465 Heads of the Valleys Highway upgrading project. Four self-healing techniques were used both individually and in combination with one another. They were: (i) the use of microcapsules developed by the University of Cambridge, in collaboration with industry, containing mineral healing agents, (ii) bacterial healing using the expertise developed at Bath University, (iii) the use of a shape memory polymer (SMP) based system

for crack closure and (iv) the delivery of a mineral healing agent through a vascular flow network. Both of the latter, (iii) and (iv), were the product of research undertaken at Cardiff University [52]. Microbial Self-healing concrete was mainly used at the junction of the side wall and bottom plate of sluice chamber in Beijing-Hangzhou canal in China [53]. It is worth to mention that the self-healing concrete applications are not only limited to the buildings and structures but also in pavements as there are some studies done to apply the self-healing concept in asphalt materials [54].

3 The eXtended Finite Element Method (XFEM) and Cohesive Surface Technique

3.1 Introduction

Standard finite element approximations are approximations with piecewise differentiable polynomials that are not well suited for problems with strong and weak discontinuities. Strong discontinuity is referred to a jump in the displacement field; a typical strong discontinuity is a crack or hole. A weak discontinuity is referred to a jump in the strain field which occurs at material interfaces, for example. The only opportunity to accurately model these kinds of discontinuities is to conform the finite element mesh with the line of discontinuity. This becomes a major difficulty for moving discontinuities that can occur for moving interfaces in two phase-flow problems or evolving cracks, for example [55]. The extended finite element method (XFEM) is a finite element approximation that is able to handle arbitrary strong and weak discontinuities without the requirement for re-meshing. In this chapter, the formulation of XFEM is outlined. The cohesive zone model, the interfacial transition zone (ITZ) including the cohesive surface technique and the cohesive element approach are reviewed. In addition to the implementations of these techniques in Abaqus software are discussed in detail.

3.2 The eXtended Finite Element Method (XFEM)

Modeling stationary discontinuities, such as a crack, with the conventional finite element method requires that the mesh conforms to the geometric discontinuities. Creating a conforming mesh can be quite difficult. Modeling a growing crack is even more cumbersome because the mesh must be updated continuously to match the geometry of the discontinuity as the crack progresses. The extended finite element method (XFEM) alleviates the need to create a conforming mesh. XFEM was first introduced by Belytschko and Black [56]. It is an extension of the conventional finite element method based on the concept of partition of unity by Melenk and Babuška [57], which allows local enrichment functions to be easily incorporated into a finite element approximation. The presence of discontinuities is ensured by the special enriched functions in conjunction with additional degrees of freedom. However, the finite element framework and its properties such as sparsity and symmetry are retained. XFEM does not alleviate the need for sufficient mesh refinement in the vicinity of the crack tip [58]. XFEM has been implemented into commercial software such as ABAQUS and has become one of the most popular methods for fracture [2]. One important aspect of problems with moving interfaces is the tracking of these interfaces. Powerful tools for tracking interfaces are the level set method and phantom node method that will be explained in the section 3.2.3. a more specific formulation of this technique can be found in [55], although in the following sections an overview of the XFEM formulation and its implementation in Abaqus will be discussed.

3.2.1 Partition of Unity Method (PUM)

XFEM is based on a local partition of unity, in which a basis function, N_I , is associated with a node I . The region of support of a basis, or shape, function is the set of elements that include node I . These shape functions form a partition of unity.

$$\sum_{I \in N} N_I(x) = 1 \quad (3.1)$$

So that any arbitrary function $f(x)$ may be reproduced exactly by

$$\sum_{I \in N} N_I(x) f(x) = f(x) \quad (3.2)$$

This ability forms the basis of the XFEM. By choosing appropriate function $f(x)$ for each node, a priori knowledge of a model's behavior may be incorporated while retaining the mathematical basis of standard finite element analysis, which is known as enrichment concept.

3.2.2 The concept of enrichment

XFEM is used with enrichment terms, added to the normal displacement interpolation, so a crack within an element can be described without the requirement for re-meshing. In essence, there are two concepts of enrichment; intrinsic enrichment and extrinsic enrichment. The motivation of enrichment is to increase the accuracy of the solution by introducing new, more accurate information into the approximation. In the case of a cohesive crack, the displacement field is discontinuous across the crack and that the crack has to close at the crack tip. In linear elastic fracture mechanics (LEFM) where the analytical solutions are known (e.g. the stress at the crack tip is singular), the accuracy of the method can be increased enormously by an enrichment. In an intrinsic enrichment, the enrichment function is included in the polynomial basis of the element-free Galerkin method (EFG) shape function. In an extrinsic enrichment, additional functions are introduced externally to the EFG basis. The enrichment function in PUM is required over the whole domain, while the XFEM uses local extrinsic enrichment to model the weak or strong discontinuity within a finite element. The XFEM approximation can be decomposed into a usual part and into an enriched part.

These aspects will be discussed only for a single crack. Moreover, two-dimensional triangular and quadrilateral finite elements with linear shape functions are considered. The crack line is approximated with level sets where the level set is discretized with the same shape functions as the mechanical properties. Hence, the curvature of the crack can be maximal bi-linear for the quadrilateral element and linear for the triangular element. Geometrical and material nonlinearities aren't considered. For now, it is assumed that the crack doesn't propagate and will study only the crack kinematics. The subsequent issues will be discussed in the following sections. The Heaviside enrichment is able to capture the jump in the displacement field. However, it does not necessarily guarantee the closure of the crack at its crack tip. The simplest possibility to ensure crack closure at the crack tip is to locate the crack tip at one of the element edges and not to enrich the adjacent nodes, see Figure 3.1. Two potential crack paths including the enriched nodes are illustrated in Figure 3.2. The black dots denote the enriched nodes and the standard nodes are not shown. This kind of crack closure has the disadvantage that the crack length is governed by the element size since it is required to grow the crack through the entire element. Another opportunity to close the crack within an element is by use of branch functions B which can be defined as

$$B = [B_1 \ B_2 \ B_3 \ B_4] = \left[\sqrt{r} \sin \frac{\theta}{2}, \sqrt{r} \cos \frac{\theta}{2}, \sqrt{r} \sin \frac{\theta}{2} \sin \theta, \sqrt{r} \cos \frac{\theta}{2} \sin \theta \right] \quad (3.3)$$

B is the branch functions according to the LEFM literature. It is obvious that for $r = 0$, the crack closes at the crack tip. Moreover, the solution will be more accurate as the information of the analytical solution since has been put into the approximation of the displacement field as the following:

$$u^h(x) = \sum_{I \in \delta} N_I(x) u_I + \sum_{I \in \delta_c(x)} N_I(x) H(x) a_I + \sum_{I \in \delta_t(x)} N_I(x) \sum_K B(x) b_I^K \quad (3.4)$$

δ_t represent the set of nodes that are influenced by the crack tip. The first term on the right-hand side of eq. (3.4) is the standard approximation, the second term and the third term is the enrichment, see Figure 3.3.

For Quadrilateral elements (Q4) the eq. (3.4) could be simplified to [58]:

$$u = \sum_{I \in N} N_I(x) \left[u_I + H(x) a_I + \sum_{\alpha=1}^4 F_{\alpha}(x) b_I^{\alpha} \right] \quad (3.5)$$

$N_I(x)$ is associated with usual nodal shape functions, u_I is a usual nodal displacement vector associated with the continuous part of the finite element solution, $H(x)$ is associated with discontinuous jump functions across the crack surfaces, a_I is vector of the nodal enriched degree of freedom, $F_{\alpha}(x)$ is associated with elastic asymptotic crack-tip functions and b_I^{α} is the vector of the nodal enriched degree of freedom. The first term on the right-hand side is applicable to all the nodes in the model, the second term is valid for nodes whose shape function support is cut by the crack interior, and the third term is used only for nodes whose shape function support is cut by the crack tip.

$$H(x) = \begin{cases} 1 & (x - x^*) \cdot n \geq 0 \\ -1 & \text{otherwise,} \end{cases} \quad (3.6)$$

Where x is a sample (Gauss) point, x^* is the point on the crack closest to x , and n is the unit outward normal to the crack at x^* , see Figure 3.5.

$$F_{\alpha}(x) = \left[\sqrt{r} \sin \frac{\theta}{2}, \sqrt{r} \cos \frac{\theta}{2}, \sqrt{r} \sin \theta \sin \frac{\theta}{2}, \sqrt{r} \sin \theta \cos \frac{\theta}{2} \right] \quad (3.7)$$

Where (r, θ) is a polar coordinate system with its origin at the crack tip and $\theta=0$ is tangent to the crack at the tip.

These functions span the asymptotic crack-tip function of elasto-statics, and $\sqrt{r} \sin \frac{\theta}{2}$ takes into account the discontinuity across the crack face. The use of asymptotic crack-tip functions is not restricted to crack modeling in an isotropic elastic material. The same approach can be used to represent a crack along a bimaterial interface, impinged on the bimaterial interface, or in an elastic-plastic power law hardening material. However, in each of these three cases different forms of asymptotic crack-tip functions are required depending on the crack location and the extent of the inelastic material deformation. The different forms for the asymptotic crack-tip functions are discussed by [59], [60], and [61], respectively. When only the element containing the crack tip is enriched with the branch functions B, it is referred to as topological enrichment. However, this will not lead to optimal convergence rate which requires a geometrical enrichment as illustrated on the RHS of Figure 3.3. In a geometrical enrichment, the enriched area around the crack tip is kept constant once the mesh is refined. However, geometrical enrichments increase the number of degrees of freedom and lead to an increased ill-conditioning of the system's stiffness matrix which might require pre-conditioning or special solution techniques.

Below is a special case, where a crack is located close to an element node as shown in Figure 3.4. Consider an element spanned by the nodes a, b, c, d. The support of the node is defined by its adjacent neighbor elements. Node a, for example, has four neighboring elements. Hence, the support size is equal to the area of these four neighboring finite elements. By defining the parameters r^+ and r^- between the area on both sides of the crack and the total area of the support:

$$r^+ = \frac{A^+}{A^+ + A^-}, r^- = \frac{A^-}{A^+ + A^-} \quad (3.8)$$

If one of these ratios is smaller than a given threshold, the support node is no longer enriched. In the case of the element a, b, c, d; only nodes a and b will be enriched.

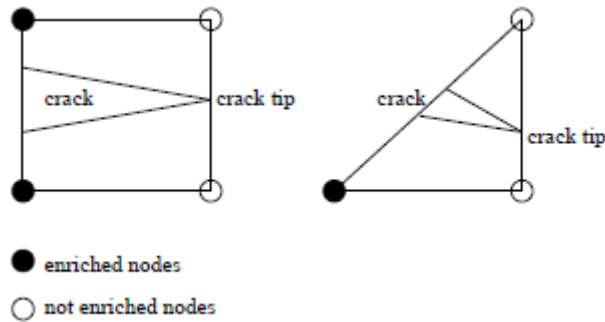


Figure 3.1: One opportunity to close the crack in XFEM [55].

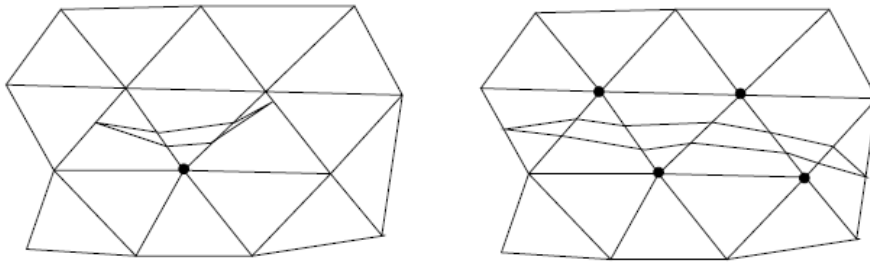


Figure 3.2: Example of enriched nodes when crack closure is realized by closing the crack tip at the element sides [55].

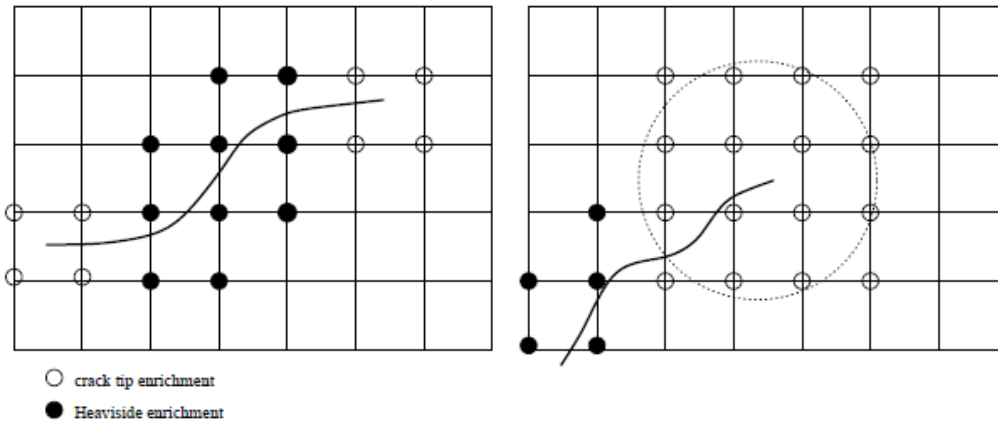


Figure 3.3: Crack with enriched elements [55].

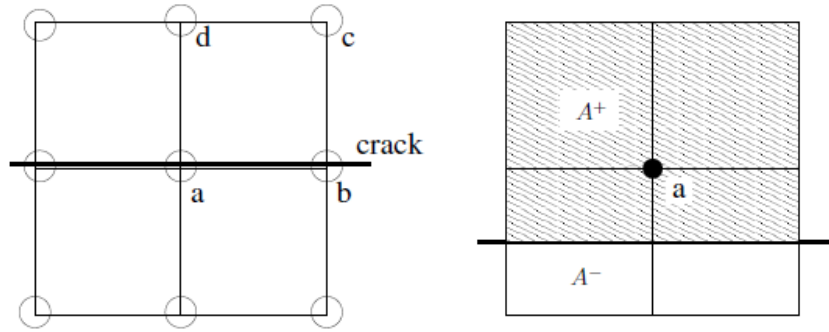


Figure 3.4: Enrichment criteria for cracks that are close to a node [55].

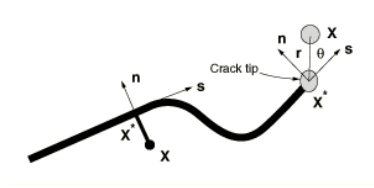


Figure 3.5: the discontinuous jump function across the crack surfaces; $H(x)$ [58].

3.2.3 Modeling moving cracks

The most well-known approach within the framework of XFEM to model moving cracks is based on traction-separation cohesive behavior. This is a very general interaction modeling capability, which can be used for modeling brittle or ductile fracture. XFEM-based cohesive segments method can be used to simulate crack initiation and propagation along an arbitrary, solution-dependent path in the bulk materials, as the crack propagation is not tied to the element boundaries in a mesh. In this case, the near-tip asymptotic singularity is not needed, and only the displacement jump across a cracked element is considered. Therefore, the crack has to propagate across an entire element at a time to avoid the need to model the stress singularity. This approach is already implemented in Abaqus to simulate crack initiation and propagation [58].

3.2.3.1 Phantom Node Method

This method is used for complex fracture problems in dynamics [62]. In order to understand the basic idea, consider a body that is cracked as shown in Figure 3.6, and the corresponding finite element discretization. Due to the crack, there are cracked elements cut by the crack. To have a set of full interpolation bases, the part of the cracked elements which belong in the real domain Ω_0 are extended to the phantom domain Ω_p . Then the displacement in the real domain Ω_0 can be interpolated by using the degrees of freedom for the nodes in the phantom domain Ω_p . The nodes are called the phantom nodes and are marked by empty circles in Figure 3.6. The approximation of the displacement field is then given by [55]:

$$u^h(x, t) = \sum_{I \in \{w_0^+, w_p^-\}} \mathbf{u}_I(t) N_I(x) H(f(x)) + \sum_{J \in \{w_0^-, w_p^+\}} \mathbf{u}_J(t) N_J(x) H(-f(x)) \quad (3.9)$$

Where $f(x)$ is the signed distance measured from the crack, $w_0^+, w_0^-, w_p^+, w_p^-$ are nodes belonging to $\Omega_0^+, \Omega_0^-, \Omega_p^+, \Omega_p^-$, respectively. $H(x)$ is the Heaviside function. As can be seen from Figure 3.6, cracked elements have both real nodes and phantom nodes. The jump in the displacement field is realized by simply integrating only over the area from the side of the real nodes up to the crack, i.e. Ω_0^+ and Ω_0^- .

In essence, phantom nodes, which are superposed on the original real nodes, are introduced to represent the discontinuity of the cracked elements, as illustrated in Figure 3.6. When the element is intact, each phantom node is completely constrained to its corresponding real node. When the element is cut through by a crack, the cracked element splits into two parts. Each part is formed by a combination of some real and phantom nodes depending on the orientation of the crack. Each phantom node and its corresponding real node are no longer tied together and can move apart. The magnitude of the separation is governed by the cohesive law until the cohesive strength of the cracked element is zero, after which the phantom and the real nodes move independently. To have a set of full interpolation bases, the part of the cracked element that belongs in the real domain, Ω_0 , is extended to the phantom domain, Ω_p . Then the displacement in the real domain, Ω_0 , can be interpolated by using the degrees of freedom for the nodes in the phantom domain, Ω_p . The jump in the displacement field is realized by simply integrating only over the area from the side of the real nodes up to the crack; i.e., Ω_0^+ and Ω_0^- . This method provides an effective and attractive engineering approach and has been used for simulation of the initiation and growth of multiple cracks in solids by [63, 64]. It has been proven to exhibit almost no mesh dependence if the mesh is sufficiently refined [58].

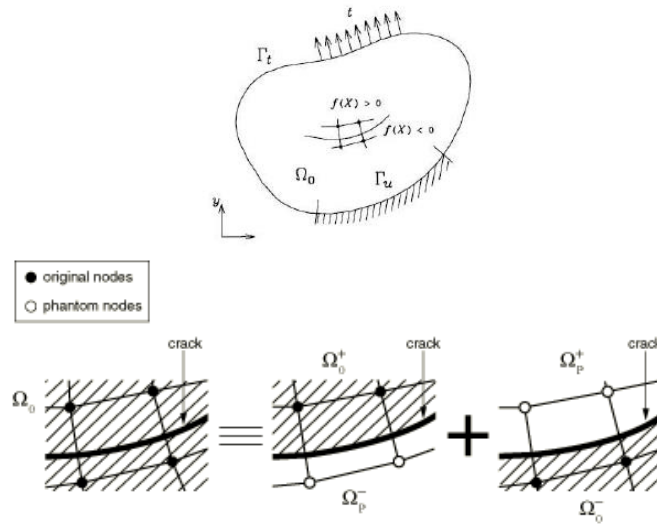


Figure 3.6: The principle of the phantom node method [55, 58].

3.2.3.2 Level set method

It is necessary to describe the geometry interfaces for the modeling of moving boundaries problems, such as crack propagation. Therefore, a numerical scheme that can be incorporated with the XFEM to track and update the geometry should be devised. The level set method is perhaps one of the most widely used methods. The level set method (LSM) is a recently

developed numerical method to capture the motion of interfaces and shapes in an implicit way. The name “level sets” refers to the sets which collect points that have the same certain level, i.e. value of signed distance. It provides an implicit way of describing the geometry of a surface by measuring the shortest distance from any point inside the domain to the boundary of the surface [55].

For example, consider an interface shown as a closed solid curve in Figure 3.7. A domain enclosed by the interface is noted as Ω and its boundary (noted as $\partial\Omega$) is the interface itself. A set of isocontours, shown as the dashed curve, are used to describe the interface. Contours inside take negative values while those outside are positive. Each isocontour collects all the points having the same distance value to the interface by:

$$\phi(x) = \text{sign}(\vec{N}(x_c) \cdot (x - x_c)) \|x - x_c\| \quad (3.10)$$

Where x contains the coordinates of an arbitrary point, x_c is the closest point on the interface to x , $\phi(x)$ is termed the implicit signed distance function and $\vec{N}(x_c)$ is the unit outer normal at x_c calculated by:

$$\vec{N}(x_c) = \frac{\nabla\phi}{\|\nabla\phi\|} \quad (3.11)$$

where $\|\cdot\|$ is the L_2 norm of a vector which defined as follows. Suppose a vector $x = \{x_1 + x_2 + \dots + x_n\}$ where n is the dimension of the vector and the L_2 norm of the vector is calculated by:

$$\|x\| = \sqrt{x_1^2 + x_2^2 + \dots + x_n^2} \quad (3.12)$$

The zero contour $\phi(x) = 0$ represents the interface. Normally, a set of data points are used to discretise the implicit functions ϕ . It is usually convenient to generate the points from the grid lines based on Cartesian coordinates, i.e. shown as the square mesh in Figure 3.7. The level set is usually discretized. The discretization is based on a finite element mesh where $N_I(x)$ is the shape function associated to the node I . The set of nodes which belong to the mesh is denoted by δ so the discretized level set is:

$$\phi(x) = \sum_{I \in \delta} N_I(x) \phi_I \quad (3.13)$$

Where ϕ_I is the value of the level set on node I . This discretization becomes useful when the value of the level set is needed at the element level. It can be evaluated by interpolation. Moreover, the derivative of the level set involves only the well-known derivatives of the shape functions:

$$\phi(x)_{,i} = \sum_{I \in \delta} N_{I,i}(x) \phi_I \quad (3.14)$$

To use level sets in fracture modeling requires specific adaptation and implementation. The first use of the LSM for crack description is given by [65] in 2D with XFEM. Two orthogonal level sets were used to describe a crack line or combinations of lines in 2D. A number of examples were tested and showed the feasibility of using level sets in describing and tracking crack propagation. The idea was later extended and developed in 3D crack modeling in a number of papers using the XFEM [66-68]. A key development that facilitates the treatment of cracks in an extended finite element analysis is the description of crack geometry, because the mesh is not required to conform to the crack geometry. The level set method, which is a powerful numerical technique for analyzing and computing interface motion, fits naturally

with the extended finite element method and makes it possible to model arbitrary crack growth without remeshing. The crack geometry is defined by two almost-orthogonal signed distance functions, as illustrated in Figure 3.8. The first, ϕ , describes the crack surface, while the second, ψ , is used to construct an orthogonal surface so that the intersection of the two surfaces gives the crack front. n^+ indicates the positive normal to the crack surface; m^+ indicates the positive normal to the crack front. No explicit representation of the boundaries or interfaces is needed because they are entirely described by the nodal data. Two signed distance functions per node are generally required to describe a crack geometry [58].

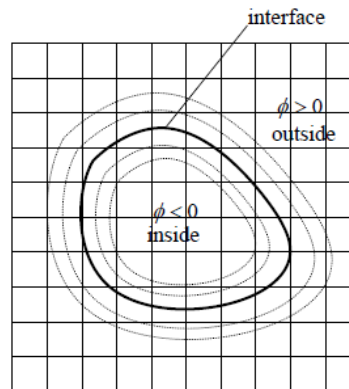


Figure 3.7: Signed distance function to describe an implicit surface [55].

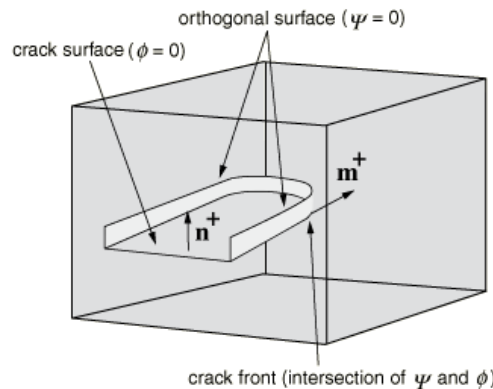


Figure 3.8: Representation of a nonplanar crack in three dimensions by two signed distance functions ϕ and ψ [58].

3.2.4 XFEM based on cohesive zone model

The concept of the cohesive zone model (CZM) of modeling fracture mechanics was developed by [69] for modeling cracks in brittle materials. In the cohesive zone model (CZM), the crack tip singularity predicted by the LEFM theory is replaced by a fracture process zone (the cohesive zone) where the material surface degrades from fully coherent to complete separation [70]. The constitutive behavior in the cohesive zone is described using a traction–separation relation as illustrated in Figure 3.9. The CZM is already implemented and available in the commercial software Abaqus. The available traction–separation model in Abaqus assumes initially linear elastic behavior followed by the initiation and evolution of

damage. The elastic behavior is written in terms of an elastic constitutive matrix that relates the normal and shear stresses to the normal and shear separations of a cracked element. The nominal traction stress vector, t , consists of the following components: t_n , t_s , and (in three-dimensional problems) t_t , which represent the normal and the two shear tractions, respectively. The corresponding separations are denoted by δ_n , δ_s , and δ_t . The elastic behavior can then be written as:

$$t = \begin{Bmatrix} t_n \\ t_s \\ t_t \end{Bmatrix} = \begin{bmatrix} K_{nn} & 0 & 0 \\ 0 & K_{ss} & 0 \\ 0 & 0 & K_{tt} \end{bmatrix} \begin{Bmatrix} \delta_n \\ \delta_s \\ \delta_t \end{Bmatrix} = K\delta \quad (3.15)$$

The normal and tangential stiffness components will not be coupled: pure normal separation by itself does not give rise to cohesive forces in the shear directions, and pure shear slip with zero normal separation does not give rise to any cohesive forces in the normal direction. The terms K_{nn} , K_{ss} , and K_{tt} are calculated based on the elastic properties for an enriched element. Specifying the elastic properties of the material in an enriched region is sufficient to define both the elastic stiffness and the traction-separation behaviour.

The failure mechanism for damage modeling consists of two steps: a damage initiation criterion and a damage evolution. The initial response is assumed to be linear. However, once a damage initiation criterion is met, damage can occur according to various damage evolution laws such as linear and nonlinear traction-separation response. The enriched elements do not undergo damage under pure compression.

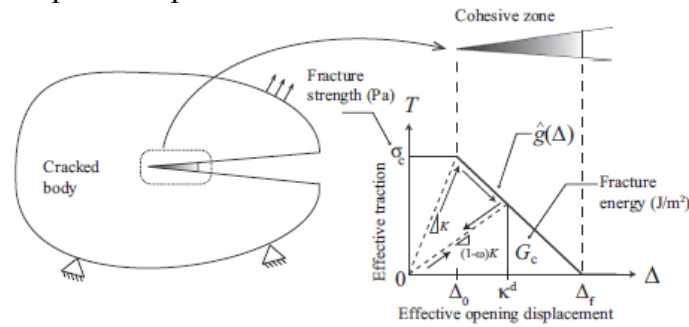


Figure 3.9: Schematic sketch of cohesive zone model (CZM) [70] .

Damage initiation (crack initiation):

Damage initiation is defined as part of the material properties, using damage for traction-separation law. There are a lot of damage initiation criteria available in the literature which are implemented in Abaqus as well such as Maximum principal stress criterion, Maximum nominal stress criterion, Quadratic nominal stress criterion, Maximum principal strain criterion, Maximum nominal strain criterion, and Quadratic nominal strain criterion. In this thesis, the Maximum Principal Stress (Maxps) Damage criterion is used. With this option, the damage will initiate when the maximal principal stress exceeds the critical value, which is the maximum strength of the material. Figure 3.10 shows the traction-separation response in the normal direction to the crack faces. A crack can appear in the centroid of any element of the mesh when the maximum principal stress calculated in its integration points satisfies the criterion of eq. (3.16). Although a more specific description of these techniques can be found in [58].

$$\left\{ \frac{\langle \sigma_{maxps} \rangle}{\sigma^*} \right\} \geq 1 \quad (3.16)$$

Where $\sigma_{\max ps}$ stands for the calculated maximum principal stress and σ^* stands for the maximum strength of the material. The symbol $\langle \rangle$ represents the Macaulay bracket with the usual interpretation (i.e., $\langle \sigma_{\max ps} \rangle = 0$ if $\sigma_{\max ps} < 0$ and $\langle \sigma_{\max ps} \rangle = \sigma_{\max ps}$ if $\sigma_{\max ps} \geq 0$). The Macaulay brackets are used to signify that a purely compressive stress state does not initiate damage. Damage is assumed to initiate when the maximum principal stress ratio; as defined in the eq. (3.16) reaches a value of one.

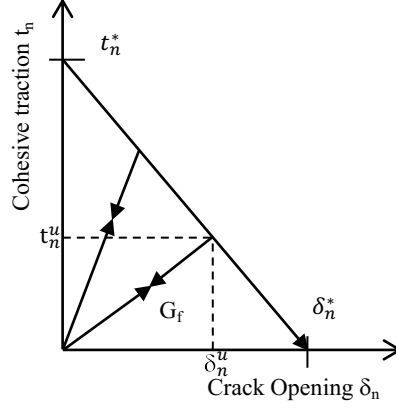


Figure 3.10: Traction-separation response.

Damage evolution (crack propagation)

The damage evolution law describes the rate at which the cohesive stiffness is degraded once the corresponding initiation criterion is reached. A scalar damage variable, D , represents the averaged overall damage at the intersection between the crack surfaces and the edges of cracked elements. It initially has a value of 0. If damage evolution is modeled, D monotonically evolves from 0 to 1 upon further loading after the initiation of damage. Either the maximal displacement or the fracture energy, which is the area under the curve in a graph of traction versus separation, must be specified. The normal and shear stresses components are affected by the damage according to [58]:

$$D = 1 - \frac{\delta_n}{\delta_n^u} \left(\frac{\delta_n^* - \delta_n^u}{\delta_n^* - \delta_n} \right) \quad (3.17)$$

$$t_n = \begin{cases} (1 - D)T_n & \text{if } t_n \geq 0 \\ T_n & \text{if } t_n < 0 \text{ (compression)} \end{cases} \quad (3.18)$$

$$t_s = (1 - D)T_s \quad (3.19)$$

$$t_t = (1 - D)T_t \quad (3.20)$$

Where t_n , t_s , and t_t are the normal and shear traction stress components acting between both crack faces. While T_n , T_s , and T_t are the normal and shear stress components predicted by the elastic traction-separation behavior for the current separations without damage. To describe the evolution of damage under a combination of normal and shear separations across the interface, an effective separation is defined as:

$$\delta_m = \sqrt{\langle \delta_n \rangle^2 + \delta_s^2 + \delta_t^2} \quad (3.21)$$

An accurate and efficient evaluation of the stress/strain fields ahead of the crack tip is important for both evaluating the crack initiation criterion and computing the crack propagation direction when needed. One of the most common ways for computing these fields is centroidal values of stress and strain. The stress/strain computed at the element centroid ahead of the crack tip is used to determine if the damage initiation criterion is satisfied and to determine the crack propagation direction, as illustrate in Figure 3.11.

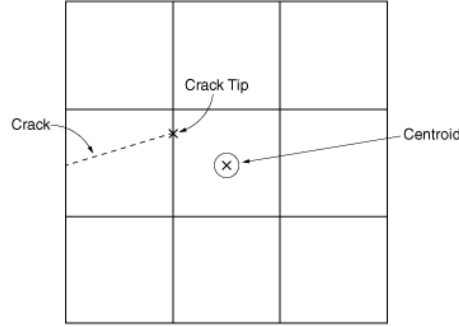


Figure 3.11: Centroidal and crack tip locations [58].

3.3 The Interfacial Transition Zone (ITZ)

The Interfacial Transition Zone (ITZ) is the zone which represents the interaction between mortar and aggregate. Many experimental and numerical techniques have been developed to measure the mechanical properties of ITZ, however, the properties are still not fully understood due to the complex microstructures. It is generally recognized that ITZs play a critical role in the concrete fracture process, and are mechanically weaker than mortar and aggregates due to the presence of a large number of pores and the gradient of the porosity from mortar to the aggregate surface. Therefore, an appropriate representation of the ITZs is essential for interfacial modeling [71]. In this thesis, the ITZ is employed to represent the interaction between the microcapsule and the concrete matrix and also to represent the interaction between the healing agent and the cracked surface of the concrete.

The constitutive matrix for the cohesive interface is expressed by the traction-separation law. The nominal traction stress vector, t , consists of the following components: t_n , t_s , and (in three-dimensional problems) t_t , which represent the normal and the two shear tractions, respectively. The corresponding separations are denoted by δ_n , δ_s , and δ_t . The elastic behavior can then be written as:

$$t = \begin{Bmatrix} t_n \\ t_s \\ t_t \end{Bmatrix} = \begin{bmatrix} K_{nn} & K_{ns} & K_{nt} \\ K_{ns} & K_{ss} & K_{st} \\ K_{nt} & K_{st} & K_{tt} \end{bmatrix} \begin{Bmatrix} \delta_n \\ \delta_s \\ \delta_t \end{Bmatrix} = K \delta \quad (3.22)$$

The failure mechanism for damage modeling consists of two steps: a damage initiation criterion and a damage evolution. The traction-separation relationship has two zones: (1) linear elastic traction zone, (2) damage evolution zone (softening); see Figure 3.12. The elastic response is governed by the stiffness K_{nn} , K_{ss} , K_{tt} the so-called penalty stiffness, whose value is calculated as a function of the two adjacent material stiffnesses [31]. It has been proved that its value has no influence on the overall sample stiffness [15] and it has been taken 1E6 MPa/mm in this thesis. Moreover, this assumes that the normal and shear penalty stiffnesses are decoupled, therefore a pure normal opening of the interface does not produce

shear forces, and vice versa. The contact cohesive behaviour is introduced in Abaqus in two approaches: (1) cohesive element, (2) cohesive contact/surface; see Figure 3.13 [58].

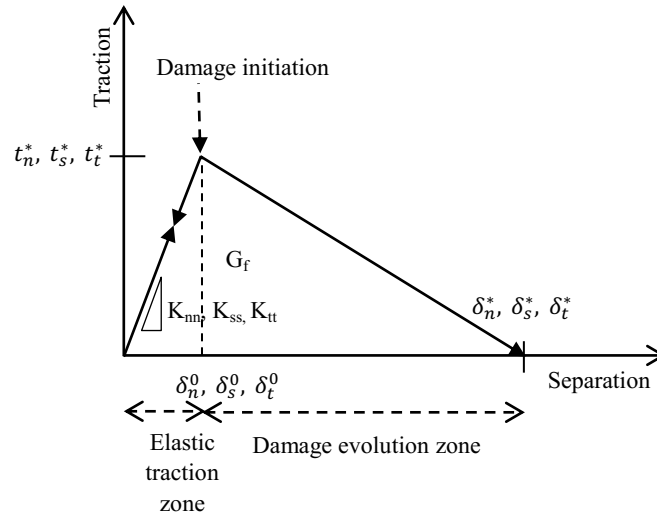


Figure 3.12: Typical traction-separation law.

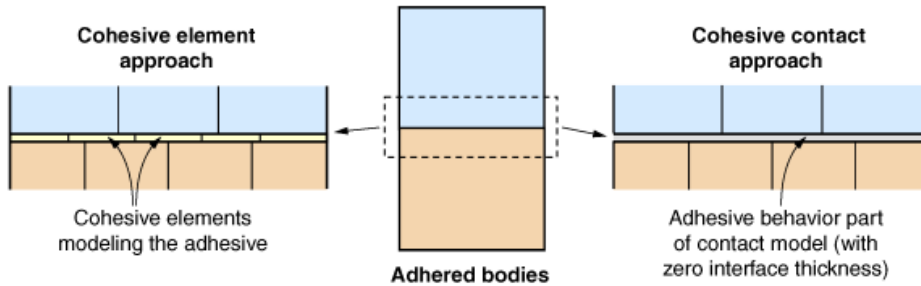


Figure 3.13: Schematic comparison of cohesive element and cohesive contact approaches [58].

3.3.1 Cohesive contact/surface (CS)

The cohesive surface approach is used to represent an infinitesimally thin layer of adhesive at a bonded interface. In fact, the cohesive surface is a zero thickness region that contains only the surface pairs initially in contact. That's why in this thesis the CS approach is employed to represent the interaction between the microcapsule and the concrete matrix, as well as to represent the interaction between the healing agent and the cracked surface of the concrete.

Damage initiation (separation initiation):

Damage initiation is defined as part of the interaction properties, using damage for traction-separation law. There are a lot of damage initiation criteria available in the literature which are implemented in Abaqus as well, such as maximum nominal stress criterion, quadratic stress criterion, maximum separation criterion, and quadratic separation criterion. In this thesis, the maximum nominal stress damage criterion is used. With this option, the damage will initiate when the maximal nominal stress exceeds the critical value, which is the maximum strength of the material. Figure 3.12 shows the typical traction-separation response

for all three directions to the contact faces. A separation can appear when the initiation criterion eq. (3.23) is satisfied. A more specific description of these techniques can be found in [58].

$$\max \left\{ \frac{\langle t_n \rangle}{t_n^*}, \frac{t_s}{t_n^*}, \frac{t_t}{t_t^*} \right\} = 1 \quad (3.23)$$

The subscripts n, s, t stand for normal, shear, and tangential components of the interfacial stress. The superscript * represents the maximum strength by the interface in the corresponding direction. The symbol $\langle \rangle$ represents the Macaulay bracket to signify that a purely compressive displacement (i.e., a contact penetration) or a purely compressive stress state does not initiate damage. Damage is assumed to initiate when the maximum nominal stress ratios; as defined in the eq. (3.23) reaches a value of one.

Damage evolution (separation propagation)

The damage evolution law describes the rate at which the cohesive stiffness is degraded once the corresponding initiation criterion is reached. A scalar damage variable, D, represents the overall damage at the contact point. It initially has a value of 0. If damage evolution is modeled, D monotonically evolves from 0 to 1 upon further loading after the initiation of damage. Either the maximal displacement or the fracture energy, which is the area under the curve in a graph of traction versus separation, must be specified. The normal and shear stresses components are affected by the damage according to [58]:

$$t_n = \begin{cases} (1-D)\bar{t}_n & \text{if } t_n \geq 0 \\ \bar{t}_n & \text{if } t_n < 0 \text{ (compression)} \end{cases} \quad (3.24)$$

$$t_s = (1-D)\bar{t}_s \quad (3.25)$$

$$t_t = (1-D)\bar{t}_t \quad (3.26)$$

Where \bar{t}_n , \bar{t}_s , and \bar{t}_t are the contact stress components predicted by the elastic traction-separation behavior for the current separations without damage. To describe the evolution of damage under a combination of normal and shear separations across the interface, an effective separation is defined according to [72] as:

$$\delta_m = \sqrt{\langle \delta_n \rangle^2 + \delta_s^2 + \delta_t^2} \quad (3.27)$$

In this thesis, it assumes linear softening for damage evolution zone

$$D = \frac{\delta_m^*}{\delta_m^u} \left(\frac{\delta_m^u - \delta_m^0}{\delta_m^* - \delta_m^0} \right) \quad (3.28)$$

Where δ_m^* refers to the maximum value of the effective separation attained during the loading history. While δ_m^u indicates the effective separation just before unloading.

The hatched area below the curve in Figure 3.12 provides the energy dissipated to produce a new pair of fully disconnected surfaces, so-called, the interface fracture toughness. The positioning of the interface weather for capsules or solidified healing agents with respect to the applied load can generate a mixed-mode propagation response of the cohesive interface. The propagation mixed mode involves different energies associated with the debonding

capability in normal (n) and parallel directions to the interface (s, t). The maximum fracture separation is then calculated by [72]:

$$\delta_n^* = \frac{2G_n^*}{t_n^0} \quad (3.29)$$

$$\delta_s^* = \frac{2G_s^*}{t_s^0} \quad (3.30)$$

$$\delta_t^* = \frac{2G_t^*}{t_t^0} \quad (3.31)$$

This thesis assumes that the interaction between the energies of each individual mode (i.e., n, s, t) follows the power law fracture criterion [72] given by:

$$\left\{ \frac{G_n}{G_n^*} \right\}^\alpha + \left\{ \frac{G_s}{G_s^*} \right\}^\alpha + \left\{ \frac{G_t}{G_t^*} \right\}^\alpha = 1 \quad (3.32)$$

Where G_n , G_s , G_t are the energy release rates calculated from the traction and normal, shear, tangential displacements during interface opening, and the power α is a cohesive property parameter that describes the interaction between modes. The properties G_n^* , G_s^* , G_t^* represent the critical interface toughness related to each direction separately. For the sake of simplicity, this thesis assumes that the critical fracture toughness is equal in all directions. Also, taking into account the effect of this parameter on the response, a value $\alpha = 1$ has been used [72].

Implementation in Abaqus

Models exhibiting various forms of softening behavior and stiffness degradation often lead to severe convergence difficulties in Abaqus. Viscous regularization of the constitutive equations defining surface-based cohesive behavior can be used to overcome some of these convergence difficulties. Viscous regularization damping causes the tangent stiffness matrix that defines the contact stresses to be positive for sufficiently small time increments. In this thesis viscosity coefficient value is taken 0.0001 [58].

Interactions, which are assigned a cohesive surface interaction property in Abaqus, are modeled with pure master-slave roles in the contact formulation. The master and slave roles are established as follows:

- The slave surface should be the more finely meshed surface.
- If the mesh densities are similar, the slave surface should be the surface with the softer underlying material [58].

There are two ways to define contact in Abaqus: (1) Contact pairs: the master and slave surfaces will specify manually. In this thesis the external surface of capsule or solidified healing agent defined as slave surfaces and the internal surface of the concrete matrix is defined as a master surface. (2) General contact: it is an automated algorithm which enforces contact in an average sense between interacting surfaces; Abaqus automatically assigns master and slave roles.

It is worth mentioning that there are some numerical convergence issues occurred related to the cohesive modeling behaviour in Abaqus such as:

- Time increment required is less than the minimum specified

In order to solve this issue the initial and minimum time increments should be defined as small values within Step module > Edit > Step-1 > Incrementation. In this thesis, the initial time increment is taken 1E-009 and the minimum time increment is taken 1E-015, see Figure 3.14.

- Too many attempts made for this increment

In order to solve this issue, the variable I_A which is the maximum number of cutbacks allowed for an increment within Step module > Other > General Solution Controls > Edit > Step-1 has to be changed to a higher number to allow many numerical attempts, in this thesis it is taken 30, see Figure 3.15.

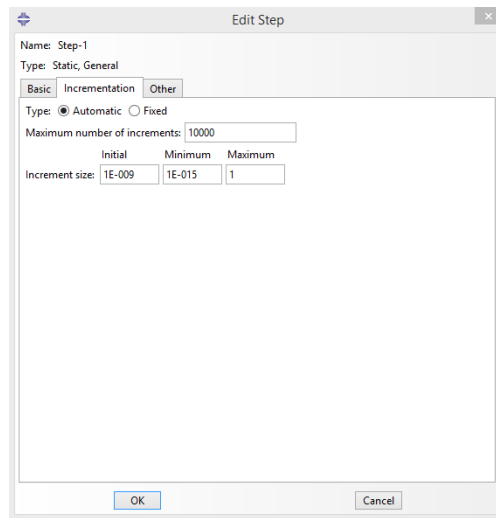


Figure 3.14: Adjustment of time incrementation in Abaqus Step module.

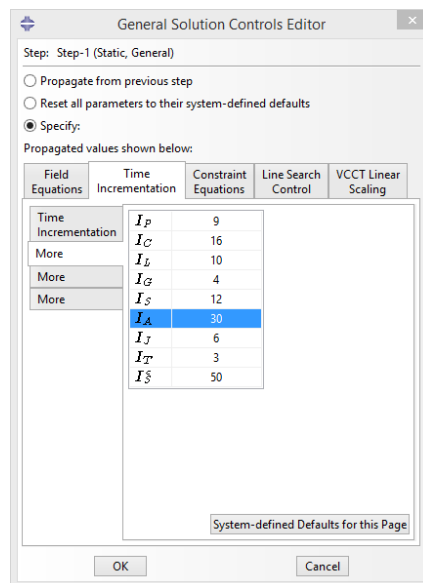


Figure 3.15: Adjustment of general solution controls in Abaqus Step module.

3.3.2 Cohesive element

The cohesive element approach is used to bond two different components with adhesive which has a finite thickness. In fact, the formulae and laws that govern cohesive constitutive behavior for cohesive element approach are quite similar to cohesive constitutive behavior of cohesive surface approach. The similarities extend to the linear elastic traction-separation model, damage initiation criteria, and damage evolution laws. However, to avoid repetition and for the sake of completeness, only the difference of modeling the cohesive element from the modeling of the cohesive surface will be discussed in this section as the cohesive element approach wasn't used in this thesis. There are some requirements for using this approach such as the cohesive zone must be discretized with a single layer of cohesive elements through the thickness. In addition, the cohesive elements are usually connected to the adjacent components by tie constraints as in most cases the mesh in the cohesive zone is not matched to the mesh of the adjacent components. Element deletion upon reaching a completely damaged state has to be activated in order to represent the damage in the modeling by removing the completely damaged elements [58].

The cohesive element approach is developed further to let it have a zero thickness; a so-called zero thickness cohesive element in order to insert it between every element interfaces in order to allow arbitrary crack propagation. It is also known as cohesive interface element (CIE). The CIE have been used to study the fracture interaction between the microcapsule and the concrete matrix and the possibility of debonding in encapsulation-based self-healing materials [73, 74]. But this approach has significant drawbacks such as introducing artificial compliance to the model and mesh dependency which has been reported in [75]. In addition, it required a script in order to generate zero thickness cohesive elements and insert them between the meshed elements at every element interfaces. A general comparison between cohesive element and cohesive surface approaches is summarized in Table 3.1.

Table 3.1: Comparison between cohesive element and cohesive surface approaches.

Simulation	Cohesive Element	Cohesive Surface
Preprocessing	<ul style="list-style-type: none"> - Direct control over the cohesive element mesh density and stiffness properties. - Tie constraints are used to connect with the adherend. - Constraints are enforced at the elements integration points. 	<ul style="list-style-type: none"> - Easily defined contact interaction. - Pure master-slave formulation is used. - Constraints are enforced at the slave nodes.
Initial configuration	<ul style="list-style-type: none"> - Must be bonded at the start of the analysis. - Once the interface has failed, the surfaces do not rebond. 	<ul style="list-style-type: none"> - Bond contact can be established anytime. - Debonded surfaces can be controlled whether it will stick or not stick if the contact occurs again.
Constitutive behaviour	<ul style="list-style-type: none"> - Allow for several constitutive behaviour types: <ul style="list-style-type: none"> - Traction-separation constitutive model. - Continuum-based constitutive model. - Uniaxial stress-based constitutive model. 	<ul style="list-style-type: none"> - Must use the traction-separation interface behaviour. - Intended for bonded interfaces where the interface thickness is negligibly small. - Only one failure mechanism is allowed.
Mass	<ul style="list-style-type: none"> - Mass must be defined. 	<ul style="list-style-type: none"> - No need to define mass. - Intended for thin adhesive interfaces; thus neglecting adhesive mass is appropriate for most applications.
Summary	<ul style="list-style-type: none"> - Recommended for relatively thick adhesive with a finite thickness. - Additional pre-processing effort is required and often increased the computational cost. 	<ul style="list-style-type: none"> - Recommended for infinitesimally thin layer adhesive. - Provides accurate, quick, and easy way to model adhesives connections.

4 Proposed Design of Microcapsules

4.1 Introduction

In this chapter, a simple proposed design method is developed to design the microcapsules size with consideration for a sufficient volume of healing agent to heal a specific crack width. It is based on the configuration of the Unit Cell (UC), Representative Volume Element (RVE), Periodic Boundary Conditions (PBC), and associates them with the volume fraction (V_f) and the crack width as variables. In addition, a short review about the used techniques such as unit cell (UC), Representative Volume Element (RVE), Periodic Boundary Conditions (PBC) is made for sake of completeness.

4.2 Representative Volume Element (RVE)

In the literature, there are several definitions of Representative Volume Element (RVE), and all of them related to its adequate size that represents the microstructure including both geometry and properties. RVE should be a statistically representative sample of the microstructure, i.e. it should include virtually a sampling of all possible microstructural configurations [76]. This definition leads to a considerable large RVE for a nonuniform microstructure which is computationally inefficient. Therefore, this definition is rarely used in actual homogenization analyses. Another definition characterizes RVE to be the smallest possible microstructure that sufficiently represents the overall macroscopic properties of interest such the constitutive relationship between stress and strain in a solid material. This definition leads to a much smaller RVE size than the statistical definition given before. The RVE satisfying this definition does not always include an adequate distribution of microfields in RVE. In summary, the RVE is the smallest element, representing the material structure, considered in the numerical simulation.

4.3 Unit Cell

The unit cell (UC) is a portion of material at its lower length scale which reproduces all other parts of the material through appropriate symmetry transformations, so that the UC and its images fill up the space the material occupies in exactly the same way as the original material does, without leaving any gap or causing any overlap. The existence of an appropriate UC implies strongly the presence of regularity in the architecture at the lower length scale of the material, which delivers the homogeneity of the material at its upper length scale. Homogeneity at the upper length scale can also result from the complete randomness of the architecture at the low length scale based on the statistic considerations. Because of the difference as stated, the use of UCs can be as a consequence of realistic modeling of the material architecture at its lower length scale, or an idealisation of the otherwise complete random structure at its lower length scale. An appropriate RVE, as discussed in the previous section, will have to be employed if the randomness in the lower length scale architecture has to be reflected in the model for the material at its upper length scale whose homogeneity is based on statistics [77].

4.4 Boundary Conditions (BC) types:

Within Finite element modeling there are different periodic boundary condition types:

4.4.1 Dirichlet boundary condition (e.g Displacement)

This type of boundary condition is applied directly onto the nodes of the external boundaries of the RVE and is suitable for displacement and temperature. As a result, it is one of the most common boundary condition types and it is usually called a first type boundary condition. It is named after a German mathematician, Johann Peter Gustav Lejeune Dirichlet [78].

4.4.2 Neumann boundary condition (e.g Pressure)

This type of boundary condition is like pressure, traction, and forces across the domain, so it is usually a result of a value through a domain like flux. It is named after a German mathematician, Carl Gottfried Neumann [78].

4.4.3 Mixed boundary condition (Combination of Dirichlet and Neuman BC)

This type of boundary condition is called mixed boundary condition, because in essence it is a combination of the previous boundary conditions; Dirichlet and Neuman. It was developed by French mathematician, Vitor Gustave Robin [78].

4.4.4 Periodic Boundary Conditions (PBC)

Periodic boundary conditions are usually used in micromechanics for the study of heterogeneous media. The periodic boundary condition (PBC) stipulates that opposite pairs of edges or surfaces on the boundary of an RVE should deform identically under a given loading history. The PBC basically prevents the constraint of enforcing edges to remain planar after deformation [78], as illustrated in Figure 4.1 for 2D RVE.

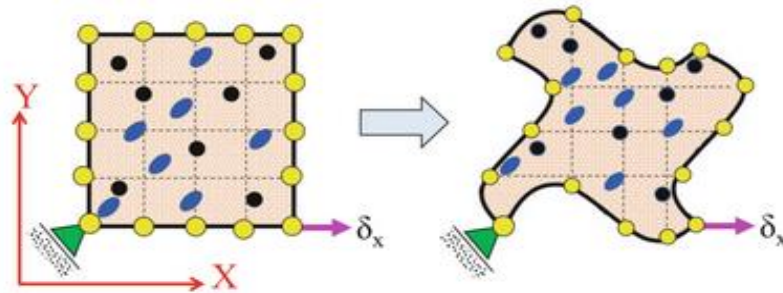


Figure 4.1: Typical periodic boundary conditions and the associated deformation shape [78].

In order to illustrate how the PBC can be implemented, consider 2D RVE as shown in Figure 4.2. The domain includes a heterogeneous material with boundary nodes N_1 to N_{16} . The virtual domain of 2D RVE is bounded by the boundary Ω :

$$\Omega = \Omega_L \cup \Omega_R \cup \Omega_T \cup \Omega_B \quad (4.1)$$

Where Ω_L , Ω_R , Ω_T , and Ω_B are the boundaries that enclose the left, right, top and bottom edges of the 2D RVE respectively. PBC required that the left boundary Ω_L deformation profile

must be similar in shape and value to the right boundary Ω_R . Similar deformation profiles are also expected for the top boundary Ω_T , and the bottom boundary Ω_B . Figure 4.1(left) shows the expected deformed shape for the domain. It should be noted that this deformation shape applies if the material is not homogeneous; otherwise the edges will be straight in which case the stiffness of the material will be constant throughout the virtual domain. The periodic boundary conditions of a model variable (ς) can be defined over the virtual domain (Ω) as follows:

$$\varsigma_{(x,y)}^{N_a} = \varsigma_{(x,y)}^{N_b} \text{ on the boundary } \Omega_k \quad (4.2)$$

Where N_a , and N_b are edge nodes that are kinematically linked on opposite edges and also where k represents L, R, T and B edges. With respect to the virtual domain shown in Figure 4.2, the model variable is a nodal displacement, i.e. $\varsigma = u_{(x,y)}$. The implication of the PBC equation is that all the nodes on one edge must match with the corresponding nodes on the opposite edge.

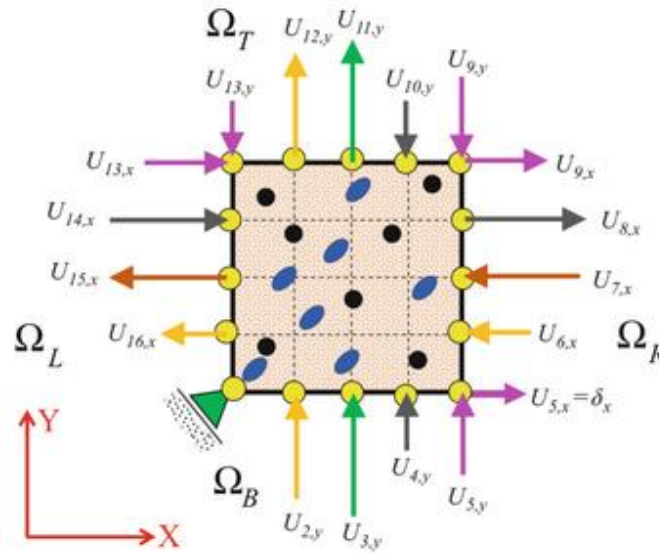


Figure 4.2: Virtual domain of RVE with PBC defined by displacements [78].

4.4.4.1 Implementation of PBC within FEM

The implementation of PBC within FEM is classified according to the type of mesh discretization. Generally, the mesh discretization could be a periodic or non-periodic mesh. Consider a plate with holes which is meshed differently, as illustrated in Figure 4.3. In the case of the periodic mesh, the number of nodes on one edge are equal to the number of nodes on the other edge, see Figure 4.3(a). In the other case non-periodic mesh, the number of nodes on one edge aren't equal to the number of nodes on the other edge, see Figure 4.3(b). The implementation of PBC on the non-periodic mesh has some complications and it is out of the scope of this thesis. Due to the proposed design method for the microcapsules based on the unit cell which it doesn't generate any complication with mesh discretization and the periodic mesh can be generated easily, so in this chapter, the implementation of PBC focused only on the periodic mesh.

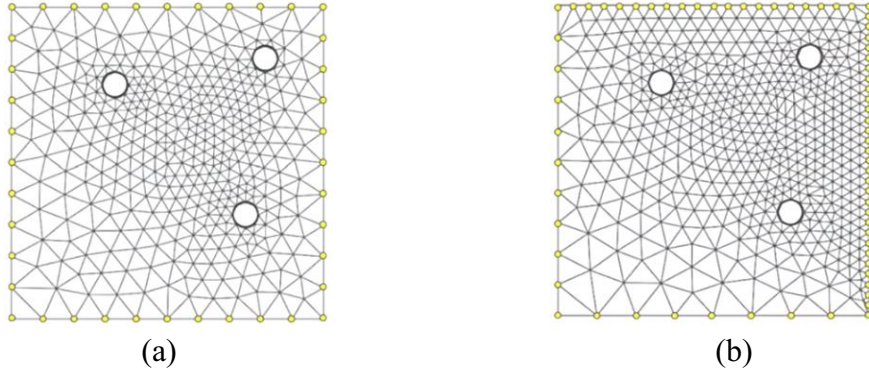


Figure 4.3: Periodic mesh (a) versus non-periodic mesh (b) [78].

In order to implement PBC on a periodic mesh, consider a 2D RVE which is pinned at one of the corner nodes N_1 to prevent rigid body motion, as illustrated in Figure 4.4. Every edge node should be linked kinematically on opposite edges. The principle is the displacement of node b must be equal to the displacement of node a and so on, as expressed in eq. (4.3) - (4.6).

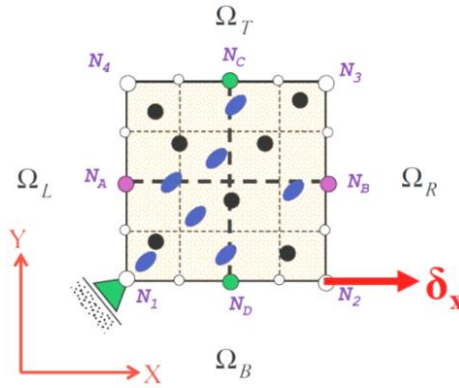


Figure 4.4: Implementation of PBC within periodic FEM mesh [78].

$$U_{(x,y)}^{N_B} = U_{(x,y)}^{N_A} \quad \text{hence} \quad U_{(x,y)}^{N_B} - U_{(x,y)}^{N_A} = 0 \quad (4.3)$$

$$U_{(x,y)}^{N_C} = U_{(x,y)}^{N_D} \quad \text{hence} \quad U_{(x,y)}^{N_C} - U_{(x,y)}^{N_D} = 0 \quad (4.4)$$

$$U_{(x,y)}^{N_2} = U_{(x,y)}^{N_1} \quad \text{hence} \quad U_{(x,y)}^{N_2} - U_{(x,y)}^{N_1} = 0 \quad (4.5)$$

$$U_{(x,y)}^{N_4} = U_{(x,y)}^{N_3} \quad \text{hence} \quad U_{(x,y)}^{N_4} - U_{(x,y)}^{N_3} = 0 \quad (4.6)$$

The boundary condition can be expressed into mathematical equations (canonical equations) where the displacements of the internal edge nodes are kinematically tied to the homogeneous displacements of the corner retained nodes. Note that N_3 isn't considered a retained node as its deformation is influenced by the deformations of nodes N_2 and N_4 , this is why it is called a slave or a dummy node. In order to enforce an axial deformation (δ_x), the displacements of corner retained nodes must be linked kinematically to the edge internal nodes. Because the loads are applied on the corner nodes, so the previous displacements boundary equations (canonical equations) can be rearranged as follows:

$$U_{(x,y)}^{N_B} - U_{(x,y)}^{N_A} - U_{(x,y)}^{N_2} + U_{(x,y)}^{N_1} = 0 \quad (4.7)$$

$$U_{(x,y)}^{N_C} - U_{(x,y)}^{N_D} - U_{(x,y)}^{N_4} + U_{(x,y)}^{N_3} = 0 \quad (4.8)$$

The PBC is imposed by applying the above canonical equations on the boundary nodes. So, if node 2 moves a certain distance, every other thing in the model will have a connection, there is a connectivity between them and so the system will respond accordingly. The canonical equations are introduced into Abaqus using a multifunction constraint equation in the interaction module. Due to the simulation here in 2D, the canonical equations need to define in two degree of freedom (DOF); x and y directions at every edge node as shown in Figure 4.5 and Figure 4.6 respectively for nodes N_B and N_A . The same principle is also applied on the top and bottom edges of RVE, for example, N_C and N_D linked kinematically to the corner nodes N_1 and N_4 .

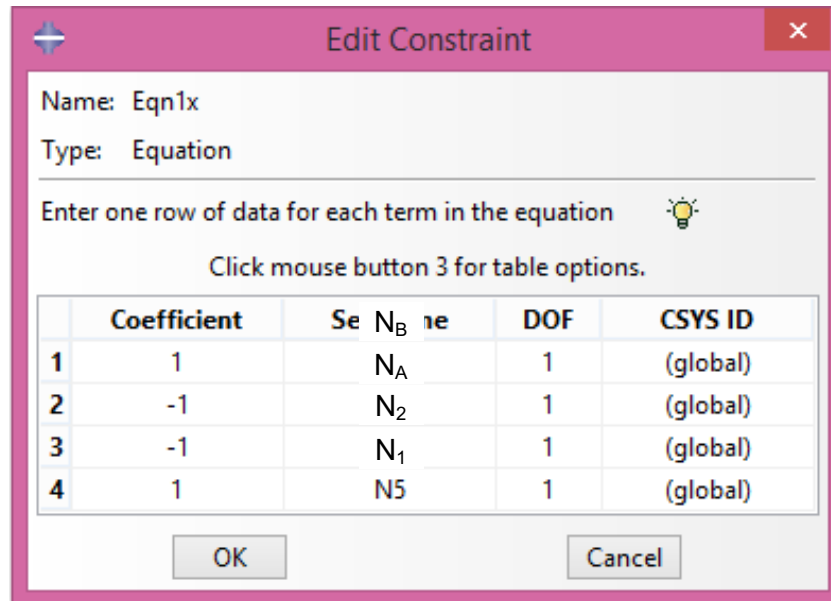


Figure 4.5: Constraint equations of PBC (x direction) in Abaqus interaction module.

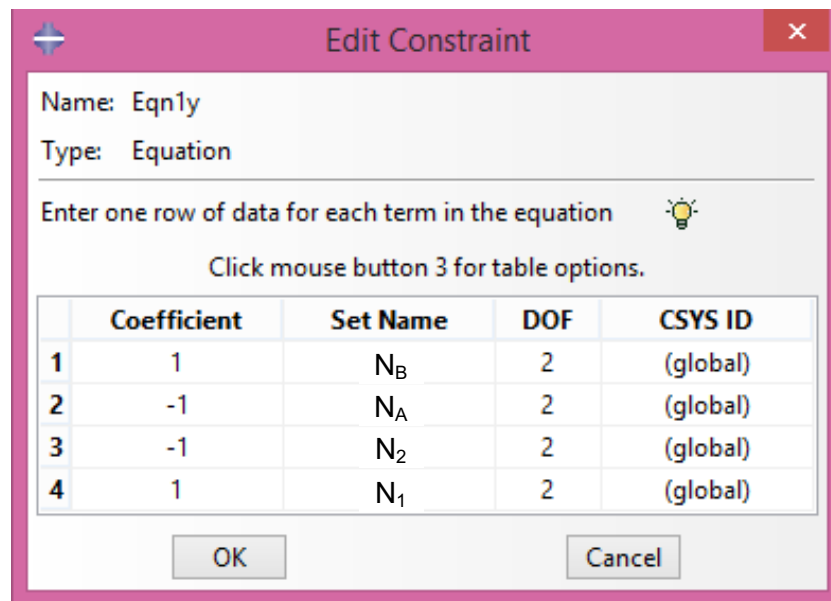


Figure 4.6: Constraint equations of PBC (y direction) in Abaqus interaction module.

4.5 Proposed Design Method of Microcapsules

It is assumed that the microcapsules are uniformly distributed in the concrete matrix. Therefore, the material can be represented using a representative volume element (RVE) with multiple uniform distributed microcapsules, as illustrated in Figure 4.7(a). Due to the regularity in the distribution of microcapsules, the material also can be represented using a unit cell (UC) with a single microcapsule as illustrated in Figure 4.7(b). The UC for this hypothesis is a cube, and includes a single microcapsule at its centroid. The three dimensions of the cube have the same length (L_{UC}) and at the same time it is equal to the interdistance between the periodic distributed microcapsules. The microcapsule dimensions are represented by the outer diameter (D) and the wall shell thickness (t_c). In order to model the fracture mechanism of this proposed design method of microcapsules, the periodic boundary conditions (PBC) should apply on the outer edges of the UC. Although the hypothesis of the uniform distribution microcapsules is somewhat far from the real random distribution of microcapsules, but it is suitable to provide a simple method to design the microcapsule based on the definition of the UC. However, the effects of microcapsule clustering on the fracture mechanism are studied computationally based on a simple developed approach in the next chapter.

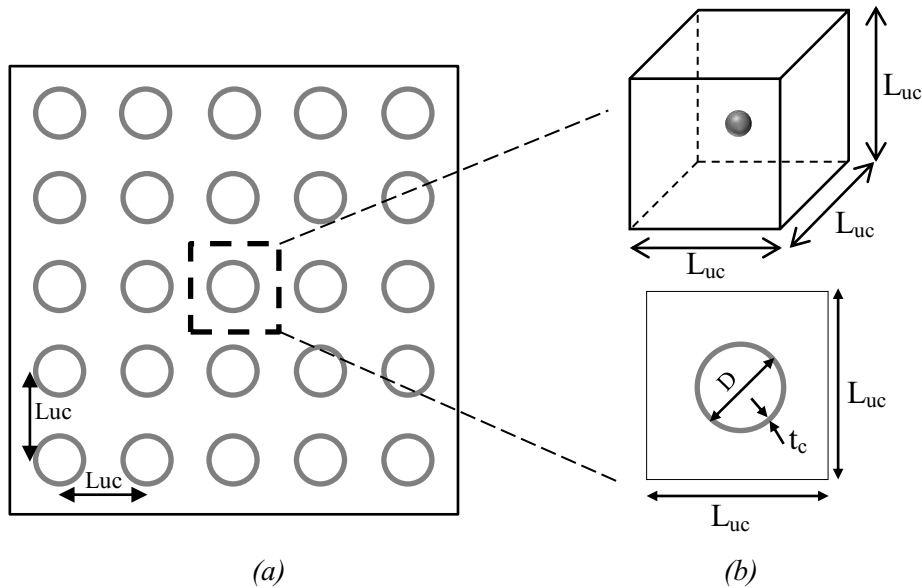


Figure 4.7: Geometry dimensions of (a) RVE and (b) UC of the proposed design method of microcapsules.

4.5.1 Virtual domain of the unit cell

The volume fraction (V_f) is a parameter which represents the volume ratio of the microcapsule to the unit cell (UC) of the concrete matrix, see eq. (4.11). While the volume of the microcapsule is calculated based on its outer diameter (D) as shown in eq. (4.9) and the volume of the unit cell shown in eq. (4.10).

$$V_c = \frac{\pi D^3}{6} \quad (4.9)$$

$$V_m = L_{uc}^3 \quad (4.10)$$

$$V_f = \frac{V_c}{V_m} \quad (4.11)$$

Substituting from eq. (4.9) and (4.10) into eq. (4.11), the V_f could be written in the following form:

$$V_f = \frac{\pi D^3}{6 L_{uc}^3} \quad (4.12)$$

From the eq. (4.12) the following equation of L_{uc} could be obtained:

$$L_{uc} = D \sqrt[3]{\frac{\pi}{6 V_f}} \quad (4.13)$$

This equation relates the dimension of UC (L_{uc}) which is equal to the distance between microcapsules to the microcapsule size represented by its diameter D . V_f can be estimated based on the expected crack width and the required volume of healing agent required to heal that crack.

4.5.2 The expected crack width of the unit cell

It is assumed that only one crack will be generated inside the unit cell and break the microcapsule. Therefore the healing agent encapsulated in a microcapsule, which, placed inside the UC, must be sufficient to heal the crack surface around it. Taking into account the roughness of the crack surface and the possibility that the healing agent will not completely released from the fractured microcapsule and there will be some healing agent remaining in it. So, it is assumed that the volume of the released healing agent is half of the microcapsule volume. Assuming also that the crack width (t_{cr}) is constant along the crack path, hence it can be calculated from the volume of the healed crack (V_{cr}) as follows:

$$V_{cr} = \frac{V_c}{2} = \left(L_{uc} - \frac{D}{2}\right)^2 t_{cr} \quad (4.14)$$

Based on the last two equations, for example, a range of volume fraction between 5% to 25% will be able to heal the crack width ranging from 0.18 mm to 0.86 mm.

5 Computational Modeling

5.1 Introduction

In this chapter, computational modeling is performed based on the XFEM and cohesive surface techniques to study the healing efficiency and the potential for the fracture or debonding of the microcapsules, or the solidified healing agents as well. In order to show the accuracy of these proposed techniques, a comparison with the zero thickness cohesive elements (CIE) has been conducted. The effects of microcapsule clustering on the fractured microcapsule are performed computationally. 3D computational simulations are performed and the obtained results are compared with the results obtained from 2D simulations to estimate the accuracy difference. In addition, computational simulations of the proposed microcapsule design method with different volume fraction (V_f), are performed and validated.

5.2 Healing Efficiency

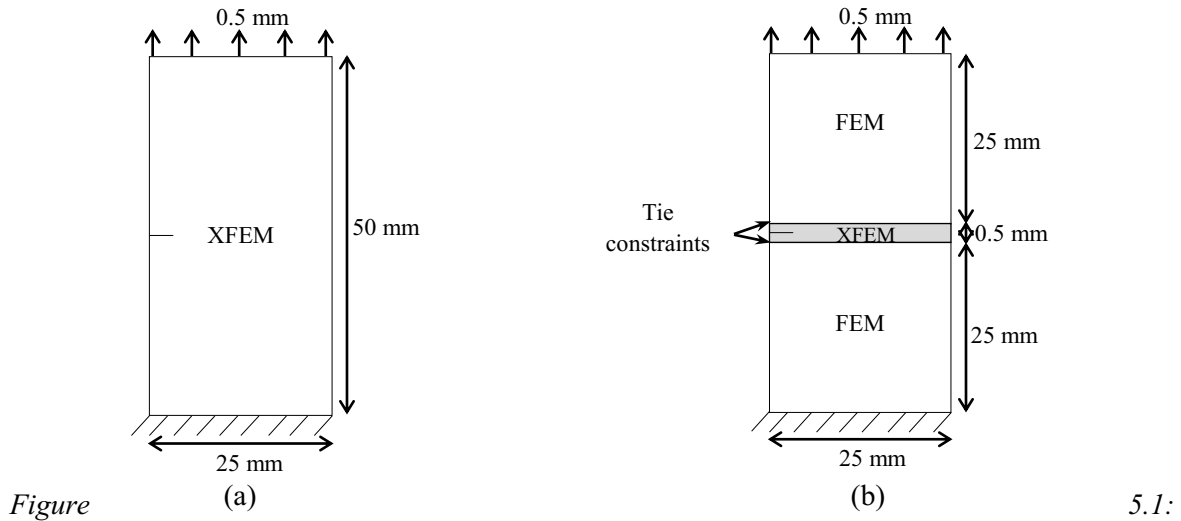
In this section, the healing efficiency of self-healing concrete is studied based on computational modeling for healed samples with solidified healing agents. The proposed modeling focused on the effects of healed-crack length on the overall healing efficiency of healed samples, and also the effects of interfacial fracture properties on fracture strength, on the load carrying capacity, and fracture or debonding probabilities of the solidified healing agents from the concrete matrix.

5.2.1 The effects of the healed crack length

5.2.1.1 Description of the model

2D specimens loaded under uniaxial tension. First specimen consists entirely from concrete and acts as a virgin concrete sample with dimensions of 50 mm x 25 mm and a precrack length is 4 mm in the middle of the sample. The whole virgin specimen is modeled by using the XFEM technique, which means that the enrichment zone is applied on the whole domain. The geometry dimensions of this sample with the boundary conditions are shown in Figure 5.1(a). The other specimens are healed samples where the width of the healed crack is 0.5 mm and with the variation of healed-crack length ratios; 100%, 75%, 50%, and 25%. The healed length with the smallest healed-crack ratio, (25%) has the smallest healed length which is equal to 25% of the cracked length and vice versa. The precrack length is 4 mm, and is placed in the middle of the healing thickness layer. The geometry dimensions of this sample with the boundary conditions are shown in Figure 5.1(b). Uniform displacements 0.5 mm was applied on the top surface of the specimens. The simulation was done in Abaqus/Static and the samples are meshed with Quadrilateral elements (Q4) elements assuming plane stress conditions. Every healed specimen is divided to three parts; top and bottom parts represent the concrete matrix which is divided by the crack path and the middle part represents the solidified healing agent. The top and bottom parts modeled by standard FEM. The middle part modeled by XFEM technique which means that the enrichment zone is applied only on the middle part. As the main focus this model is to study the effects of the healed crack length on the healing efficiency of the self-healing concrete specimen, so the contact surfaces between the three parts are assumed to be fully bonded and modeled by tie constraints. The material

properties listed in Table 5.1 characterized by [73, 79, 80]. Their parameters are then represented by the Young's modulus (E), Poisson's ratio (ν), maximum tensile strength (σ^*), and fracture energy (G_f).



Specimens geometry dimensions and modeling techniques (a) virgin concrete sample (b) healed concrete sample.

Table 5.1: The material properties.

Material	E (MPa)	ν	σ^* (MPa)	G_f (N/mm)
Concrete	25000	0.2	2.5	0.075
Healing agent (solidified)	3700	0.33	55	0.1

5.2.1.2 Study of the mesh size

In order to establish the degree of mesh refinement required to obtain reliable results, meshes of three different densities are modeled, as shown in Figure 5.2 have been conducted. The coarse mesh has 5200 elements consisting of 5000 elements for the concrete matrix and 200 for the healing agent. The medium mesh has 20800 elements consisting of 20000 elements for the concrete matrix and 800 for the healing agent. The fine mesh has 33050 elements consisting of 31250 elements for the concrete matrix and 1800 for the healing agent. Figure 5.4 shows the force displacement curves for each mesh discretization. The force displacement curves for the medium mesh and the fine mesh discretization are very close to each other. Therefore, the medium mesh discretization is employed for simulations and presenting the results in this study.

5.2.1.3 Parametric studies

Parametric studies of four different healed-crack length ratios with different healed crack lengths are performed to study the effects of the healed length of the crack on the load

carrying and overall healing efficiency of healed samples. The material parameters values in Table 5.1 are assigned to each part. Only one parameter, (L_h), which represents the healed length, was varied relative to the crack length which is equal to the sample width as the crack is propagated and divides the virgin sample into two parts while other parameters were fixed. The four healed-crack length ratios (L_h), range from 25% ($L_h = 6.25$ mm) to 100% ($L_h = 25$ mm), see Figure 5.3.

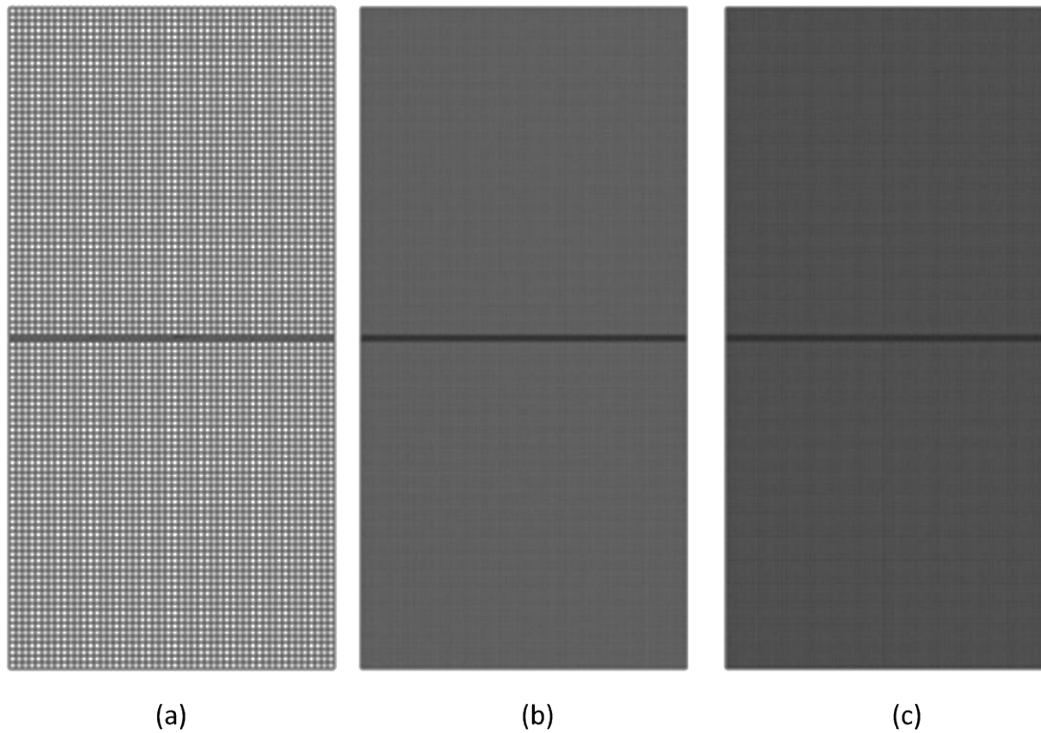


Figure 5.2: The mesh discretization with three different densities (a) Coarse mesh (5200 elements) (b) Medium mesh (20800 elements) (c) Fine mesh (33050 elements).

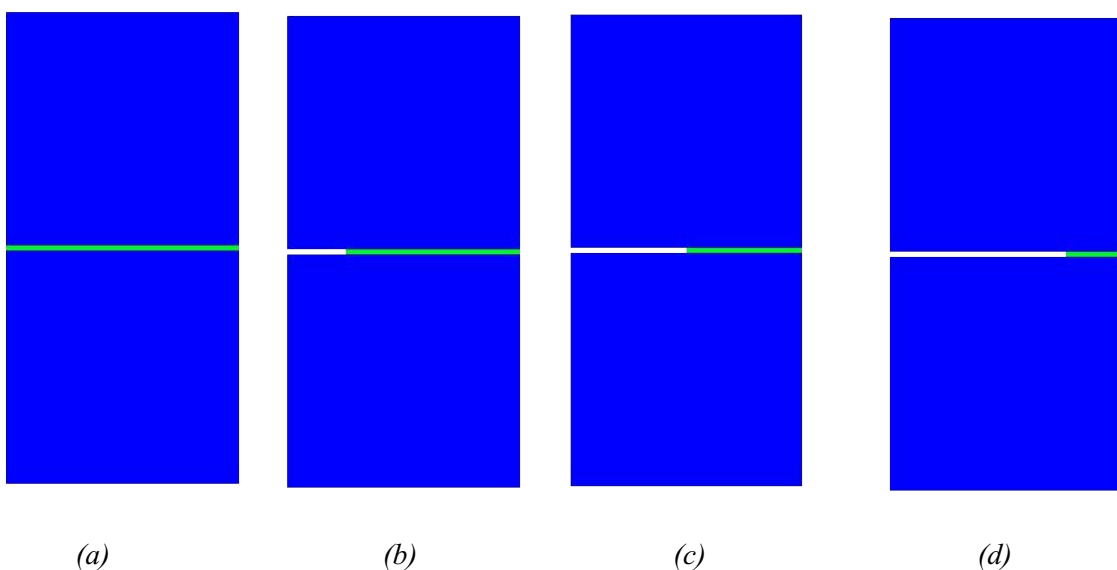


Figure 5.3: Healed samples with different healed-crack length L_h ratios (a) L_h 100% ($L_h = 25$ mm) (b) L_h 75% ($L_h = 18.75$ mm) (c) L_h 50% ($L_h = 12.5$ mm) (d) L_h 25% ($L_h = 6.25$ mm).

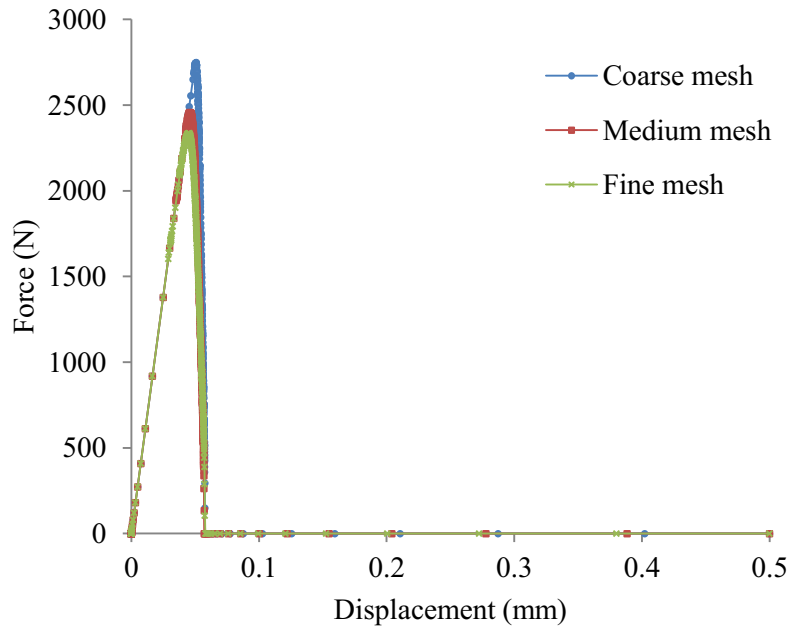


Figure 5.4: Force displacement curves from different mesh discretization.

5.2.1.4 Results and discussion

Figure 5.5 demonstrates the crack pattern for the virgin sample. While Figure 5.6 demonstrates the effects of the healed-crack length (L_h) on the crack pattern for the healed specimens. The length (L_h) is calculated as a percentage of the total length of the crack length which is equal to sample width after loading the virgin sample.



Figure 5.5: Crack pattern of virgin sample.

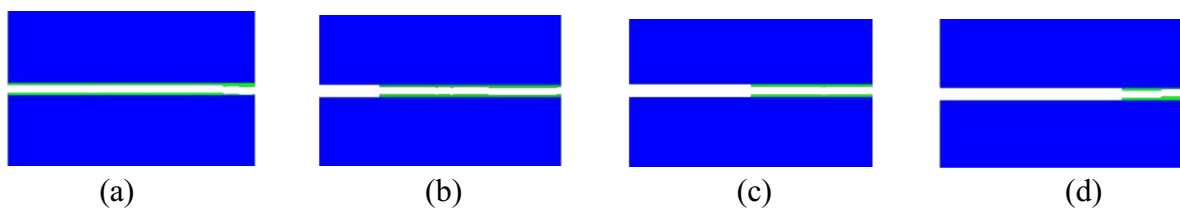


Figure 5.6: Crack pattern of four healed samples with different L_h ratios (a) L_h 100% ($L_h = 25$ mm) (b) L_h 75% ($L_h = 18.75$ mm) (c) L_h 50% ($L_h = 12.5$ mm) (d) L_h 25% ($L_h = 6.25$ mm).

Figure 5.7 shows the force displacement curve for the virgin sample. While Figure 5.8 shows the effects of the healed-crack length (L_h) on the load carrying capacity of the four samples with different healed-crack length ratios. These results display clearly that the healed-crack length affects significantly on the load carrying capacity of the specimen (specimen strength). It demonstrates the strength of the healed samples with variations of healed-crack length ranging from 25 mm (i.e. 100% of sample width) to 6.25 mm (i.e. 25% of sample width). The load carrying capacity of the specimen jumps from 562.92 N for L_h ratio 25% to 2457.18 N for L_h ratio 100%.

Figure 5.9 demonstrates clearly that the healed-crack length (L_h) has a significant role for governing the specimen strength as the higher percentage of healed-crack length to the total crack length leads to higher peak load. In spite of the low percentage of L_h 25% it has higher strength (562.92 N) compared to (268.97 N) for the virgin sample. That means with a lower ratio healed-crack length 25% its load carrying capacity is almost more than twice the load carrying capacity of the virgin sample.

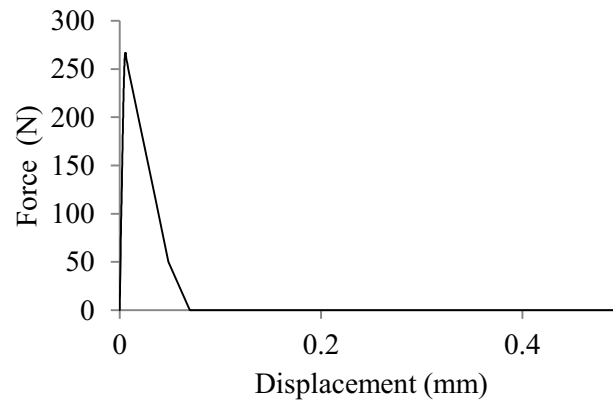


Figure 5.7: Force displacement curve of virgin sample.

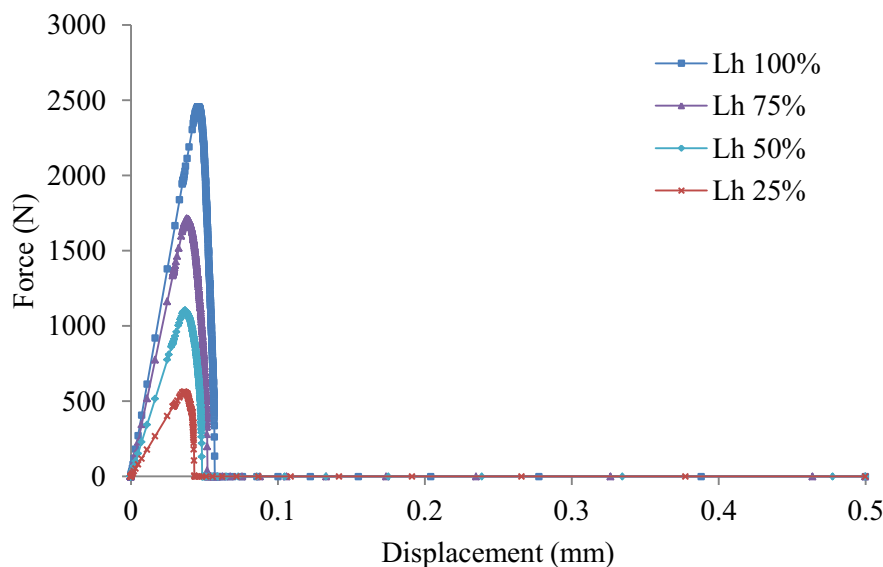


Figure 5.8: Force displacement curves of four healed samples with different L_h ratios.

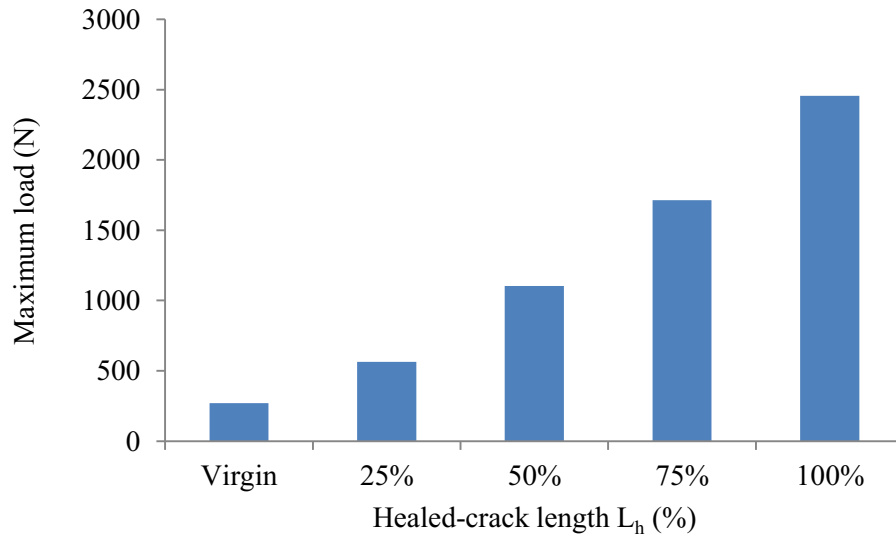


Figure 5.9: Effects of the L_h ratio to the maximum load of the specimens.

5.2.2 The effects of the interfacial fracture properties

5.2.2.1 Description of the model

2D specimens loaded under uniaxial tension from both sides top and bottom. The specimens represent healed samples with the width of the healed crack is 0.5 mm and with the variation of healed-crack length ratios; 100%, 75%, 50%, and 25%. The healed length with the smallest healed-crack ratio has the smallest healed length which is equal to 25% of the cracked length and vice versa. The geometry dimensions of this sample with the boundary conditions are shown in Figure 5.10. Uniform displacements 0.5 mm were applied on both top and bottom sides of the specimens. The simulation was done in Abaqus/Static and the samples are meshed with Quadrilateral elements (Q4) assuming plane stress conditions. Every healed specimen is divided into three parts; top and bottom parts represent the concrete matrix, which is divided by the crack path beforehand and the middle part represents the solidified healing agent. The three parts of each specimen are modeled by XFEM which means that there are three enrichment zones one for each part. The interactions between these parts are modeled by cohesive surface technique (CS). In order to investigate where the crack will initiate, therefore the preexisting crack with this type of analysis is not required. The material properties listed in Table 5.2 are characterized by [73, 79-81]. Their parameters are then represented by Young's modulus (E), Poisson's ratio (ν), maximum tensile strength (σ^*), and fracture energy (G_f).

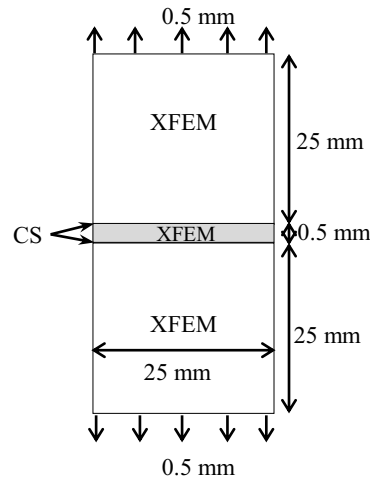


Figure 5.10: Specimens geometry dimensions and modeling techniques.

Table 5.2: The material properties.

Material	E (MPa)	ν	σ^* (MPa)	G_f (N/mm)
Concrete	25000	0.2	3.5	0.055
Healing agent (solidified)	3400	0.38	39	0.088
Interface	-	-	Varies	Varies

5.2.2.2 Study of the mesh size

In order to establish the degree of mesh refinement required to obtain reliable results, three different mesh densities are modeled, as shown in Figure 5.11 have been conducted. The coarse mesh has 42900 elements consisting of 42400 elements for the concrete matrix and 500 for the healing agent. The medium mesh has 56400 elements consisting of 55600 elements for the concrete matrix and 800 for the healing agent. The fine mesh has 87750 elements consisting of 86500 elements for the concrete matrix and 1250 for the healing agent. The Figure 5.13 shows the force displacement curves for each mesh discretization. The force displacement curves for the medium mesh and the fine mesh discretization are very close to each other. Therefore, the medium mesh discretization is employed for simulations and presenting the results in this study.

5.2.2.3 Parametric studies

Parametric studies of four different interfacial fracture properties are performed to study the effects of the interfacial fracture properties between the solidified healing agent and the cracked surfaces of the concrete specimen on the load carrying and overall healing efficiency of healed specimens with four different healed-crack length ratios. The four healed-crack length ratios (L_h) ranging from 25% ($L_h = 6.25$ mm) to 100% ($L_h = 25$ mm), see Figure 5.12. The material parameters values in Table 5.2 are assigned to each part. The interaction between the solidified healing agent and concrete matrix (i.e., the interfacial transition zone)

is defined as a cohesive surface. Only two parameters σ^* and G_f for the interfacial transition zone (itz) are varied relative to the properties of solidified healing agent for each simulation while the other parameters were fixed; i.e. they are ranging from 25% ($\sigma^* = 9.75$ Mpa, $G_f = 0.022$ N/mm) to 100% ($\sigma^* = 39$ Mpa, $G_f = 0.088$ N/mm).

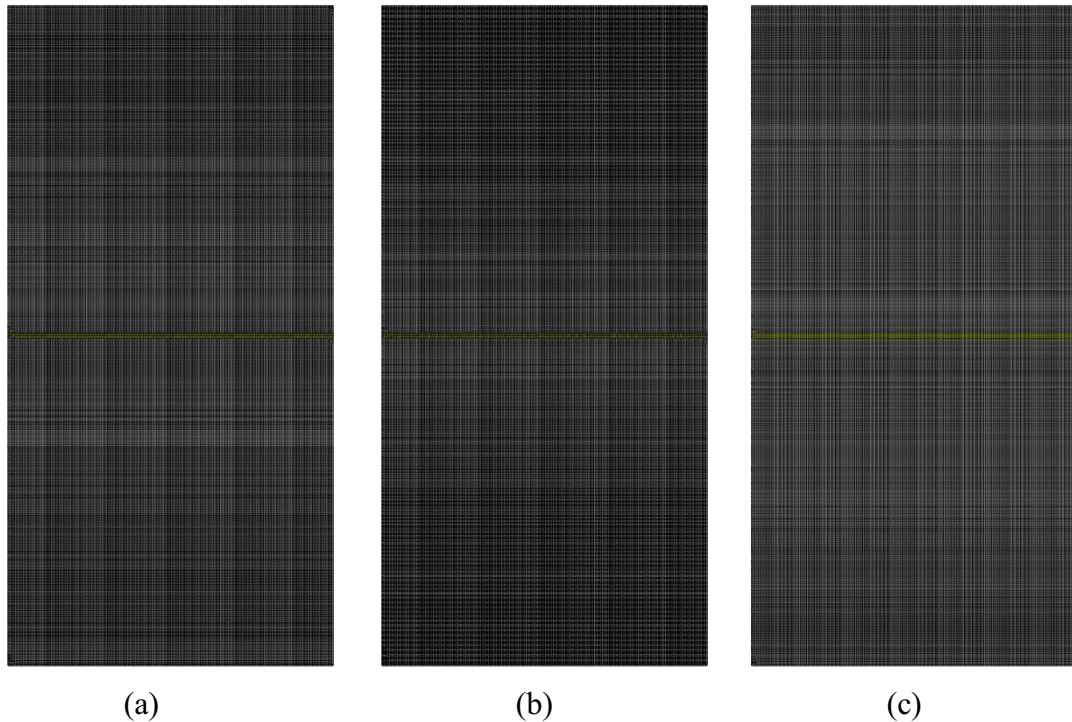


Figure 5.11: The mesh discretization with three different densities (a) Coarse mesh (42900 elements) (b) Medium mesh (56400 elements) (c) Fine mesh (87750 elements).

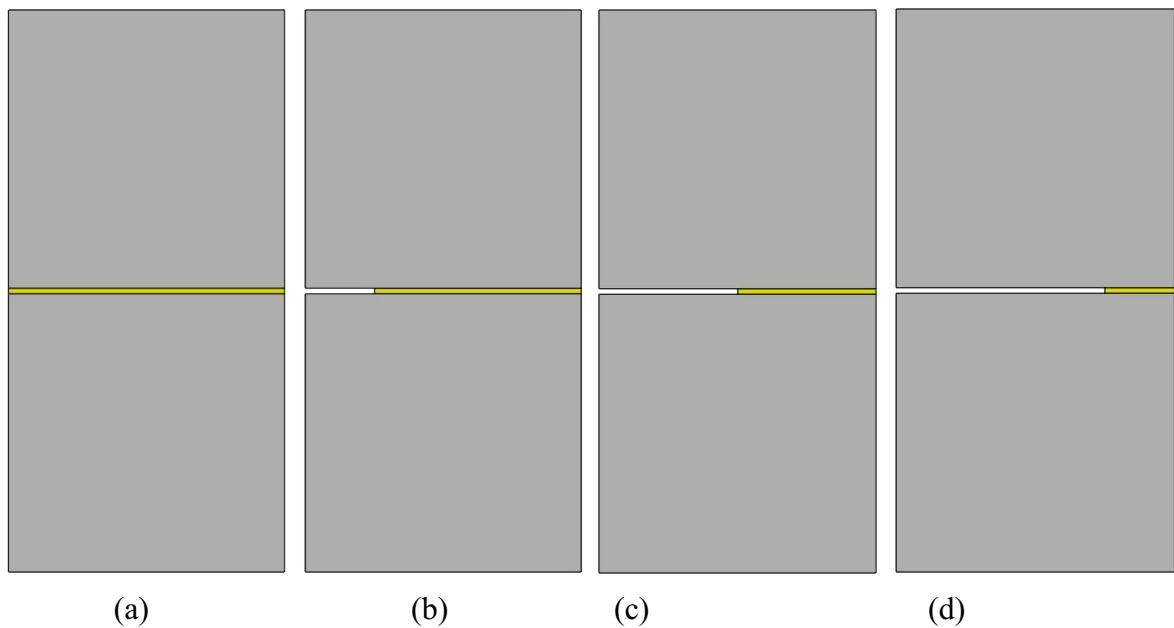


Figure 5.12: Healed samples with different healed-crack length L_h ratios (a) L_h 100% ($L_h = 25$ mm) (b) L_h 75% ($L_h = 18.75$ mm) (c) L_h 50% ($L_h = 12.5$ mm) (d) L_h 25% ($L_h = 6.25$ mm).

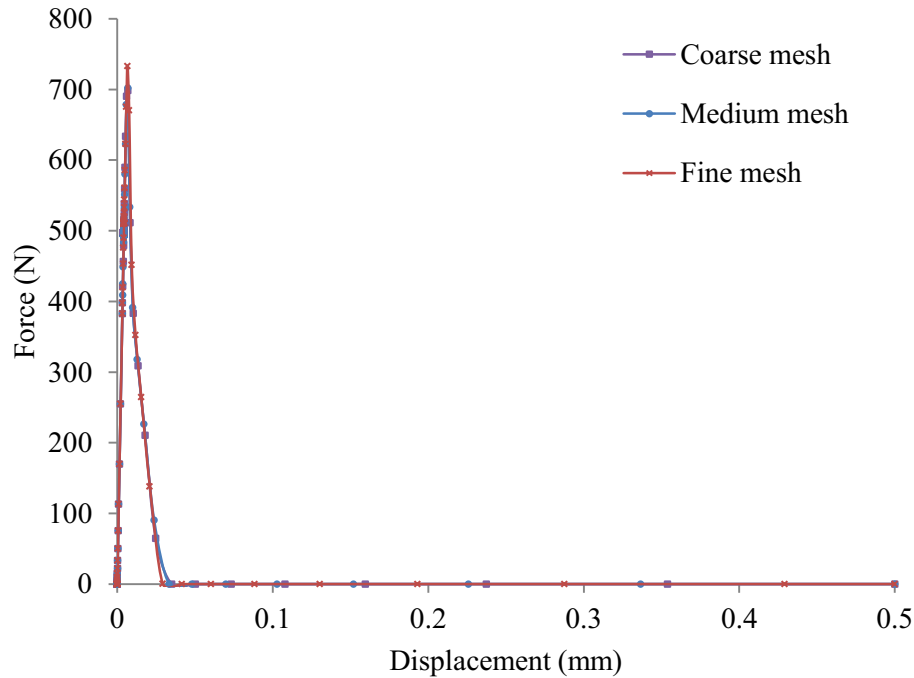


Figure 5.13: Force displacement curves from different mesh discretization.

5.2.2.4 Results and discussion

A. Effects of the interfacial fracture properties on the load carrying capacity

The effects of the interfacial fracture properties (itz) on the load carrying capacity for the four specimens with different healed-crack length ratios are shown in Figure 5.14 - Figure 5.17. It is clear that the load carrying capacity of the specimen is highly influenced by interfacial cohesive properties. Figure 5.14 - Figure 5.17 show the strength of the interfacial zone (itz) ranging from 9.75 MPa (i.e., 25% of the healing agent strength) to 39 MPa (same as healing agent) for healed-crack length ratios 100%, 75%, 50%, and 25%. Similarly, the fracture energy of the interfacial zone (itz) ranging from 0.022 N/mm (i.e., 25% of the healing agent fracture energy) to 0.088 N/mm (same as the healing agent). Figure 5.14 shows the effects of the interfacial fracture properties itz on the load carrying capacity of the specimen for the healed-crack length ratio 100%. The maximum load carried by the specimen decreased from 702.1 N for itz = 100% to 360.3 N for itz = 25%. So it is clear that the interfacial cohesive properties (itz) have a significant role for governing the load carrying capacity of the specimen. The same phenomenon also can be found in Figure 5.15, Figure 5.16, and Figure 5.17 for the healed-crack length ratios 75%, 50%, and 25%, respectively. It is clear that when the interfacial cohesive fracture properties have the same values of the healing agent, the higher maximum load will be achieved. Consequently, it is obvious that the higher the itz, the higher the load carrying capacity and vice versa.

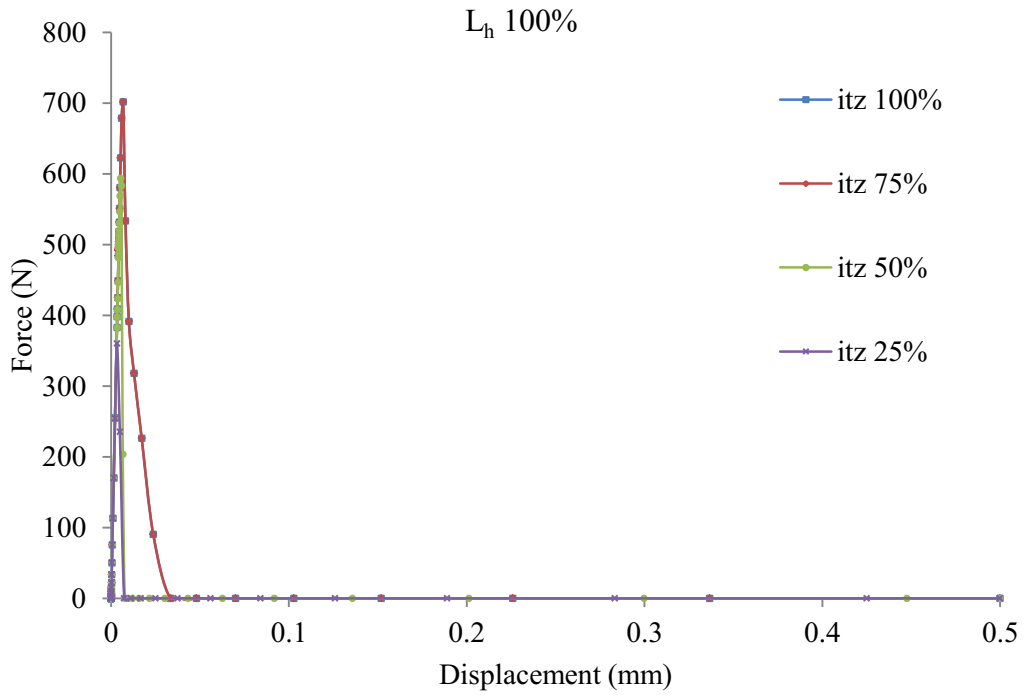


Figure 5.14: Force displacement curves of healed-crack length ratio L_h 100% with different itz ratios.

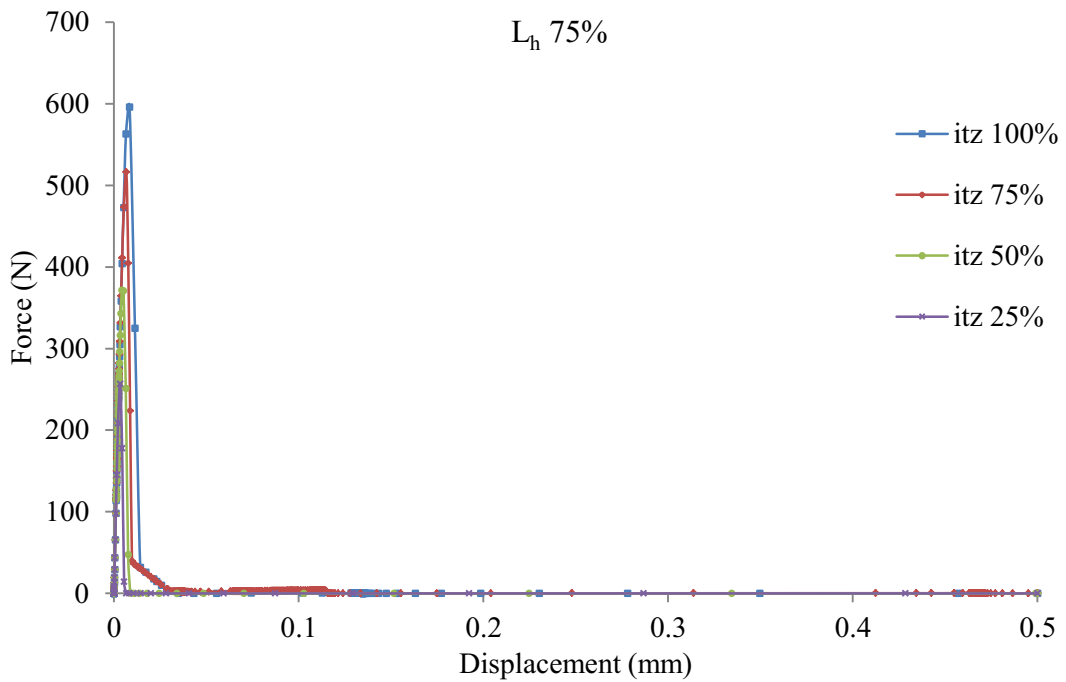


Figure 5.15: Force displacement curves of healed-crack length ratio L_h 75% with different itz ratios.

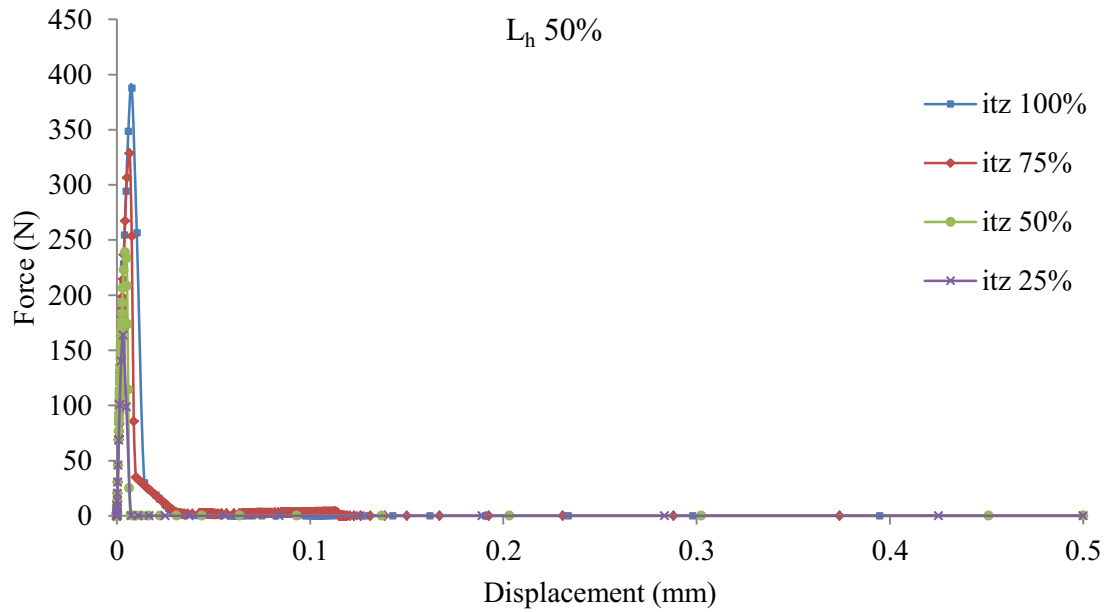


Figure 5.16: Force displacement curves of healed-crack length ratio L_h 50% with different itz ratios.

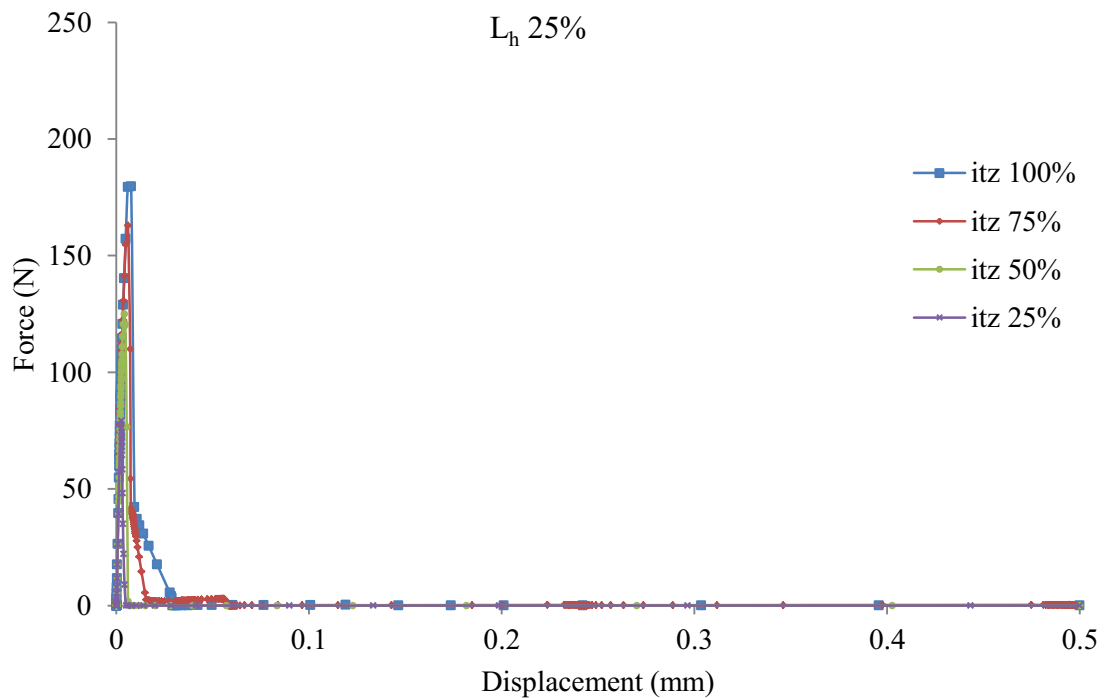


Figure 5.17: Force displacement curves of healed-crack length ratio L_h 25% with different itz ratios.

B. Effects of the healed-crack length on the load carrying capacity

The effects of the healed-crack length (L_h) on the load carrying capacity for the four specimens with different interfacial fracture properties (itz) ratios are shown in Figure 5.18 - Figure 5.21. It is clear that the load carrying capacity of the specimen is highly influenced by the healed-crack length (L_h). Figure 5.18 shows the effects of the healed-crack length (L_h) on the load carrying capacity of the specimen for the interfacial fracture properties ratio 100%.

The maximum load carried by the specimen decreased from 702.1 N for $L_h = 100\%$ to 179.6 N for $L_h = 25\%$. It is clear that the healed-crack length (L_h) has a significant role for governing the load carrying capacity of the specimen. The same phenomenon also can be found in Figure 5.19, Figure 5.20, and Figure 5.21 for the interfacial fracture properties ratios 75%, 50%, and 25%, respectively. It is clear that when the healed-crack length is equal to the crack length, then the higher maximum load carrying capacity will be achieved. Consequently, these results show that the higher the L_h , the higher the load carrying capacity and vice versa.

Figure 5.22 shows the relationship between the maximum carrying load and the itz percentage of interfacial fracture properties for different healed-crack length ratios. It is shown clearly that the higher percentage of itz increases the maximum load of the specimen that it can withstand. The higher healed-crack length ratio, the higher maximum carrying load of the specimen.

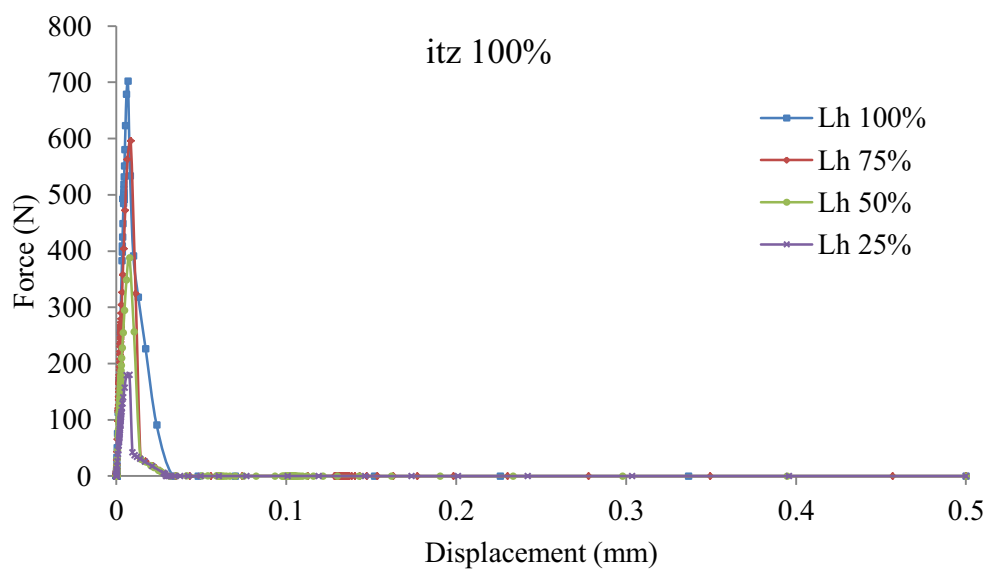


Figure 5.18: Force displacement curves of interfacial fracture ratio itz 100% with different L_h ratios.

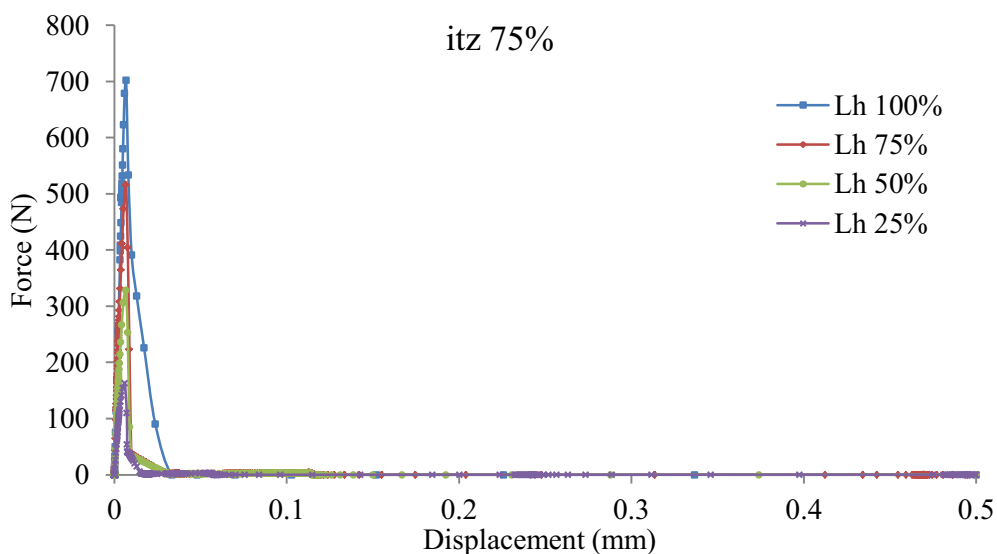


Figure 5.19: Force displacement curves of interfacial fracture ratio itz 75% with different L_h ratio.

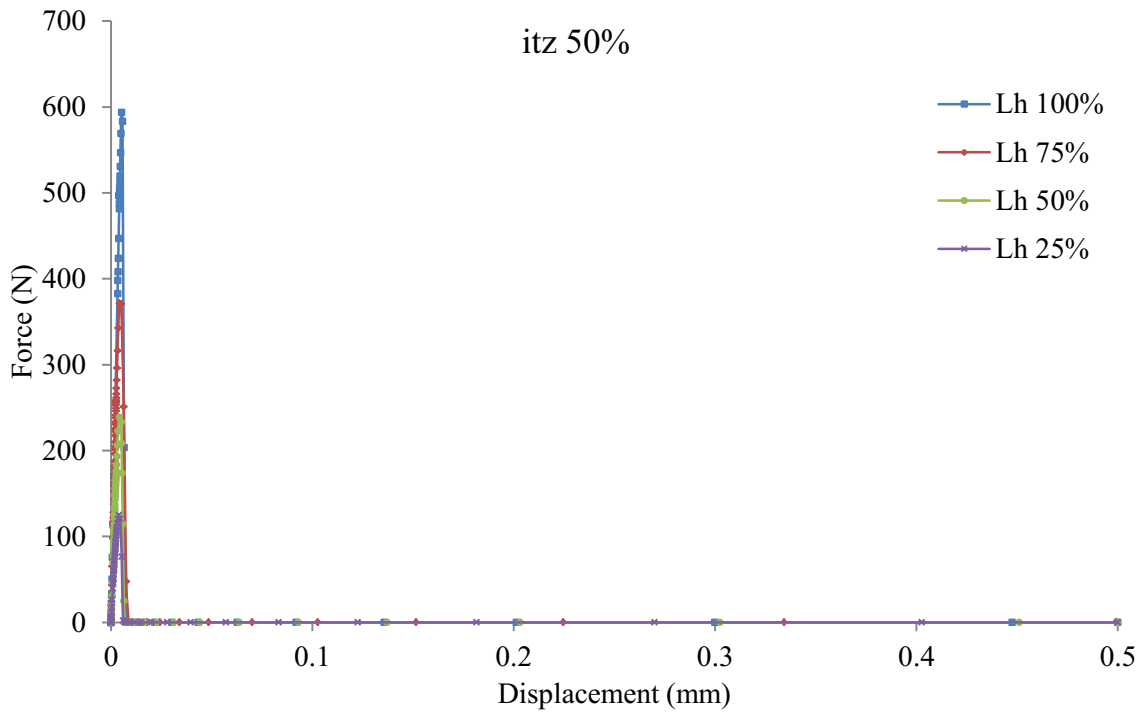


Figure 5.20: Force displacement curves of interfacial fracture ratio itz 50% with different L_h ratio.

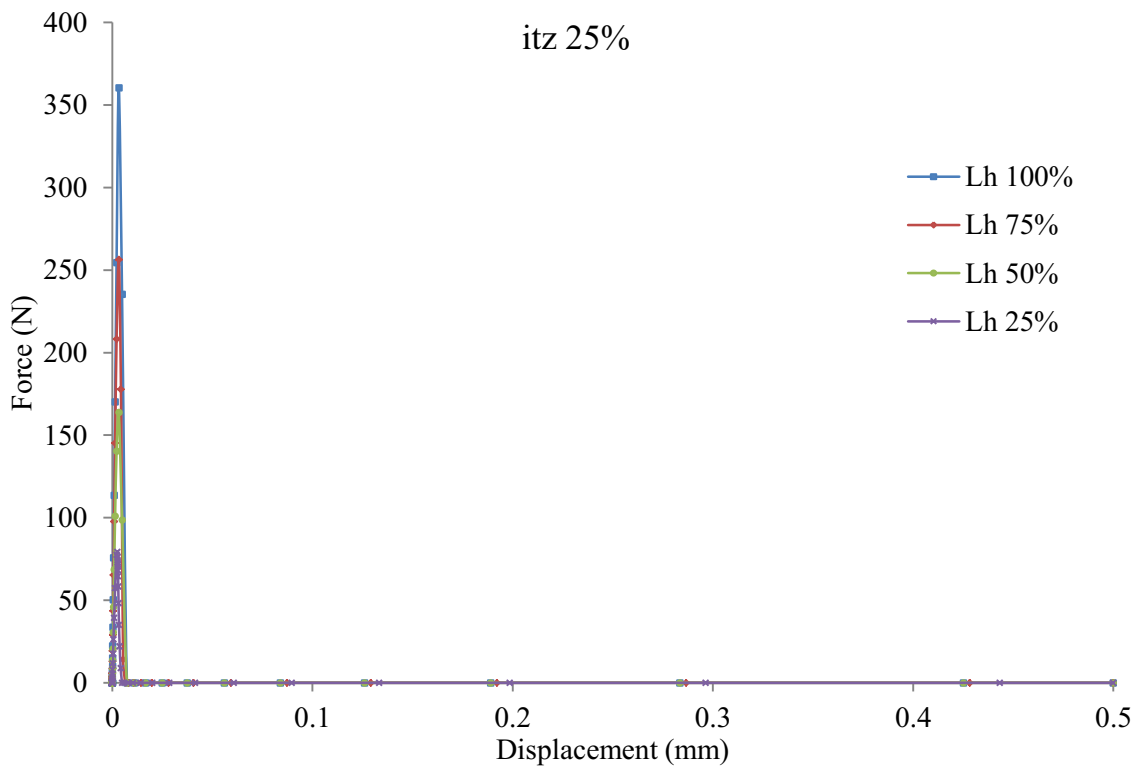


Figure 5.21: Force displacement curves of interfacial fracture ratio itz 25% with different L_h ratio.

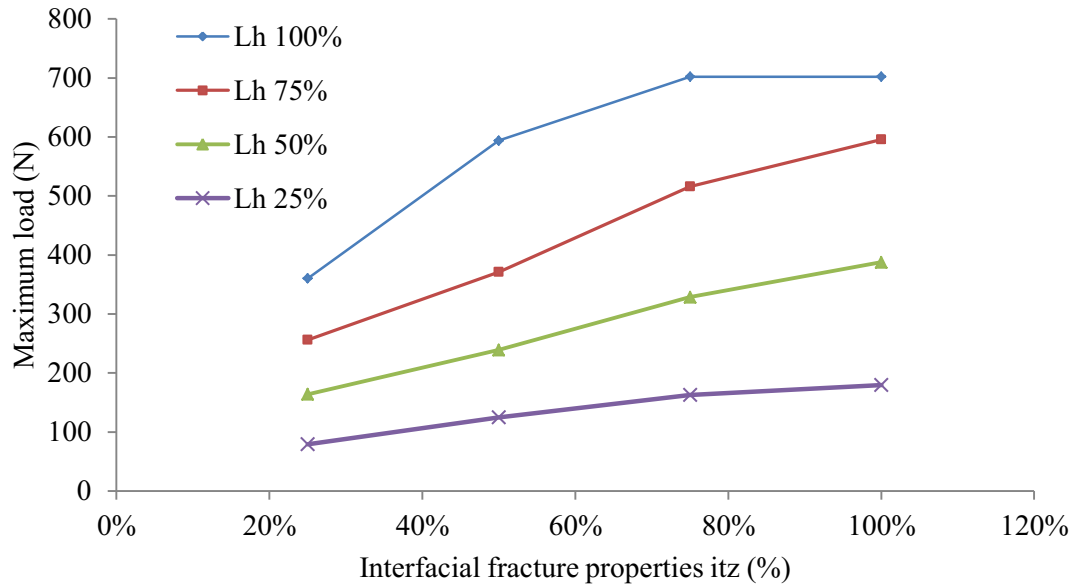


Figure 5.22: Effects of the healed-crack length ratio L_h and the itz percentage on the maximum load.

C. Effects of the interfacial fracture properties and the healed-crack length on the crack pattern

The effects of the interfacial fracture properties (itz) on the crack pattern for specimen with healed-crack length ratios 100%, 75%, 50%, 25% are shown in Figure 5.23, Figure 5.24, Figure 5.25, and Figure 5.26 respectively. Figure 5.23 demonstrates the crack patterns propagated in the healed specimens with the healed-crack length ratio L_h 100% associated with variation of the interfacial fracture ratios (itz) 100%, 75%, 50%, 25%. The specimens with itz 100% and 75% produced the same crack patterns as the crack initiated and propagated through the concrete matrix only which can be observed from Figure 5.23(a) and (b). When the percentage of itz range from 0%–25% of the fracture properties of the solidified healing agent, interfacial cracks occur and the solidified healing agent is debonded from the concrete matrix as illustrated in Figure 5.23(d). An interesting fracture pattern occurred when itz is 50% as an interfacial crack initiated and propagated through the contact surface between the solidified healing agent and the concrete matrix in addition to another crack initiating and propagating through the concrete matrix, as illustrated in Figure 5.23(c). That means a possibility for developing interfacial cracks and concrete cracks at the same time when the interfacial fracture properties are 50% of the solidified healing agent fracture properties.

Figure 5.24 - Figure 5.26 produced the same crack patterns propagated in the healed specimens with the healed-crack length ratios L_h 75%, 50%, and 25% respectively associated with variation of the interfacial fracture ratios (itz) 100%, 75%, 50%, 25%. When the percentage of itz to the fracture properties of the solidified healing agent ranging from 100%–75%, the crack initiated and propagated through the concrete matrix first, then the crack moved towards the contact surface between the solidified healing agent and the concrete matrix, and became an interfacial crack separating them till the end of the simulation, as illustrated in Figure 5.24(a-b) - Figure 5.26(a-b). That means mixed crack patterns are developed when the percentage of L_h ranges from 75%–25%, with the percentage of itz

ranging from 100%–75% as the first part is a concrete crack initiated and propagated through the concrete matrix and the second part is an interfacial crack propagated through the interface zone between the healing agent and the concrete matrix. On the contrary, when the percentage of itz range from 0%–25% of the fracture properties of the solidified healing agent, interfacial cracks occur and the solidified healing agent is debonded from the concrete matrix as illustrated in Figure 5.24(d) - Figure 5.26(d). Another interesting fracture pattern occurred when itz 50% as an interfacial crack initiated and propagated through the contact surface between the solidified healing agent and the concrete matrix in addition to another crack initiating and propagating through the concrete matrix, as illustrated in Figure 5.24(c) - Figure 5.26(c). That means a possibility for developing interfacial cracks and concrete cracks at the same time when the interfacial fracture properties are 50% of the solidified healing agent fracture properties.

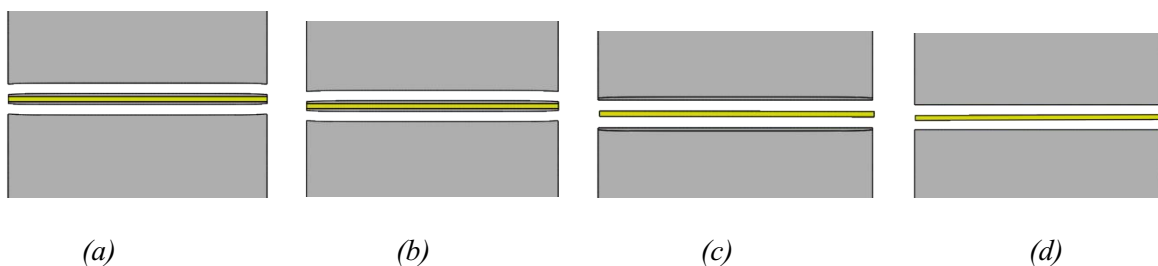


Figure 5.23: Crack pattern of L_h 100% specimen with different itz ratios. (a) itz = 100% (b) itz = 75% (c) itz = 50% (d) itz = 25%.

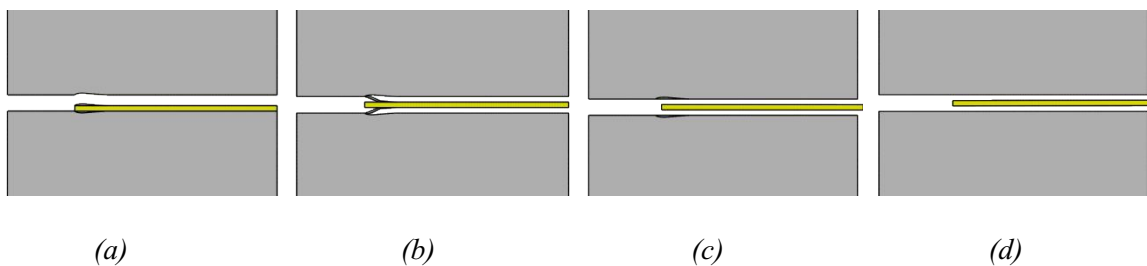


Figure 5.24: Crack pattern of L_h 75% specimen with different itz ratios. (a) itz = 100% (b) itz = 75% (c) itz = 50% (d) itz = 25%.

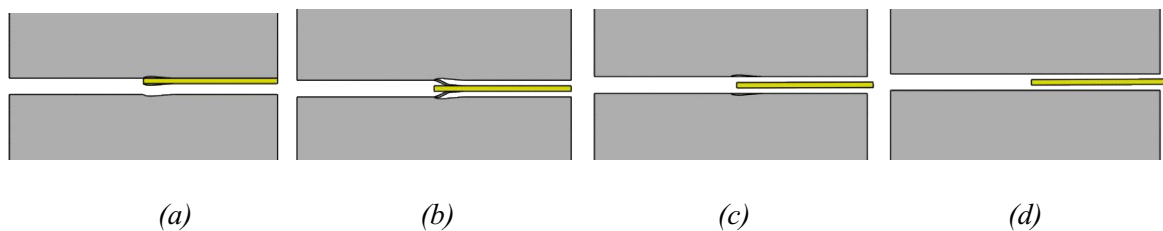


Figure 5.25: Crack pattern of L_h 50% specimen with different itz ratios. (a) itz = 100% (b) itz = 75% (c) itz = 50% (d) itz = 25%.

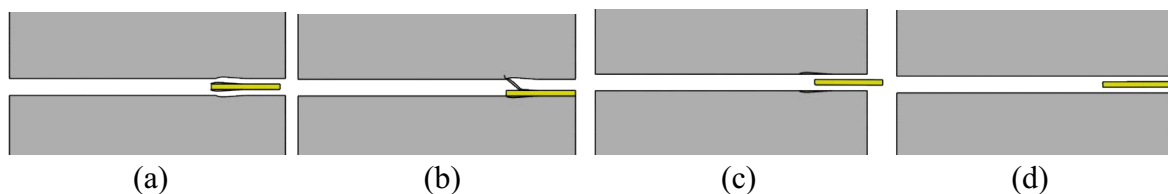


Figure 5.26: Crack pattern of L_h 25% specimen with different itz ratios. (a) itz = 100% (b) itz = 75% (c) itz = 50% (d) itz = 25%.

5.3 2D Microcapsules Fracture

In this section, the effects of interfacial fracture energy and strength on fractured microcapsules are studied computationally. The modeling focused on studying the effects of interaction surface between the microcapsule shell and the concrete matrix, on the load carrying capacity and the probability of fracture and debonding of the microcapsule from the concrete matrix.

5.3.1 The Effects of interfacial fracture energy

5.3.1.1 Description of the model

2D precracked concrete specimens with one microcapsule loaded under uniaxial tension. The dimensions of the specimens are 50 mm x 25 mm and the diameter of the microcapsule is 2 mm with shell thickness 0.1 mm. The precrack length is 4 mm is placed at the middle of the specimens' heights. The overall geometry dimensions of this sample with the boundary conditions are shown in Figure 5.27. Uniform displacement 0.1 mm was applied on the top surface of the specimens. The simulation was done in Abaqus/Static and the samples are meshed with Quadrilateral elements (Q4) assuming plane stress conditions. The material properties listed in Table 5.3 are characterized by [71, 73, 79, 80]. Their parameters are then represented by Young's modulus (E), Poisson's ratio (ν), maximum tensile strength (σ^*), and fracture energy (G_f). For the cohesive surface representing the interaction between the microcapsule and the concrete matrix, the normal and shear fracture properties are assumed to be equal due to the lack of experimental data available in the literature.

In order to establish the degree of mesh refinement required to obtain reliable results, several preliminary calculations using a notched sample without microcapsule have been studied. Overall, all element sizes here tested are well below the value ruled by the critical element size discussed in [82]. The outer size mesh of the matrix is 1 mm, the single bias seed technique used to guarantee the smooth mesh transition between the outer coarse mesh and the inner fine mesh around the microcapsule opening max. 1 mm and min. 0.2 mm and the circumferential length 0.25 mm around the microcapsule opening. The recommendations for meshing capsules according to [79] have been considered and the number of elements through the thickness of the microcapsule was fixed to 4 and the circumferential length 0.05 mm to compromise between accuracy and computational effort as shown in Figure 5.28.

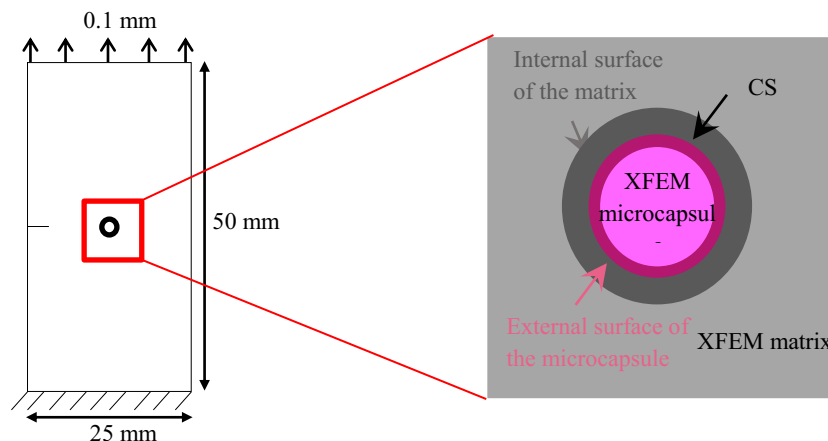


Figure 5.27: Specimens geometry dimensions and modeling techniques.

Table 5.3: The material properties.

Material	E (MPa)	ν	σ^* (MPa)	G_f (N/mm)
Concrete	25000	0.2	6	0.06
Capsule	3600	0.3	10	0.1
Interface	-	-	Varies	Varies

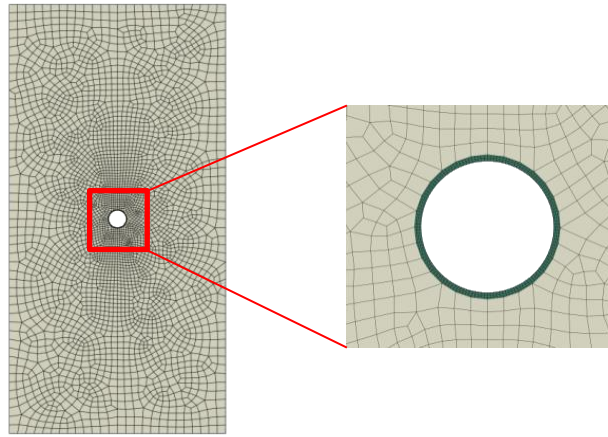


Figure 5.28: The meshing of the specimens.

5.3.1.2 Parametric studies

Parametric studies of different interfacial fracture properties are performed to study the effects of the interfacial transition zone (itz) between the microcapsule shell and the concrete matrix on the load carrying and the crack patterns. The cohesive surface between the microcapsule shell and the concrete matrix is defined by only two parameters which represent the interfacial fracture properties; the maximum interfacial tensile strength σ^* , which is known as the bonding strength, as well and the interfacial fracture energy G_f . In order to investigate the effects of interfacial strength and fracture energy, parametric studies of six different material inputs for σ^* and G_f were carried out. These two parameters for the interfacial transition zone (itz) are varied relative to the properties of the concrete for each simulation, while the other parameters are constant. itz ranging from 5% ($\sigma^* = 0.3$ Mpa, $G_f = 0.003$ N/mm) to 100% ($\sigma^* = 6$ Mpa, $G_f = 0.06$ N/mm) while the values of the other material properties are listed in Table 5.3. In order to study the effects of the interface fracture energy on the interfacial strength, the values of G_f are varied relative to the properties of the concrete for each simulation, while the interfacial strength remains fixed with other parameters as well.

5.3.1.3 Results and discussion

A. Effects of interfacial fracture properties on the load carrying capacity

The effects of the interfacial fracture properties (itz) on the load carrying capacity for the six specimens with itz ratios are shown in Figure 5.29. It is clear that the load carrying capacity of the specimen is highly affected by interfacial cohesive properties. Figure 5.29 shows the interfacial fracture properties (itz) ranging from 5% of concrete fracture properties ($\sigma^* = 0.3$ Mpa, $G_f = 0.003$ N/mm) to 100%; same as concrete fracture properties ($\sigma^* = 6$ Mpa, $G_f = 0.06$ N/mm). The maximum load carried by the specimen decreased from 105.6 N for itz = 100% to 104.1 N for itz = 5%. That means when the cohesive properties of the interface between the microcapsule and the concrete matrix are the same, the specimen strength will reach the higher value. Consequently, the higher the itz ratio, the greater the load carrying capacity of the specimen and vice versa. Figure 5.30 shows the force displacement curves with different G_f values with respect to fixed interfacial strength values. For example, Figure 5 (a) shows the force displacement curves with different G_f values ranging from 0.06 N/mm (i.e., 100 % of concrete fracture energy) to 0.003 N/mm (i.e., 5% of concrete fracture energy) with respect to interfacial strength σ^* value 6.0 MPa (same as concrete matrix). From Figure 5 (a) can be easily noticed that the curves coincide and the peak load is the same 105.6 N regardless the value of G_f . The same principle applied for Figure 5 (b), (c), (d), (e), and (f), except the peak load changes with respect to interfacial strength from 105.59 N for $\sigma^* = 75\%$ to 103.86 N for $\sigma^* = 5\%$. So, it is clear that the interfacial fracture energy has no effect on the load carrying capacity of the specimens.

Figure 5.31 shows the force displacement curves with different σ^* values with respect to fixed interfacial fracture energy. For example, Figure 6 (a) shows the force displacement curves for interfacial fracture energy 0.06 N/mm (same as concrete matrix) with different σ^* values ranging from 6 MPa (same as concrete matrix) to 0.3 MPa (i.e., 5% of concrete strength). The specimen strength increased from 104.1 N for $\sigma^* = 5\%$ to 105.6 N for $\sigma^* = 100\%$. The same principle is applied for Figure 5.31 (b), (c), (d), (e), and (f). As a result, it is clear that the interfacial fracture strength is the dominant factor governing the load carrying capacity of the specimen.

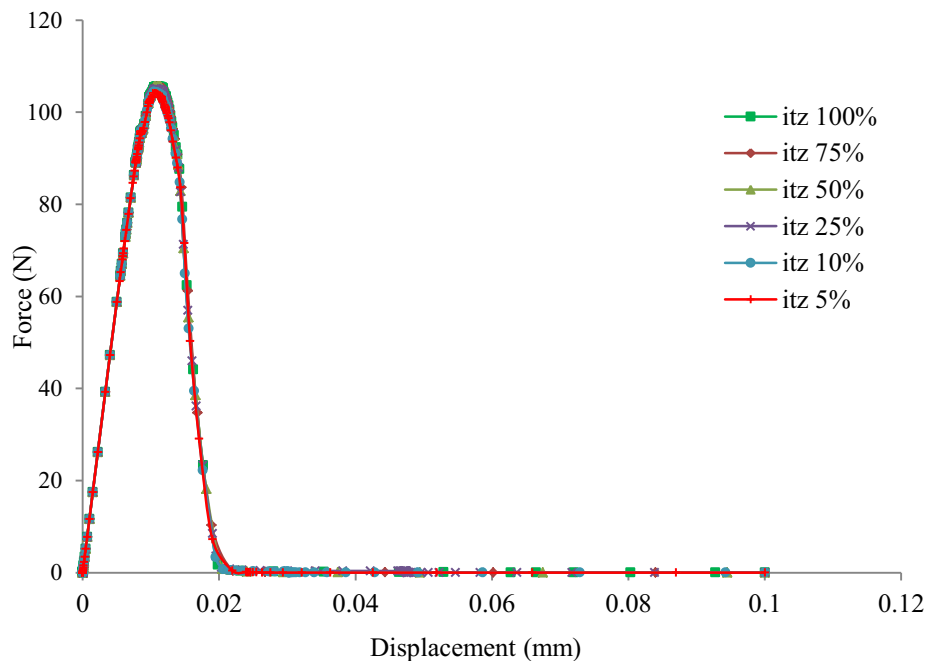


Figure 5.29: Force displacement curves with different itz values.

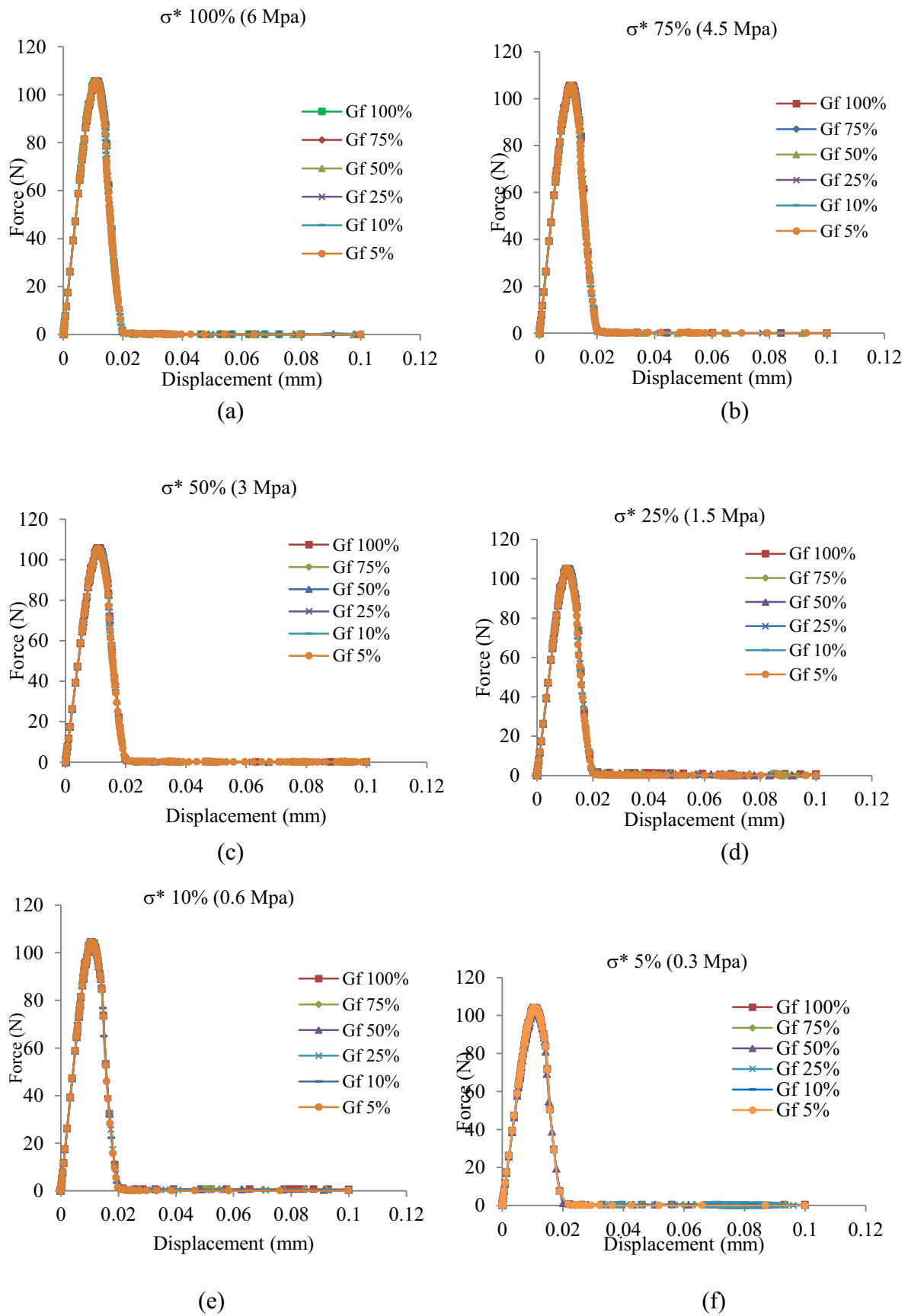


Figure 5.30: Force displacement curves with different G_f values. (a) $\sigma^* 100\%$ (b) $\sigma^* 75\%$ (c) $\sigma^* 50\%$ (d) $\sigma^* 25\%$ (e) $\sigma^* 10\%$ (f) $\sigma^* 5\%$.

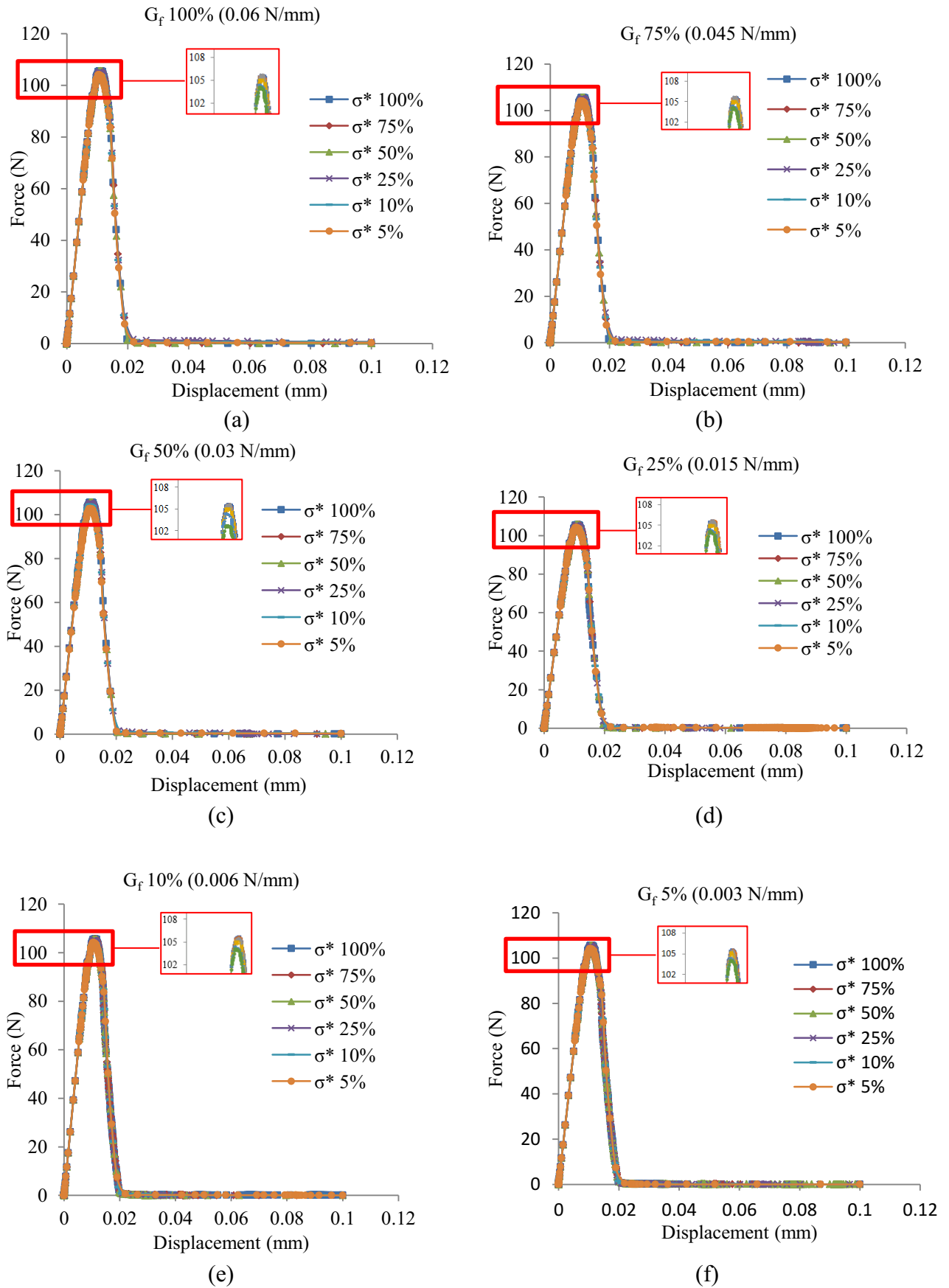


Figure 5.31: Force displacement curves with different σ^* values. (a) G_f 100% (b) G_f 75% (c) G_f 50% (d) G_f 25% (e) G_f 10% (f) G_f 5%.

B. Effects of interfacial fracture properties on the crack pattern

The effects of the interfacial fracture properties (itz) on the crack pattern for specimen with with itz ratios 100%, 75%, 50%, 25% are shown in Figure 5.32. The fracture properties of the interface (itz) is calculated as a percentage of the fracture properties of concrete matrix. The specimens with itz 100%, 75%, and 50% produced the same crack patters, as the propagating crack could break the microcapsule, which can be seen in Figure 5.32 (a), (b), and (c). When the percentage of itz, ranging from 0%–25% of the concrete matrix strength, an interfacial crack occurs and the microcapsule is debonded from the concrete matrix as illustrated in Figure 5.32 (d), (e) and (f). Figure 5.33 shows the effects of variation in fracture energy of the interfacial G_f on the crack pattern for specimen with ratios G_f 100%, 75%, 50%, 25 %, 10 % and 5% of concrete fracture energy respectively while the interfacial strength remains fixed at 6 MPa (i.e., 100 % of concrete strength). The samples with G_f 100%, 75%, 50%, and 25% produced the same crack patterns and the crack could break the microcapsule as illustrated in Figure 5.33 (a), (b), (c), and (d). When the percentage of interfacial fracture energy G_f , ranging from 0-10% of the concrete matrix fracture energy, an interfacial crack occurs and the microcapsule debonds from the concrete matrix, as illustrated in Figure 5.33 (e) and (f). An interesting fracture pattern occurred when G_f 10% as the propagating crack became initially an interfacial crack when it reaches the microcapsule shell, then suddenly breaks the capsule shell from the other side, as illustrated in Figure 5.33 (e). This means that a partial fracture crack developed when the interfacial strength is of a high value (i.e., 100 % of concrete strength) and fracture energy is of a low value (i.e., 10 % of concrete fracture energy). Figure 5.34 and Figure 5.35 shows that interfacial strengths ranging from 75% - 50% of matrix strength have the same crack pattern; the samples with interfacial G_f 100%, 75%, 50%, and 25% of matrix fracture energy produced the same crack patterns, as the crack could break the microcapsule as illustrated in Figure 5.34 and Figure 5.35 (a), (b), (c), and (d). When the percentage of G_f ranges from 0%–10% of the concrete matrix fracture energy, an interfacial crack occurs and the microcapsule debonds from the concrete matrix, as illustrated in Figure 5.34 and Figure 5.35 (e) and (f). Figure 5.36, Figure 5.37, and Figure 5.38 show that interfacial strengths ranging from 5% - 25% of matrix strength have the same crack patterns as the microcapsule debonds from the concrete matrix. An interesting fracture pattern occurred when the interfacial σ^* 10% and interfacial G_f 100% of the concrete matrix, because the propagating crack could not debond the microcapsule completely, as shown in Figure 5.36 (a). That means a partially debonded crack developed when the interfacial strength is 25 % of concrete strength and fracture energy is high value (same as concrete matrix).

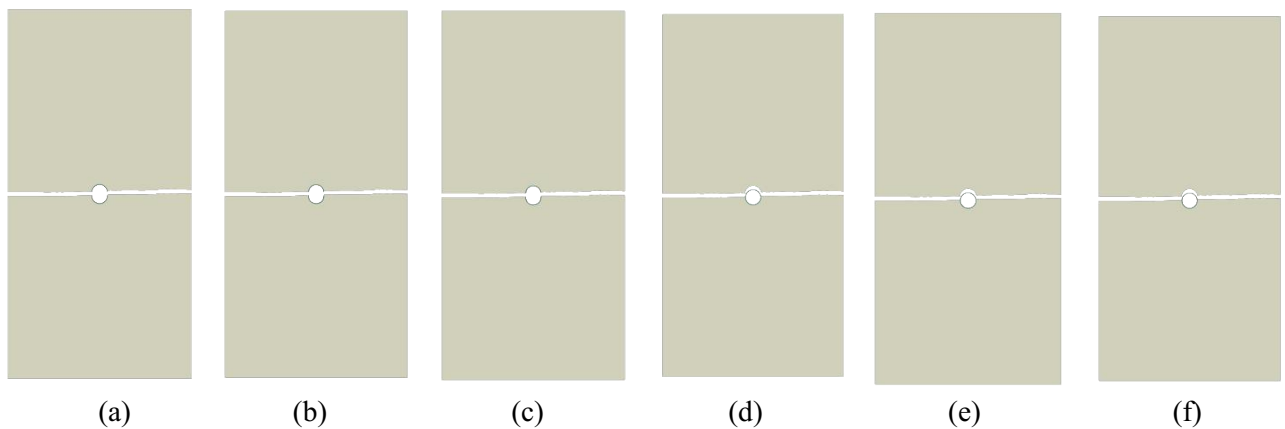
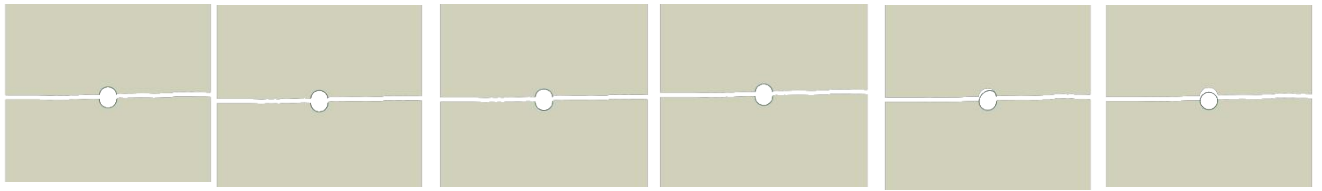
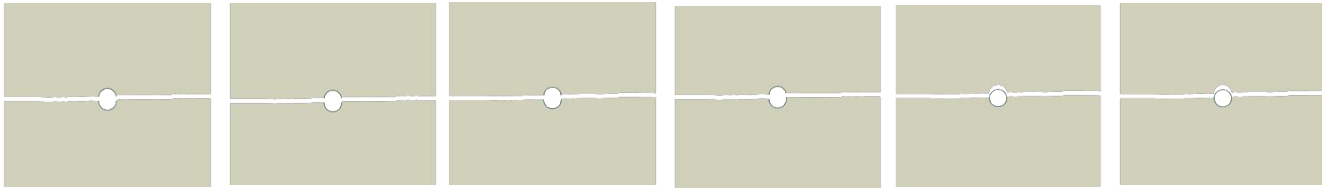


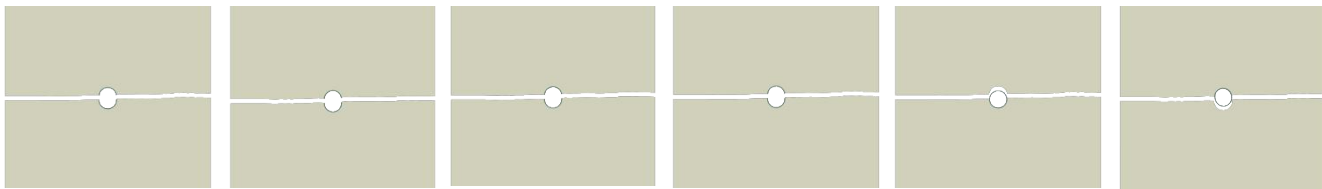
Figure 5.32: Crack pattern specimens with different itz values. (a) itz 100% (b) itz 75% (c) itz 50% (d) itz 25% (e) itz 10% (f) itz 5%.



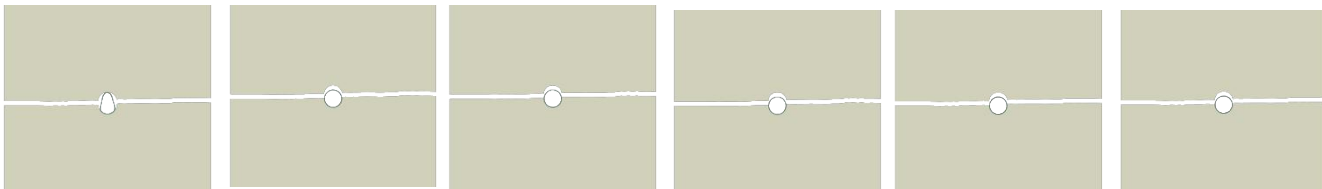
(a) (b) (c) (d) (e) (f)
 Figure 5.33: Crack pattern of σ^* 100% specimen (6 Mpa) with different G_f ratios. (a) G_f 100% (b) G_f 75% (c) G_f 50% (d) G_f 25% (e) G_f 10% (f) G_f 5%.



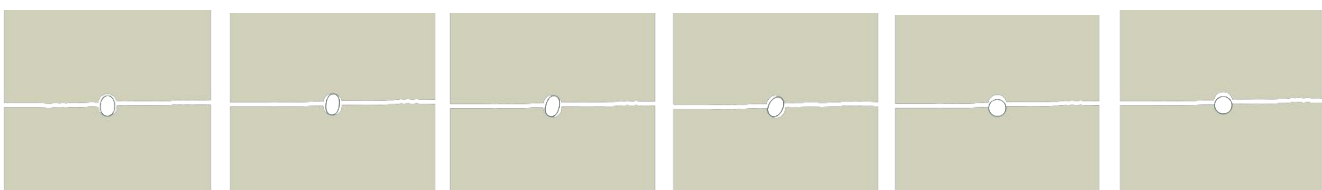
(a) (b) (c) (d) (e) (f)
 Figure 5.34: Crack pattern of σ^* 75% specimen (4.5 Mpa) with different G_f ratios. (a) G_f 100% (b) G_f 75% (c) G_f 50% (d) G_f 25% (e) G_f 10% (f) G_f 5%.



(a) (b) (c) (d) (e) (f)
 Figure 5.35: Crack pattern of σ^* 50% specimen (3 Mpa) with different G_f ratios. (a) G_f 100% (b) G_f 75% (c) G_f 50% (d) G_f 25% (e) G_f 10% (f) G_f 5%.



(a) (b) (c) (d) (e) (f)
 Figure 5.36: Crack pattern of σ^* 25% specimen (1.5 Mpa) with different G_f ratios. (a) G_f 100% (b) G_f 75% (c) G_f 50% (d) G_f 25% (e) G_f 10% (f) G_f 5%.



(a) (b) (c) (d) (e) (f)
 Figure 5.37: Crack pattern of σ^* 10% specimen (0.6 Mpa) with different G_f ratios. (a) G_f 100% (b) G_f 75% (c) G_f 50% (d) G_f 25% (e) G_f 10% (f) G_f 5%.



(a) (b) (c) (d) (e) (f)
 Figure 5.38: Crack pattern of σ^* 5% specimen (0.3 Mpa) with different G_f ratios. (a) G_f 100% (b) G_f 75% (c) G_f 50% (d) G_f 25% (e) G_f 10% (f) G_f 5%.

5.3.2 Effects of Microcapsule Size and Interfacial Fracture Properties: Verification Study

5.3.2.1 Description of the model

2D precracked concrete specimens with one microcapsule loaded under uniaxial tension. The dimensions of the specimens are 50 mm x 25 mm and the diameter of the microcapsule is 2 mm with four values of core-shell thickness ratio; 1:1, 5:1, 10:1, and 15:1. The microcapsule with the largest core-shell ratio (15:1) has the smallest shell thickness and vice versa. The precrack length is 4 mm is placed at the middle of the specimens' heights. The overall geometry dimensions of this specimen with the boundary conditions are shown in Figure 5.39. Uniform displacement 0.1 mm was applied on the top surface of the specimens. The simulation was done in Abaqus/Static and the samples are meshed with Quadrilateral elements (Q4) assuming plane stress conditions. The material properties listed in Table 5.4 are characterized by [71, 73, 79, 80, 83, 84]. Their parameters are then represented by Young's modulus (E), Poisson's ratio (ν), maximum tensile strength (σ^*), and fracture energy (G_f). For the cohesive surface representing the interaction between the microcapsule and the concrete matrix, the normal and shear fracture properties are assumed to be equal due to the lack of experimental data available in the literature.

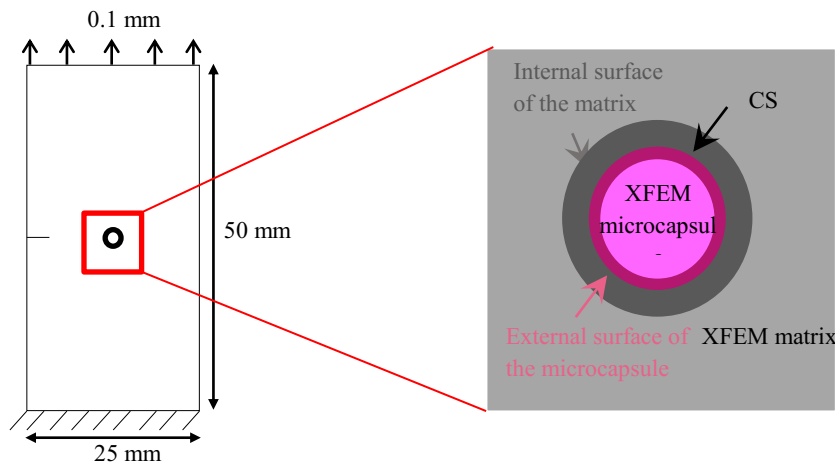


Figure 5.39: Specimens geometry dimensions and modeling techniques.

Table 5.4: The material properties.

Material	E (MPa)	ν	σ^* (MPa)	G_f (N/mm)
Concrete	25000	0.2	6	0.06
Capsule	3600	0.3	10	0.1
Interface	-	-	Varies	Varies

5.3.2.2 Study of the mesh size

In order to establish the degree of mesh refinement required to obtain reliable results, several preliminary calculations using a microcapsule with is 2 mm diameter and shell thickness of 0.1 mm as an average size for the four values of the core-shell thickness ratio, have been done. Three meshes with different discretization are conducted as shown in Figure 3. The coarse mesh has 5219 elements, consisting of 5103 elements for the matrix and 116 elements for the microcapsule with 2 elements through its thickness. The medium mesh has 16435 elements consisting of 16078 elements for the matrix and 357 elements for the microcapsule with 3 elements through its thickness. The fine mesh has 32217 elements consisting of 31741 elements for the matrix and 476 elements for the microcapsule with 4 elements through its thickness. Figure 4 shows the damage dissipation energy (fracture energy) for each mesh discretization. The damage dissipation energy curves for the medium mesh and the fine mesh density are very close to each other. Therefore, the medium mesh discretization is employed for simulations and presenting the results.

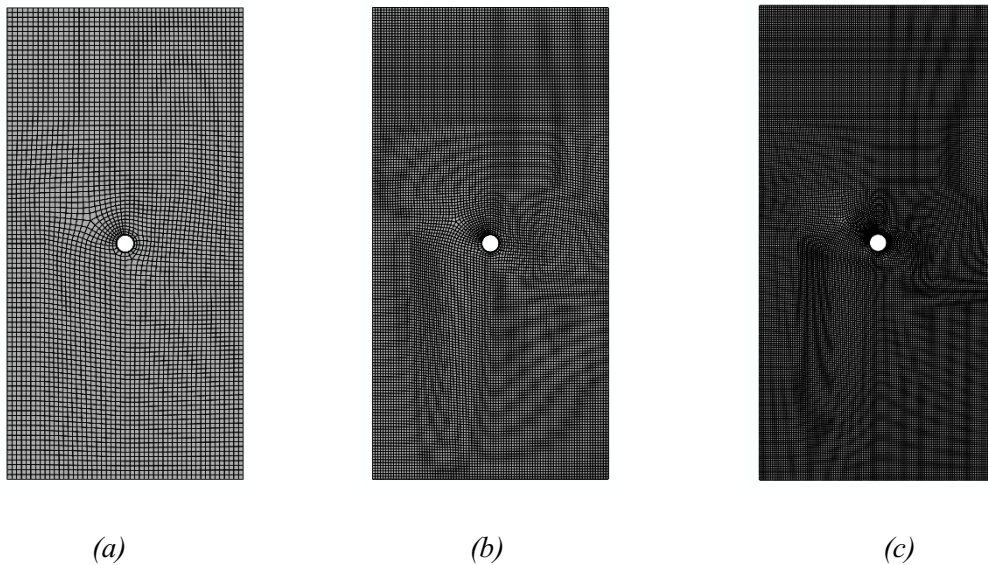


Figure 5.40: Three meshes with different discretization (a) Coarse mesh (5219 elements) (b) Medium mesh (16435 elements) (c) Fine mesh (32217 elements).

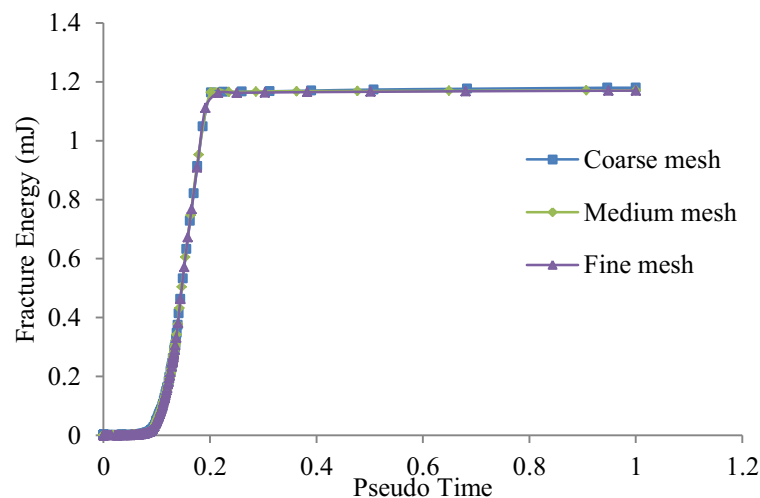


Figure 5.41: Damage dissipation energy from different mesh discretization.

5.3.2.3 Parametric studies

Parametric studies of different interfacial fracture properties are performed to study the effects of the interfacial transition zone (itz) between the microcapsule shell and the concrete matrix on the load carrying and the crack patterns with four different core-shell thickness ratios as shown in Figure 5.42. The cohesive surface between the microcapsule shell and the concrete matrix is defined by only two parameters which represent the interfacial fracture properties; the maximum interfacial tensile strength σ^* , which is known as the bonding strength as well and the interfacial fracture energy G_f . In order to investigate the effects of interfacial strength and fracture energy, parametric studies of five different material inputs for σ^* and G_f were carried out. These two parameters for the interfacial transition zone (itz) are varied relative to the properties of the concrete for each simulation while the other parameters were fixed; i.e. they range from 10% ($\sigma^* = 0.6$ Mpa, $G_f = 0.006$ N/mm) to 100% ($\sigma^* = 6$ Mpa, $G_f = 0.06$ N/mm).

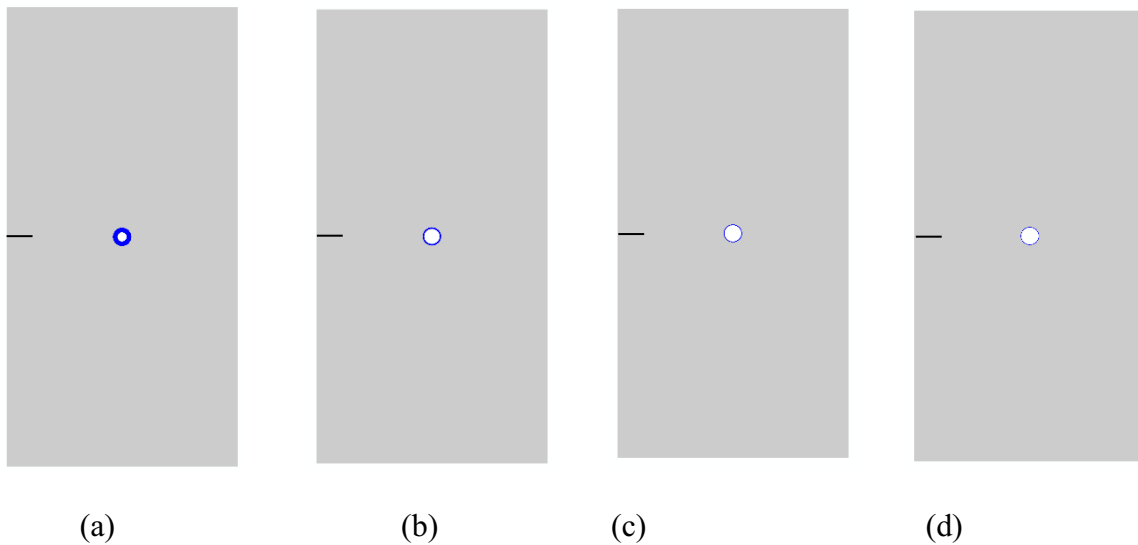


Figure 5.42: Samples with different microcapsule core shell thickness ratios, (a) Ratio 1:1 (b) Ratio 5:1 (c) Ratio 10:1 (d) Ratio 15:1.

5.3.2.4 Results and discussion

A. Effects of interfacial fracture properties and the microcapsule size on the load carrying capacity

The effects of interfacial fracture properties (itz) for the specimens with core-shell thickness ratios 1:1, 5:1, 10:1, and 15:1 on load carrying capacity are represented by variation of itz from 10% of the concrete fracture properties ($\sigma^* = 0.6$ Mpa, $G_f = 0.006$ N/mm) to 100%; in the same manner the concrete fracture properties ($\sigma^* = 6$ Mpa, $G_f = 0.06$ N/mm) are demonstrated in Figure 5.43-Figure 5.46. It is apparent that interfacial cohesive characteristics have a significant impact on the specimen's load carrying capacity. Figure 5.43 shows the effects of the interfacial fracture properties itz on the load carrying capacity of the specimen with the microcapsule core-shell thickness ratio 1:1. The maximum load of the specimen increased from 103.5 N for itz = 10% to 106.7 N for itz = 100%. Consequently, it is clear that

the interfacial cohesive properties itz have a significant role for governing the load carrying capacity of the specimen. The same phenomenon also can be found in Figure 5.44, Figure 5.45, and Figure 5.46 for the microcapsule with ratios 5:1, 10:1, and 15:1, respectively. It is clear that when the interfacial cohesive fracture properties have the same values of the concrete matrix, the higher maximum load carrying capacity will be achieved. As a result, the higher the itz, the higher the load carrying capacity and vice versa.

In order to show the accuracy of this proposed model a comparison with the zero thickness cohesive elements approach (CE) which had been used on a previous study [73] has been performed. The dotted curves show the effects of the same range of the fracture properties of the interface (itz) on the load carrying capacity using the cohesive elements (CE). For sake of clarity, only the lower and upper limits for that range have been plotted in dotted lines. It has to be noted in that previous study, the healing agent, which is liquid, is modeled as solid elements although the modeling focussed only on the fracture of the microcapsule without studying the releasing of the healing agent. Additionally, the drawbacks of that approach, such as artificial compliance which are mentioned in [75] led to overestimated load carrying capacity of the model. Regarding the healing agent aspect, this proposed model is restricted to model the fracture and debonding of the microcapsule, and therefore it is assumed empty.

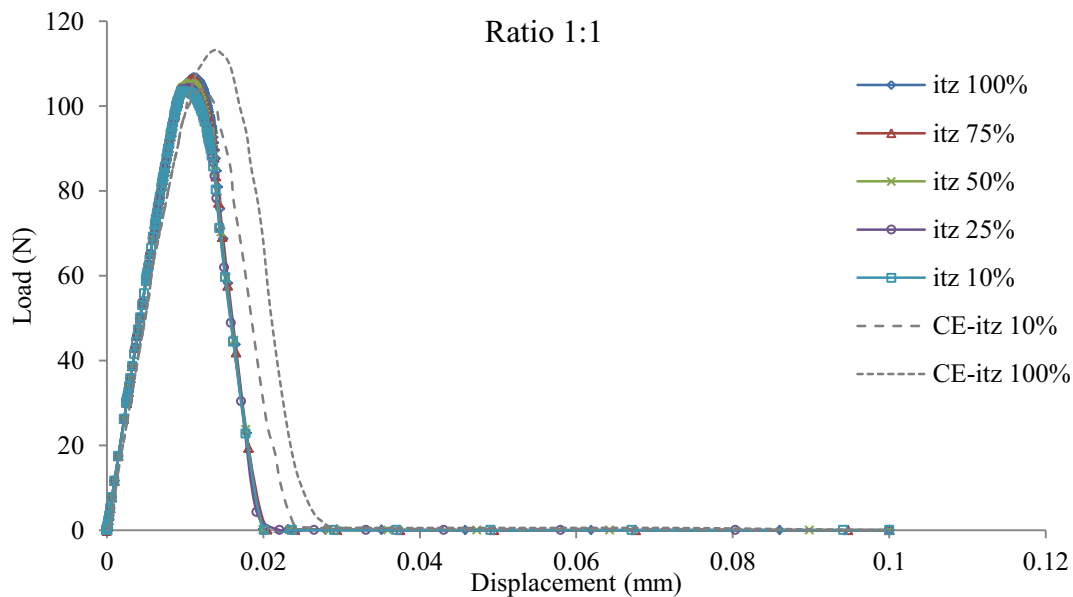


Figure 5.43: Load displacement curves for microcapsule core-shell ratio 1:1 with different itz values.

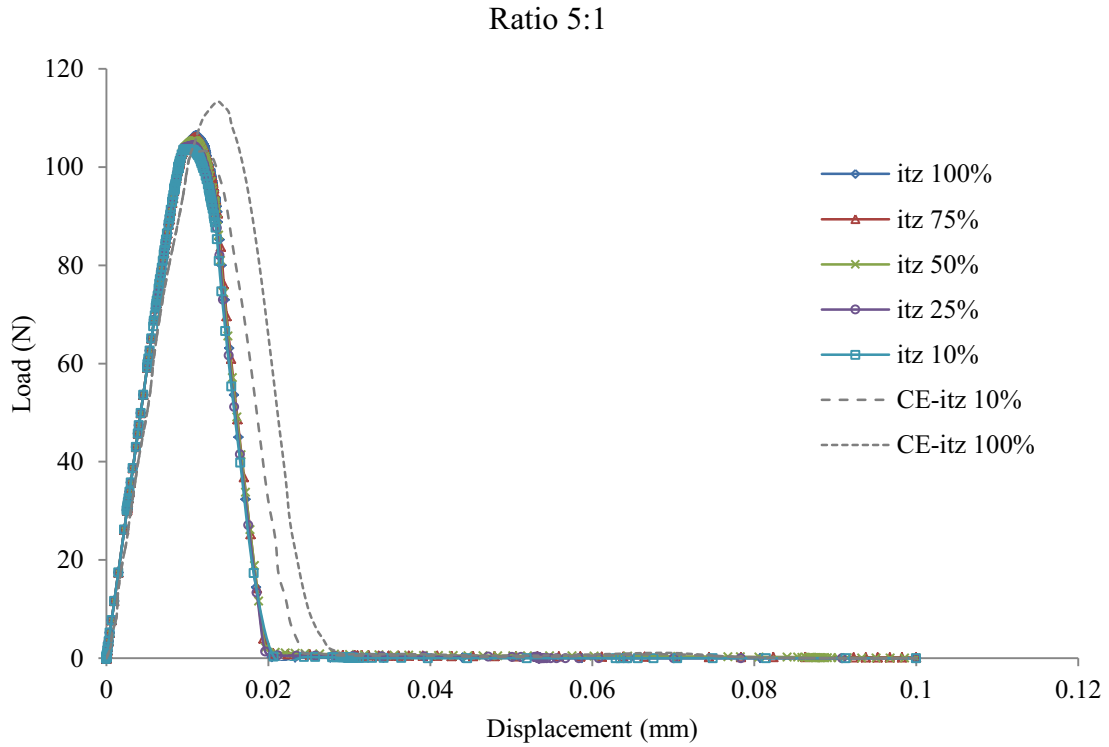


Figure 5.44: Load displacement curves for microcapsule core-shell ratio 5:1 with different itz values.

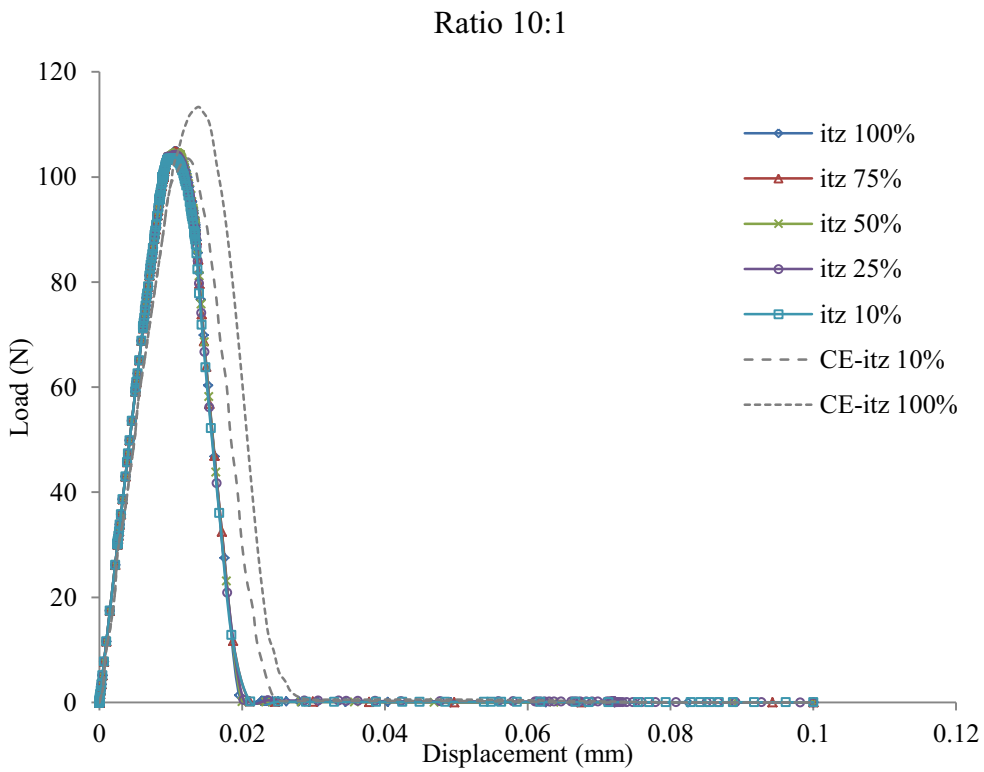


Figure 5.45: Load displacement curves for microcapsule core-shell ratio 10:1 with different itz values.

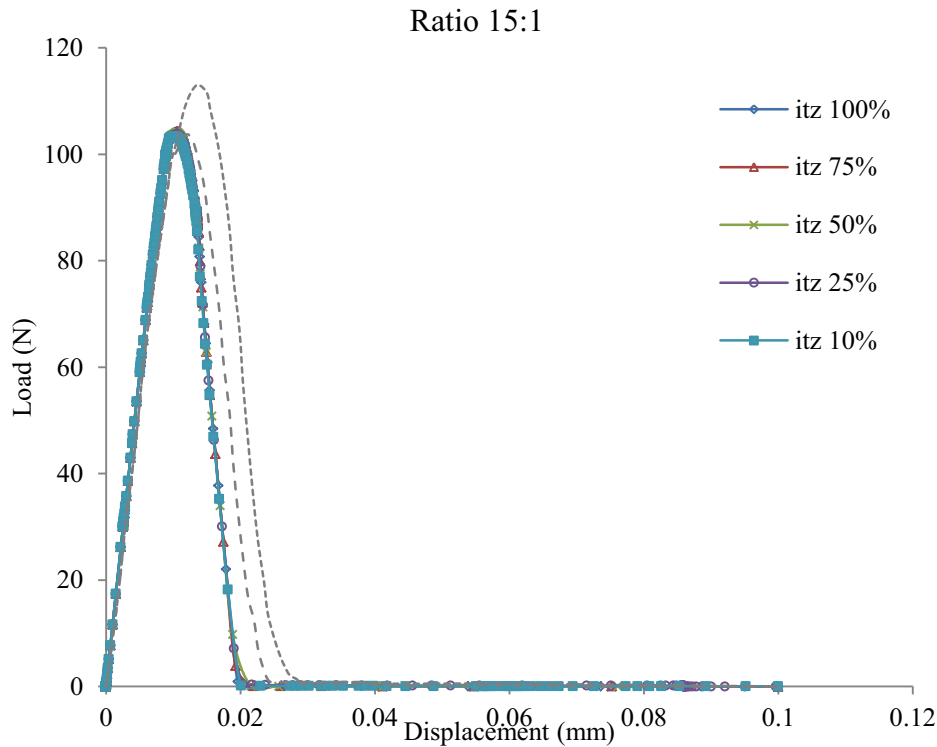


Figure 5.46: Load displacement curves for microcapsule core-shell ratio 15:1 with different itz values.

B. Effects of interfacial fracture properties and the microcapsule size on the maximum carrying load

The effects of the microcapsule size, which is defined by the core-shell thickness ratio, on the maximum carrying load for the four samples with different interfacial fracture properties (itz) are shown in Figure 5.47. It is shown that the lower core-shell thickness ratio (larger shell thickness) of the microcapsule, the higher the maximum carrying load of the sample. On the other hand, the higher percentage of itz increases the maximum load of the sample that it can withstand.

Also, to show the accuracy of this proposed model for studying the relationship between the maximum carrying load and the itz ratio of interfacial fracture properties for different microcapsule core-shell thickness ratios, another comparison will be made. This comparison with the zero thickness cohesive elements approach (CE) which had been used on a previous study [73] has been performed. The dotted curve shows the effects of the same range of microcapsule core-shell thickness ratios which were almost identical for all different four ratios 1:1, 5:1, 10:1, and 15:1 in that study. It has been mentioned in that previous study that there is no effect from the core-shell thickness ratio of microcapsule on the load carrying capacity of the specimen. On the contrary, our proposed model has shown clearly that the core-shell thickness ratio of the microcapsule has a significant effect on the load carrying capacity as the lower core-shell thickness ratio of the microcapsule (larger shell thickness) leads to the higher load carrying capacity of the sample which is logic. So, the proposed model shows more accuracy for modeling the fracture of encapsulation-based self-healing concrete compared to the zero thickness cohesive elements approach (CE) and confirms its drawbacks, which were reported in [75].

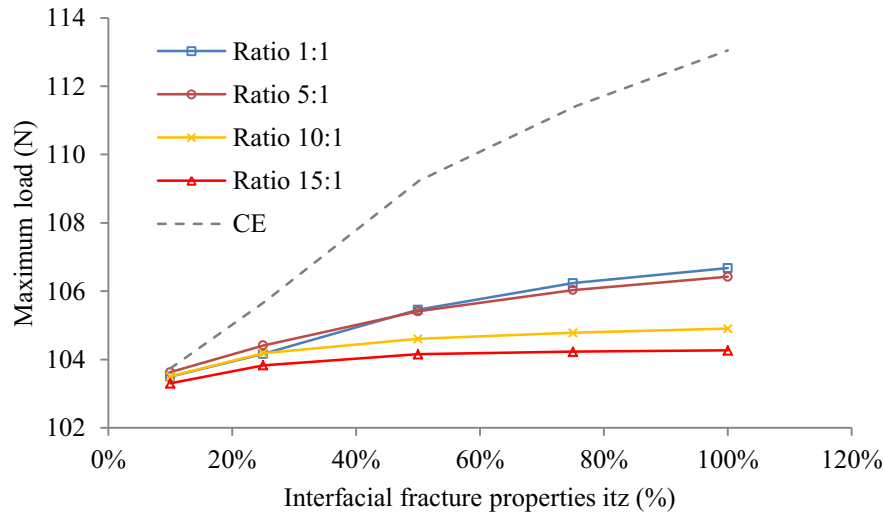


Figure 5.47: Effects of itz ratios to the maximum load with different microcapsule core-shell ratios.

C. Effects of interfacial fracture properties and the microcapsule size on the crack pattern

The effects of the interfacial fracture properties (itz) for specimens with core-shell thickness ratios 1:1, 5:1, 10:1, and 15:1 on the crack pattern are shown in Figure 5.48, Figure 5.49, Figure 5.50, Figure 5.51 respectively. The effects of the interfacial fracture properties are represented by variation of itz from 10% of the concrete fracture properties ($\sigma^* = 0.6$ Mpa, $G_f = 0.006$ N/mm) to 100%; same as the concrete fracture properties ($\sigma^* = 6$ Mpa, $G_f = 0.06$ N/mm). Figure 5.48 shows that the specimens with core-shell thickness ratio 1:1 (the largest shell thickness) produced the same crack patterns as the microcapsule is debonded from the concrete matrix regardless of the ratio of the interfacial fracture properties (itz). The propagating crack couldn't break the microcapsule shell even when the interfacial fracture properties have the same values of the concrete matrix, see Figure 5.48 (a)-(e) as an interfacial crack occurs regardless the itz ratio. When the specimens have a core-shell thickness ratio of 5:1 and a percentage of itz of the fracture properties of the concrete matrix ranging from 0%–50%, an interfacial crack occurs and the microcapsule is debonded from the concrete matrix, as shown in Figure 5.49 (a)-(c). When the itz ratio is 75% the propagating crack became an interfacial crack when it reached the microcapsule shell and breaks it from the other side, as illustrated in Figure 5.49(d). That means a partial fracture crack is developed when the microcapsule core-shell thickness ratio is 5:1 and the ratio of the interfacial fracture properties between the microcapsule and the concrete matrix (itz) is 75%. When the itz ratio is 100% (same as the concrete) the propagating crack could break the microcapsule as shown in Figure 5.49(e). The crack pattern for the specimens with core-shell thickness ratio 10:1 and 15:1 are similar, and it is clear that when interfacial fracture properties (itz) range from 0-25% an interfacial crack occurs, as shown in Figure 5.50(a) & (b) and Figure 5.51(a) & (b). The microcapsule is debonded from the concrete matrix as the propagating crack couldn't break the microcapsule shell. On the contrary, when the fracture properties of the interface (itz) ranging from 50-100% the propagating crack could break the microcapsule as shown in Figure 5.50(c)-(e) and Figure 5.51(c)-(e). This shows that the good match between the

interfacial fracture properties and the proper core-shell thickness ratio leads to the fracturing of the microcapsule. That will allow the release of healing agents, then solidification process will start to heal the cracks inside the concrete matrix.

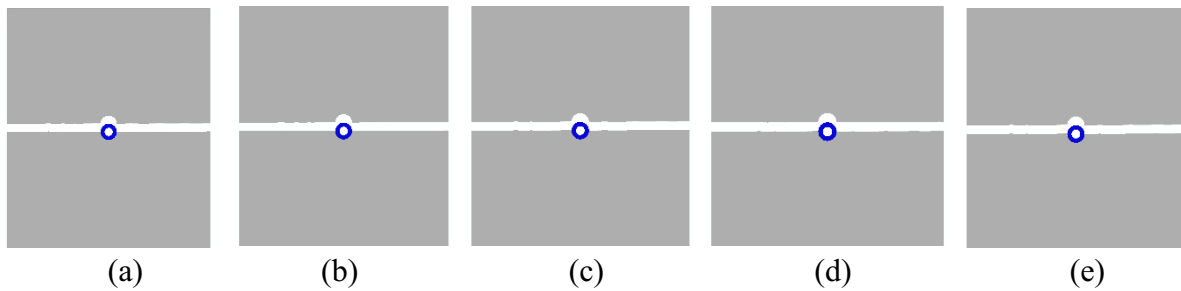


Figure 5.48: Crack pattern of microcapsule ratio 1:1 with different itz ratios. (a) itz 10% (b) itz 25% (c) itz 50% (d) itz 75% (e) itz 100%.

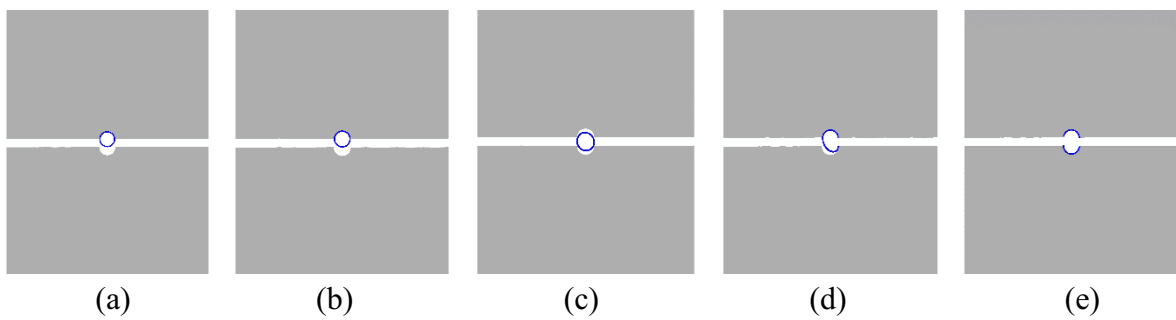


Figure 5.49: Crack pattern of microcapsule ratio 5:1 with different itz ratios. (a) itz 10% (b) itz 25% (c) itz 50% (d) itz 75% (e) itz 100%.

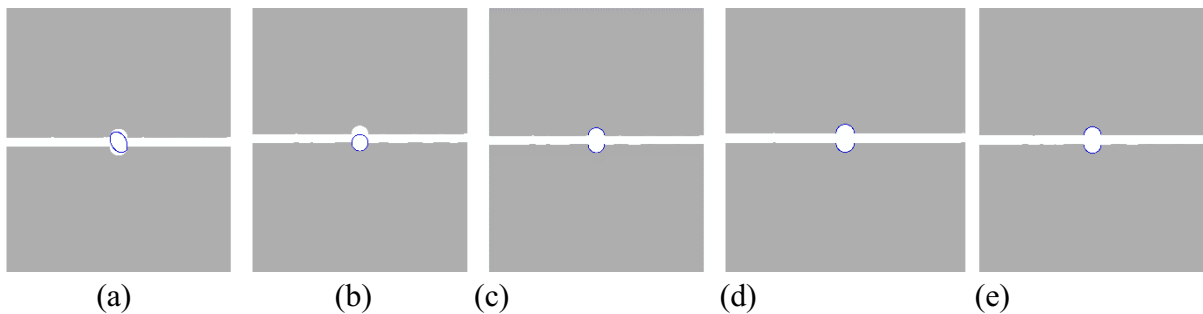


Figure 5.50: Crack pattern of microcapsule ratio 10:1 with different itz ratios. (a) itz 10% (b) itz 25% (c) itz 50% (d) itz 75% (e) itz 100%.

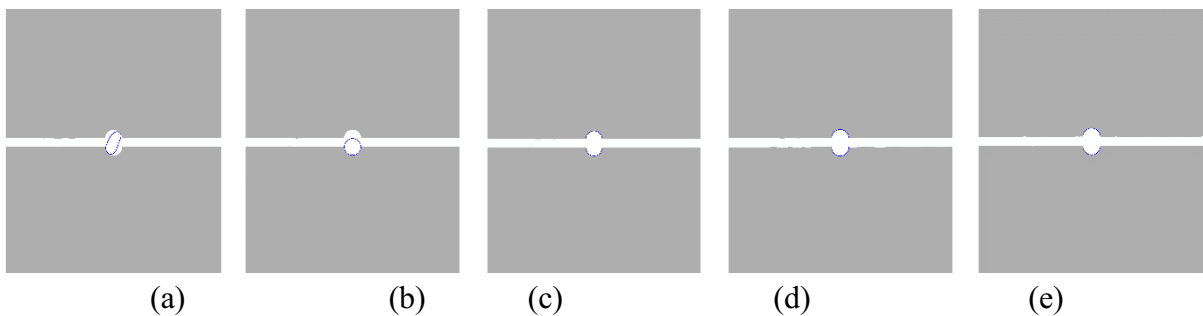


Figure 5.51: Crack pattern of microcapsule ratio 15:1 with different itz ratios. (a) itz 10% (b) itz 25% (c) itz 50% (d) itz 75% (e) itz 100%.

It is worth mentioning that this proposed model shows high accuracy compared to the zero thickness cohesive elements approach (CE) which have been used on a previous study [73]. As in that previous study (CE) the specimen with core-shell thickness ratio 5:1 produced the similar crack pattern which produced from the specimen with core-shell thickness ratio 1:1 as the microcapsule is debonded from the concrete matrix regardless of the value of the interfacial fracture properties (itz). Also, the crack pattern will be similar for the specimen with core-shell thickness ratio 10:1 and 15:1 when the interfacial fracture properties (itz) range from 0-75%, as an interfacial crack occurs and the microcapsule was debonded from the concrete matrix because the propagating crack couldn't break the microcapsule shell. But only the propagating crack could break the microcapsule shell when the itz percentage is 100% (same as the concrete) for the specimen with core-shell thickness ratio 10:1 and 15:1. However, it doesn't appear logical that the microcapsule fractures only when the interfacial fracture properties have the same value for concrete matrix regardless the microcapsule core-shell thickness ratio, especially in the case of the microcapsule with the largest core-shell ratio (15:1) which has the thinnest thickness of shell. So, the proposed model shows more accuracy for modeling the fracture of encapsulation-based self-healing concrete, compared to the zero thickness cohesive elements approach (CE) and confirms its disadvantages such as artificial compliance and mesh dependency, which is reported in [75].

5.4 Effects of Microcapsule Clustering

In this section, the effects of microcapsule clustering on the fractured microcapsule are studied computationally. The clustering effects of microcapsules could happen due to the random distribution of the microcapsules during the mixing process of the concrete. The modeling focused on studying the effects of the effective contact surface between the microcapsule and the concrete matrix, on the load carrying capacity and the probability of fracture or debonding of the microcapsule from the concrete matrix.

5.4.1 Description of the model

2D precracked concrete specimens with one microcapsule loaded under uniaxial tension. The dimensions of the specimens are 50 mm x 25 mm and the diameter of the microcapsule is 2 mm with a shell thickness 0.1 mm. The precrack length is 4 mm and is placed at the middle of the specimens' heights. The overall geometry dimensions of this sample with the boundary conditions are shown in Figure 5.52. Uniform displacement 0.1 mm was applied on the top surface of the specimens. The simulation was done in Abaqus/Static and the samples are meshed with Quadrilateral elements (Q4), assuming plane stress conditions. The material properties listed in Table 5.5 are characterized by [71, 73, 79, 80]. Their parameters are then represented by Young's modulus (E), Poisson's ratio (ν), maximum tensile strength (σ^*), and fracture energy (G_f). For the cohesive surface representing the interaction between the microcapsule and the concrete matrix, the normal and shear fracture properties are assumed to be equal due to the lack of experimental data available in the literature.

There is no need to study the mesh refinement in this section as the same dimensions and boundary conditions from the previous modeling in section 5.3.2 have been used here. The mesh discretization has 16734 elements consisting of 15782 elements for the matrix and 952 elements for the microcapsule with 4 elements through its thickness, as shown in Figure 5.53.

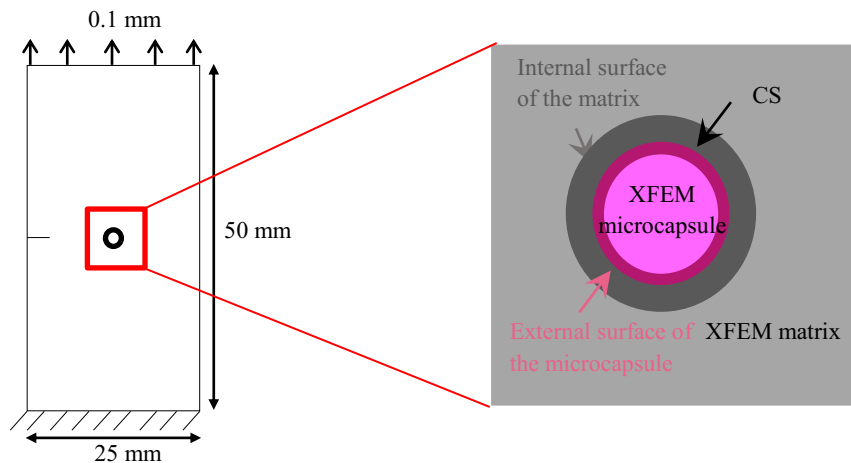


Figure 5.52: Specimens geometry dimensions and modeling techniques.

Table 5.5: The material properties.

Material	E (MPa)	ν	σ^* (MPa)	G_f (N/mm)
Concrete	25000	0.2	6	0.06
Capsule	3600	0.3	10	0.1
Interface	-	-	6	0.06

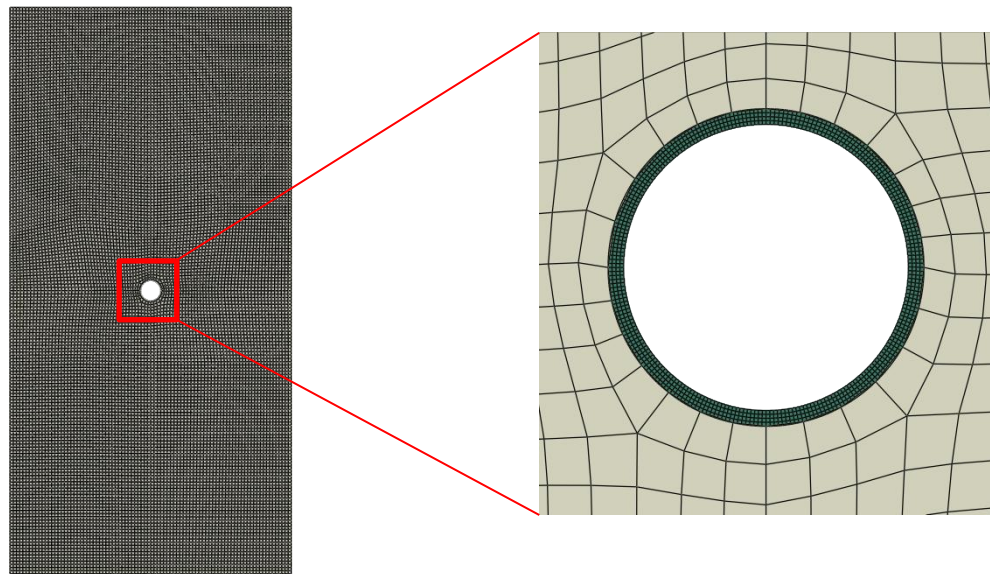
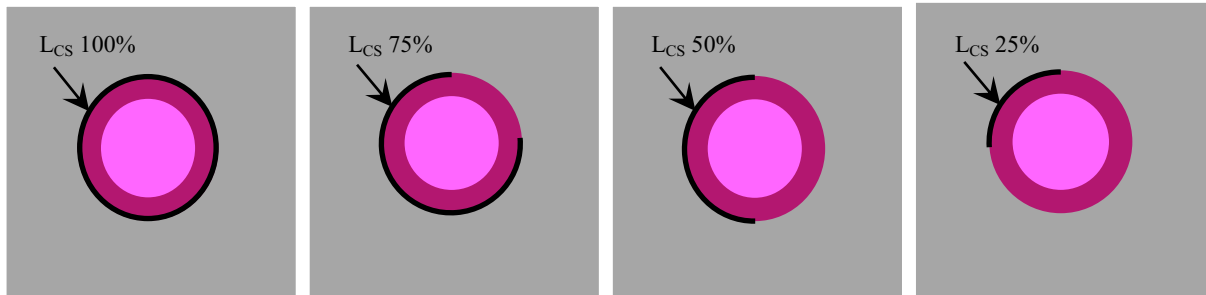


Figure 5.53: The meshing of the specimens.

5.4.2 Parametric studies

The capsular clustering could happen due to the random distribution of the microcapsules during the mixing process of the concrete. The microcapsules clustering could happen in various assemblies, starting from simple degrees of clustering with only two microcapsules in contact and so on. To model different degrees of microcapsule clustering, a lot of complications will occur, especially for mesh discretization in addition to the higher computational cost. In order to avoid these complications, a simple proposed procedure in 2D is designed with a singular microcapsule and changing the circumference contact length between the microcapsule and the concrete. Parametric studies of different contact circumference surface lengths between the microcapsule and the concrete are performed to study the effects of capsular circumferential contact length (L_{cs}) on the load carrying and the crack patterns. The material parameters values in Table 5.5 are assigned to each part. Only one parameter (L_{cs}), which represents the contact length between the concrete matrix and the microcapsule is varied relative to the microcapsule circumference length while other parameters were fixed. The four capsular circumferential contact length ratios (L_{cs}) range from 25% ($L_{cs} = 1.57$ mm) to 100% ($L_{cs} = 6.28$ mm), see Figure 5.54.



(a)

(b)

(c)

(d)

Figure 5.54: Specimens with different capsular circumferential contact length ratios L_{cs} ratios

(a) L_{cs} 100% ($L_{cs} = 6.28$ mm) (b) L_{cs} 75% ($L_{cs} = 4.71$ mm) (c) L_{cs} 50% ($L_{cs} = 3.14$ mm)

(d) L_{cs} 25% ($L_{cs} = 1.57$ mm).

5.4.3 Results and discussion

A. Effects of the capsular clustering on the load carrying capacity

The effects of the capsular clustering on the load carrying capacity for the specimens represented by different capsular circumferential contact lengths (L_{cs}) ratios are shown in Figure 5.55. It shows the capsular circumferential contact lengths ranging from L_{cs} 100% of the microcapsule circumference; i.e. same as microcapsule circumference ($L_{cs} = 6.28$ mm) to L_{cs} 25% of the microcapsule circumference ($L_{cs} = 1.57$ mm). In addition to zero contact case, which means there is no contact between the microcapsule and concrete. In this case, the model could be considered as a concrete plate with a hole. The maximum load carried by the specimen decreased from 104.7 N for $L_{cs} = 100\%$ to 103N for $L_{cs} = 25\%$ and 102.7 N for $L_{cs} = 0\%$. That means when the contact length of the interface between the microcapsule and the concrete is equal to the microcapsule circumference, the specimen will reach the maximum carrying load.

The relationship between the maximum carrying load and the different L_{cs} ratios of the capsular circumferential contact length can be observed from Figure 5.56. It is shown clearly that the higher percentage of L_{cs} increases the maximum load that the specimen can withstand. So, the higher the L_{cs} ratio, the greater the load carrying capacity of the specimen and vice versa.

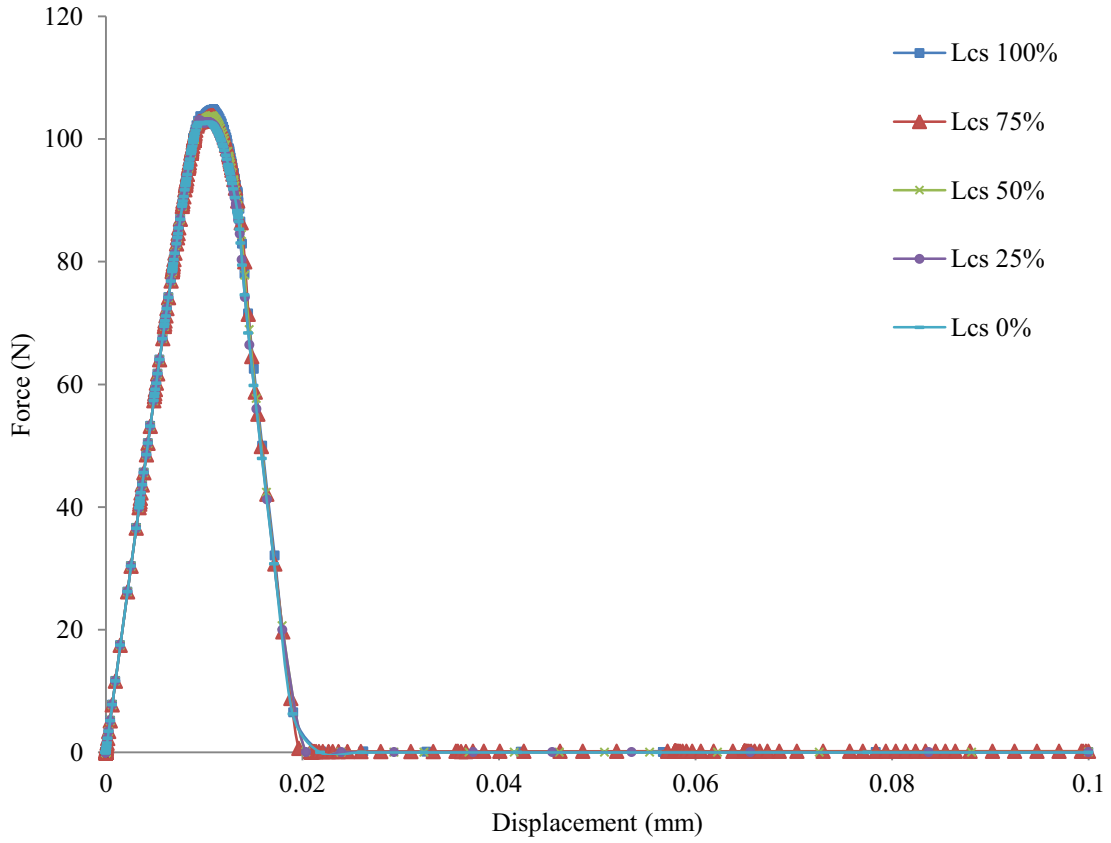


Figure 5.55: Load displacement curves for specimens with different L_{cs} ratios.

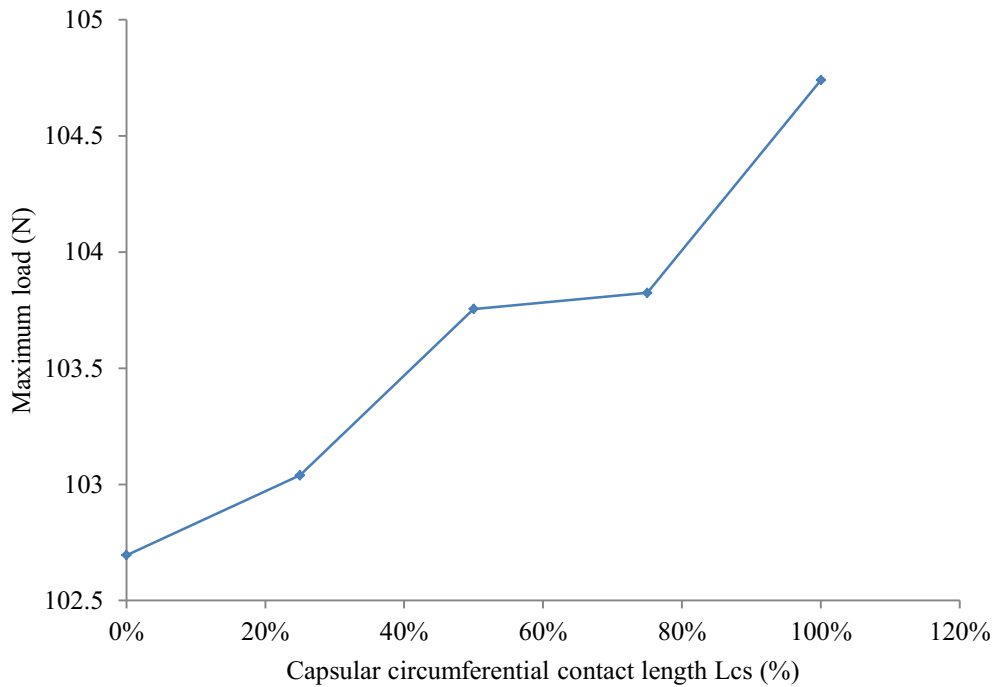


Figure 5.56: Effects of the L_{cs} ratio on the maximum load of the specimens.

B. Effects of the capsular clustering on the crack pattern

The effects of the capsular clustering for specimens represented by different capsular circumferential contact lengths (L_{cs}) ratios 100%, 75%, 50%, 25%, and 0% on the crack pattern are shown in Figure 5.57 (a), (b), (c), (d), and (e) respectively. It is clear that when the capsular circumferential contact length (L_{cs}) ratio ranges from 0-25% an interfacial crack occurs, as shown in Figure 5.57 (d) & (e). The microcapsule is debonded from the concrete matrix, as the propagating crack couldn't break the microcapsule shell. When the capsular circumferential contact length ratio is L_{cs} 50%, the propagating crack breaks the microcapsule shell from only one side and it debonds from the other side, due to an interfacial crack being generated, as illustrated in Figure 5.57(c). When the capsular circumferential contact length ratio is L_{cs} 75% an interesting crack pattern is generated, as the propagating crack broke the microcapsule shell completely from one side and partial fractured and debonded the microcapsule from the other side, as illustrated in Figure 5.57(b). The microcapsule is completely fractured when the capsular circumferential contact length ratio is L_{cs} 100%, as illustrated in Figure 5.57(a). That shows clearly that the capsular clustering which is represented by the capsular circumferential contact length ratio has a significant role for determining whether the microcapsule will fracture or debond from the concrete matrix. Consequently, the higher the L_{cs} , the higher probability of the microcapsule being fractured and vice versa.

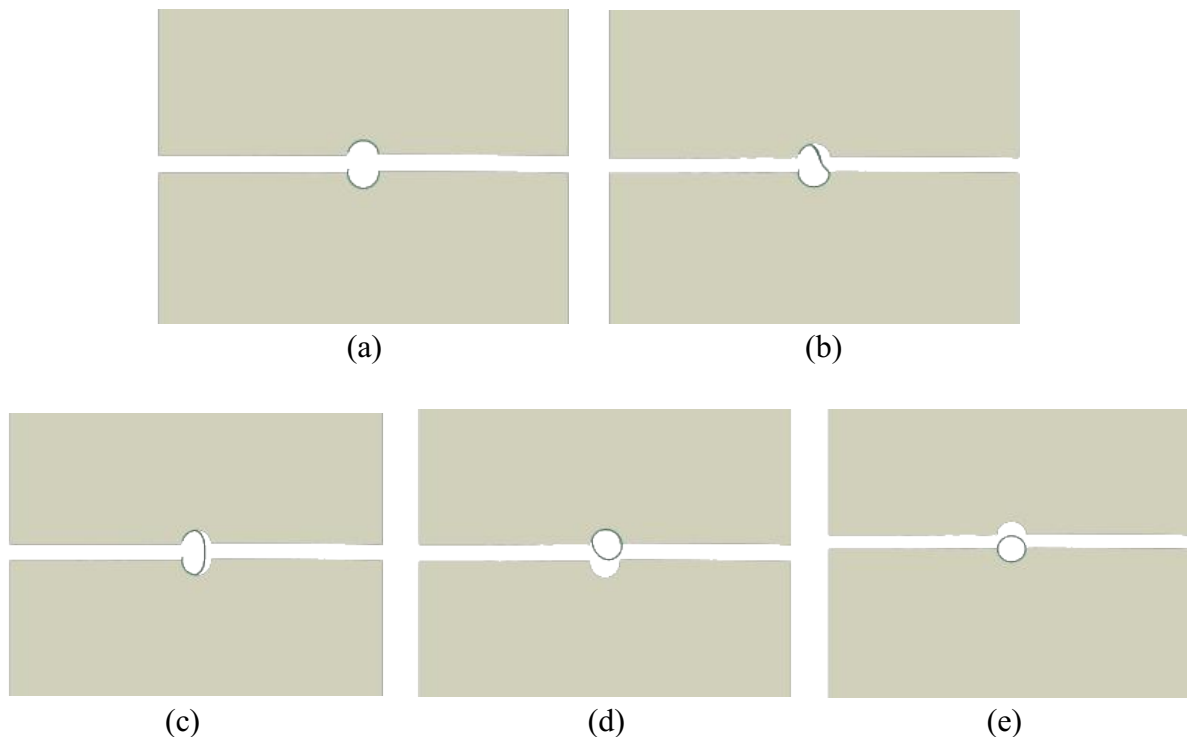


Figure 5.57: Crack pattern of specimens with different L_{cs} ratios. (a) L_{cs} 100% (b) L_{cs} 75% (c) L_{cs} 50% (d) L_{cs} 25% (e) L_{cs} 0%.

5.5 3D Microcapsule Fracture

In this section, 3D computational simulations are performed to study the possibilities of fracture and debonding of the microcapsule from the concrete matrix. The modeling focused on studying the effects of the effective contact surface between the microcapsule and the concrete matrix, on the load carrying capacity, and the probability of fracture or debonding of the microcapsule from the concrete matrix. In addition, the obtained results are compared with the results obtained from 2D simulations in previous sections in order to study the difference in results obtained from both simulations and to estimate the accuracy difference. This study will validate the 2D computational simulation and estimate the accuracy difference ratio between 2D and 3D simulations, which allows practical engineers to get much more reliable results based only on 2D simulations that can be built easily and not as computationally expensive as 3D simulations. In brief, such study aims to allow the practical engineers to get the most use of 2D simulations for encapsulated self-healing concrete.

5.5.1 Description of the model

3D precracked concrete specimens with one microcapsule loaded under uniaxial tension. The dimensions of the specimens are 50 mm x 25 x 5 mm and the diameter of the microcapsule is 2 mm with a shell thickness 0.1 mm. The precrack length is 4 mm, and is placed at the middle of the specimens' heights. The overall geometry dimensions of this sample with the boundary conditions are shown in Figure 5.58. Uniform displacement 0.1 mm was applied on the top surface of the specimens. The simulation was done in Abaqus/Static and the samples are meshed with Tetrahedral elements (Tet4) assuming plane stress conditions. The material properties listed in Table 5.6 are characterized by [71, 73, 79, 80]. Their parameters are then represented by Young's modulus (E), Poisson's ratio (ν), maximum tensile strength (σ^*), and fracture energy (G_f). For the cohesive surface representing the interaction between the microcapsule and the concrete matrix, the normal and shear fracture properties are assumed to be equal due to the lack of experimental data available in the literature.

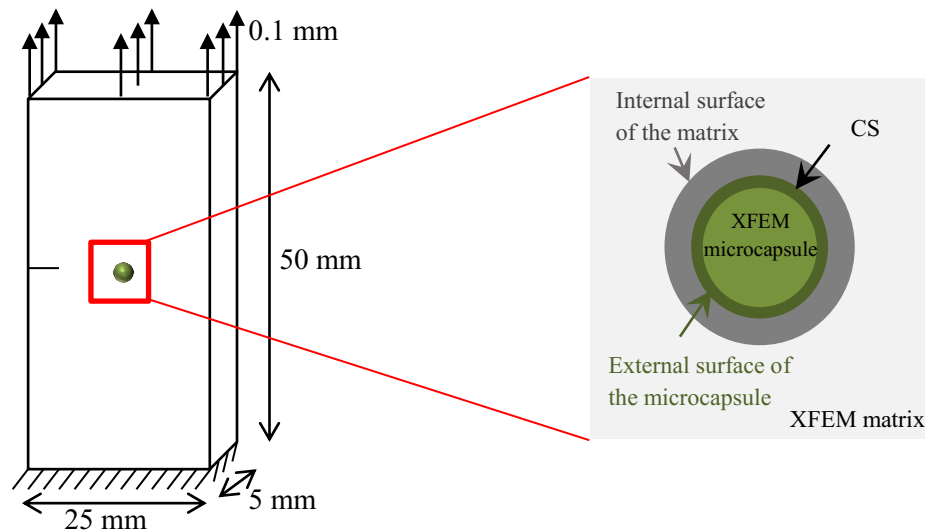


Figure 5.58: Specimens geometry dimensions and modeling techniques.

In order to establish the degree of mesh refinement required to obtain reliable results, several preliminary calculations using a notched sample without microcapsule have been studied. Overall, all element sizes here tested are well below the value ruled by the critical element size discussed in [79, 82] to compromise between accuracy and computational effort. The

element size 1.5 mm and the circumferential element length 0.1 mm around the microcapsule opening, as well as the microcapsule as shown in Figure 5.59.

Table 5.6: The material properties.

Material	E (MPa)	ν	σ^* (MPa)	G_f (N/mm)
Concrete	25000	0.2	6	0.06
Capsule	3600	0.3	10	0.1
Interface	-	-	6 & 0.6	0.06 & 0.006

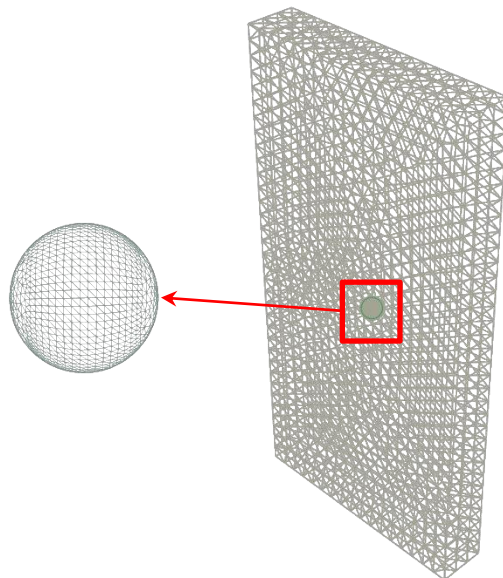


Figure 5.59: The meshing of the specimens.

5.5.2 Parametric studies

Parametric studies of different interfacial fracture properties are performed to study the effects of the interfacial transition zone (itz) between the microcapsule shell and the concrete matrix on the load carrying and the crack patterns. The cohesive surface between the microcapsule shell and the concrete matrix is defined by only two parameters which represent the interfacial fracture properties; the maximum interfacial tensile strength σ^* , which is known as the bonding strength as well and the interfacial fracture energy G_f . These two parameters for the interfacial transition zone (itz) are varied relative to the properties of the concrete for each simulation while the other parameters were fixed as listed in Table 5.6. According to the findings from 2D computational simulations which have been performed in the previous sections, the parametric studies for 3D focused on two main cases for itz; strong interface ($\sigma^* = 6$ Mpa, $G_f = 0.06$ N/mm) and weak interface ($\sigma^* = 0.6$ Mpa, $G_f = 0.006$ N/mm).

5.5.3 Results and discussion

A. Effects of interfacial fracture properties on the load carrying capacity

The effects of the interfacial fracture properties (itz) on the load carrying capacity for strong interface and weak interface are shown in Figure 5.60 and Figure 5.61, respectively. Figure 5.60 shows the impacts of the strong interfacial fracture properties (itz) on the load carrying capacity for 3D and 2D simulations. The 2D simulations have already been performed and discussed in detail including the load displacement curve for strong interface itz 100% in section 5.3.1. In order to illustrate a load displacement curve for 2D simulation equivalent to 3D simulation, the load values from 2D have been multiplied by the specimen width 5 mm. The maximum load carried by the specimen decreased from 548.65 N for 3D modeling to 527.86 N for 2D modeling which means that the reduction in accuracy between 3D and 2D simulations is 3.9%. As a result, in order to reduce the computational cost resulting from 3D modeling, the results of 2D modeling for strong interface could be increased by 3.9% to obtain the same accuracy if it would be modeled as 3D.

Figure 5.61 shows the impacts of the weak interfacial fracture properties (itz) on the load carrying capacity for 3D and 2D simulations. The 2D simulations have already been performed and discussed in detail including the load displacement curve for weak interface itz 10% section 5.3.1. In order to illustrate a load displacement curve for 2D simulation equivalent to 3D simulation, the load values from 2D have been multiplied by the specimen width 5 mm. The maximum load carried by the specimen decreased from 540.68 N for 3D modeling to 522.31 N for 2D modeling which means that the reduction in accuracy between 3D and 2D simulations is 3.4%. Consequently, in order to reduce the computational cost resulting from 3D modeling, the results of 2D modeling for weak interface could be increased by 3.4% to obtain the same accuracy if it would be modeled as 3D.

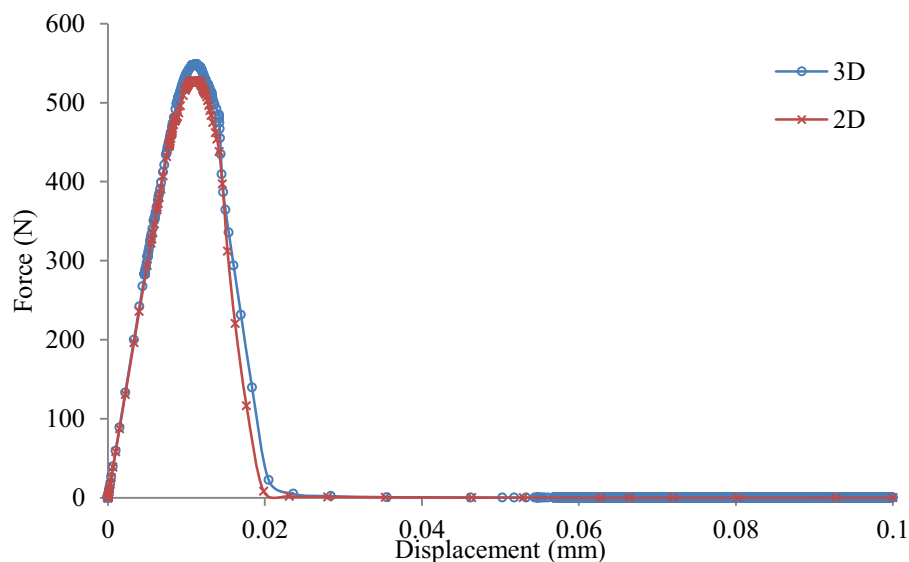


Figure 5.60: Load displacement curves for strong interface in 3D and 2D.

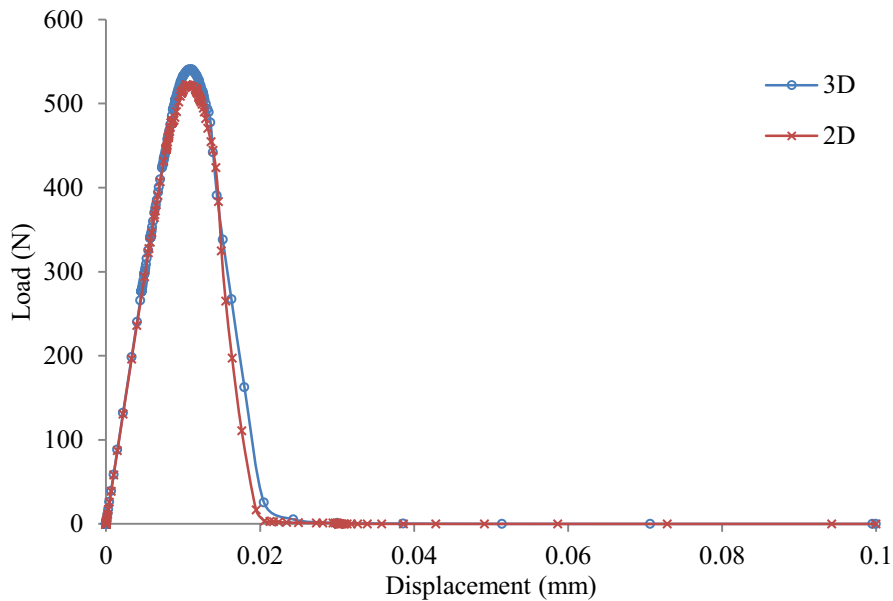


Figure 5.61: Load displacement curves for weak interface in 3D and 2D.

In order to simplify and generalize the reduction factor of accuracy between 3D and 2D simulations for microcapsules self-healing concrete, an average from both reduction percentages for strong and weak interfaces could be calculated (3.65%). For practical engineers, the reduction factor of accuracy 3.65% between 3D and 2D simulation should be considered without caring about the type of interface whether it is weak or strong. That means in order to depend only on the 2D modeling for microcapsules self-healing concrete, the maximum carried load by the specimen from 2D simulations should be increased by 3.65% to obtain almost the same accuracy if it would be modeled as 3D.

B. Effects of interfacial fracture properties on the crack pattern

Figure 5.62 illustrates the impacts of the strong interfacial fracture properties (itz) on the crack pattern. The microcapsule is fractured due to the propagating crack in the concrete which could break the microcapsule. While Figure 5.63 illustrates the impacts of the weak interfacial fracture properties (itz) on the crack pattern. The microcapsule is debonded from the concrete matrix due to the propagating crack in the concrete becoming an interfacial crack once it is encountered with the microcapsule shell. These results from 3D simulations are in good agreement with the other results obtained from 2D simulations which have been performed and discussed in detail in section 5.3.1 for strong interface itz 100% and weak interface itz 10% as illustrated in Figure 5.32(a), (e) respectively. According to this finding, the 2D simulations could be sufficient for modeling the crack pattern in the microcapsules self-healing concrete without increasing the computational cost by performing 3D simulations especially for practical engineers.

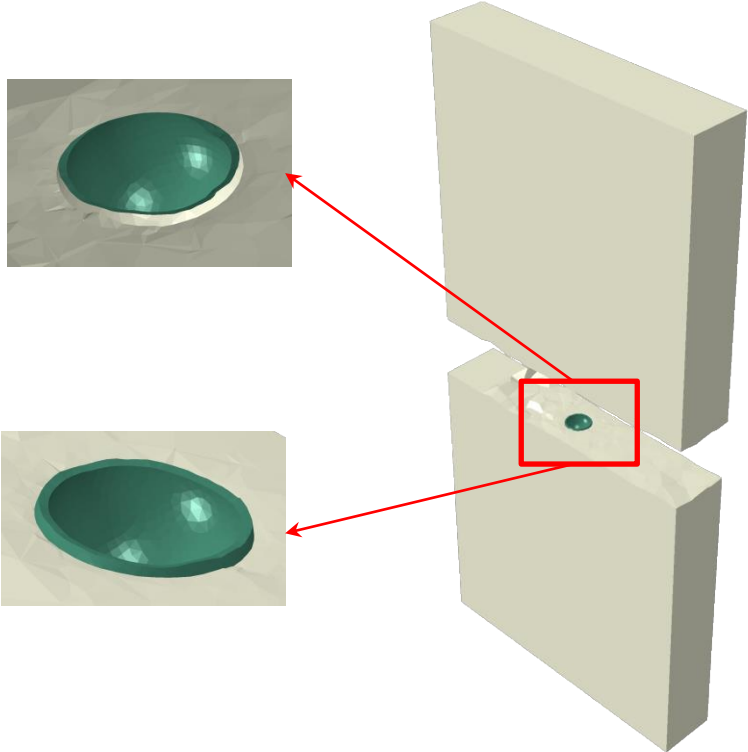


Figure 5.62: Crack pattern specimens with strong interface in 3D.

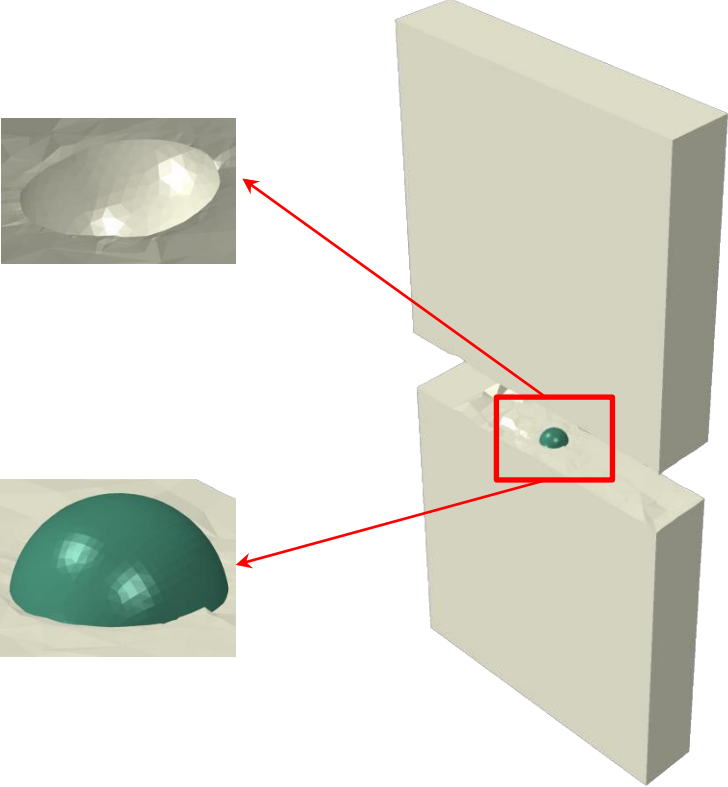


Figure 5.63: Crack pattern specimens with weak interface in 3D.

5.6 Microcapsules Design

In this section, the simulations of the proposed microcapsule design as discussed in chapter 4 are performed based on unit cell (UC), Representative Volume Element (RVE), and Periodic Boundary Conditions (PBC) to study the impacts of microcapsule size and interfacial fracture properties between the microcapsule shell and the concrete matrix, on the load carrying capacity and the probability of fracture or debonding of the microcapsule from the concrete matrix. In addition, the role of the volume fraction (V_f) and the crack width on the microcapsule design are studied.

5.6.1 Volume Fraction ($V_f = 5\%$)

5.6.1.1 Description of the model

2D RVE body centred unit cell concrete samples with one microcapsule and volume fraction ($V_f = 0.05$) are loaded under uniaxial tension. The outer diameter of the microcapsule is 2 mm with four values of core-shell ratio; 1:1, 5:1, 10:1, and 15:1. The microcapsule with the largest core-shell ratio (15:1) has the smallest shell thickness and vice versa. The RVE dimensions of the samples is calculated according to eq. (4.13); $L_{uc} = 4.4$ mm. In order to investigate how the crack will initiate, a preexisting crack with this type of analysis is not required. The overall geometry dimensions of this specimen with the boundary conditions are shown in Figure 5.64. The PBC have been implemented along the four sides of RVE using equation constraint to connect each node with its corresponding node on the other side. Vertical displacement 0.05 mm is applied to the reference point (RP). The simulation was done in Abaqus/Static and assuming plane stress conditions. The material properties listed in Table 5.7 are characterized by [71, 73, 79, 80, 83, 84]. Their parameters are then represented by Young's modulus (E), Poisson's ratio (ν), maximum tensile strength (σ^*), and fracture energy (G_f). For the cohesive surface representing the interaction between the microcapsule and the concrete matrix, the normal and shear fracture properties are assumed to be equal due to the lack of experimental data available in the literature.

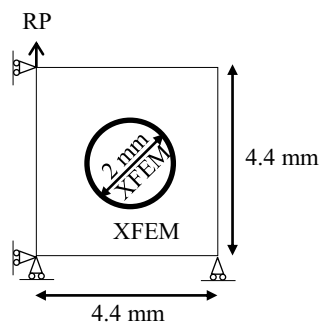


Figure 5.64: RVE geometry dimensions and modeling techniques.

Mesh convergence

Several preliminary calculations, similar to that performed in section 5.3.2.2 have been carried out to study mesh convergence to compromise between accuracy and computational effort. The RVE samples are meshed with Quadrilateral elements (Q4) with full integration. In order to have a periodic mesh to facilitate the application of PBC, the average mesh elements size of RVE is 0.44 mm, the number of elements for each side of RVE is fixed 15,

and the number of circumferential elements around the microcapsule opening is fixed at 25. The average mesh elements size for microcapsule core-shell ratio 1:1 is 0.1 mm with 5 elements through its thickness, for microcapsule core-shell ratio 5:1 is 0.0417 mm with 4 elements through its thickness, for microcapsule core-shell ratio 5:1 is 0.0303 mm with 3 elements through its thickness, and for microcapsule core-shell ratio 5:1 is 0.03125 mm with 2 elements through its thickness, as shown in Figure 5.65.

Table 5.7: The material properties.

Material	E (MPa)	ν	σ^* (MPa)	G_f (N/mm)
Concrete	25000	0.2	6	0.06
Capsule	3600	0.3	10	0.1
Interface	-	-	Varies	Varies

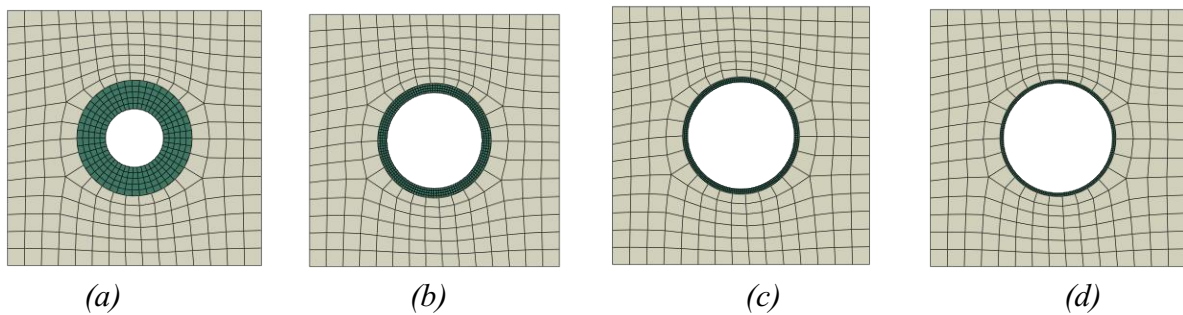


Figure 5.65: The mesh discretization with different microcapsule core-shell ratios, (a) Ratio 1:1 (b) Ratio 5:1 (c) Ratio 10:1 (d) Ratio 15:1.

5.6.1.2 Parametric studies

Parametric studies of different interfacial fracture properties are performed to study the effects of the interfacial transition zone (itz) between the microcapsule shell and the concrete matrix on the load carrying and the crack patterns with four different microcapsule core-shell ratios; 1:1, 5:1, 10:1, and 15:1 as shown in Figure 5.65. The cohesive surface between the microcapsule shell and the concrete matrix is defined by only two parameters which represent the interfacial fracture properties; the maximum interfacial tensile strength σ^* which is known as the bonding strength as well and the interfacial fracture energy G_f . In order to investigate the effects of interfacial strength and fracture energy, parametric studies of five different material inputs for σ^* and G_f were carried out. These two parameters for the interfacial transition zone (itz) are varied relative to the properties of the concrete for each simulation while the other parameters were constant; i.e. they are ranging from 10% ($\sigma^* = 0.6$ Mpa, $G_f = 0.006$ N/mm) to 100% ($\sigma^* = 6$ Mpa, $G_f = 0.06$ N/mm).

5.6.1.3 Results and discussion

A. Effects of interfacial fracture properties and the microcapsule size on the load carrying capacity

The effects of interfacial fracture properties (itz) for the RVE samples with core-shell ratios 1:1, 5:1, 10:1, and 15:1 on load carrying capacity are represented by variation of itz from 10% of the concrete fracture properties ($\sigma^* = 0.6$ Mpa, $G_f = 0.006$ N/mm) to 100%; same as the concrete fracture properties ($\sigma^* = 6$ Mpa, $G_f = 0.06$ N/mm) are demonstrated in Figure 5.66- Figure 5.69. It is apparent that interfacial cohesive characteristics have a significant impact on the load carrying capacity of RVE samples. Figure 5.66 shows the effects of the interfacial fracture properties itz on the load carrying capacity of the RVE with the microcapsule core-shell ratio 1:1. The maximum load of the RVE decreased from 21.3 N for $itz = 100\%$ to 16.9 N for $itz = 10\%$. As a result, it is clear that the interfacial cohesive properties itz have a significant role for governing the load carrying capacity of the RVE samples. The same phenomenon also can be found in Figure 5.67, Figure 5.68, and Figure 5.69 for the microcapsule with ratios 5:1, 10:1, and 15:1, respectively. It is clear that when the interfacial cohesive fracture properties have the same values of the concrete matrix, the higher maximum load carrying capacity will be achieved. Consequently, it is obvious that the higher the itz , the higher the load carrying capacity and vice versa.

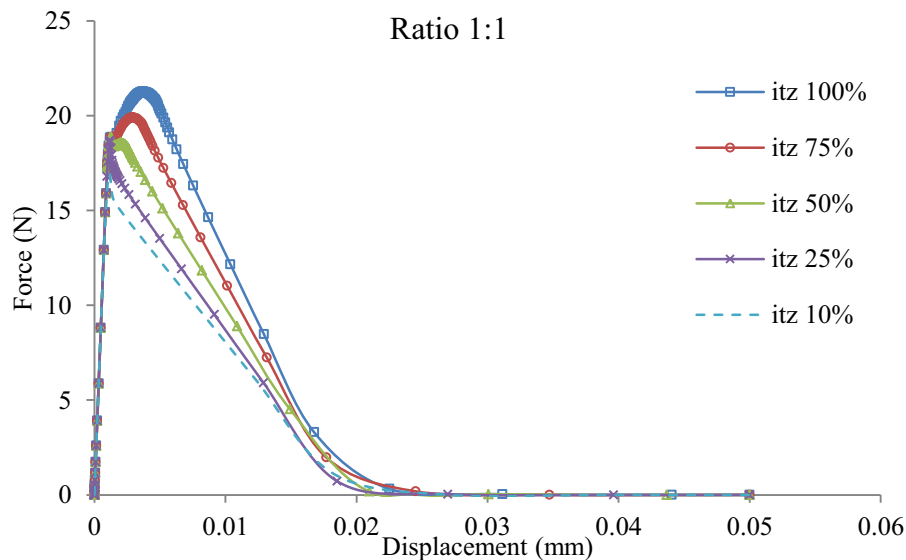


Figure 5.66: Load displacement curves for microcapsule core-shell ratio 1:1 with different itz values.

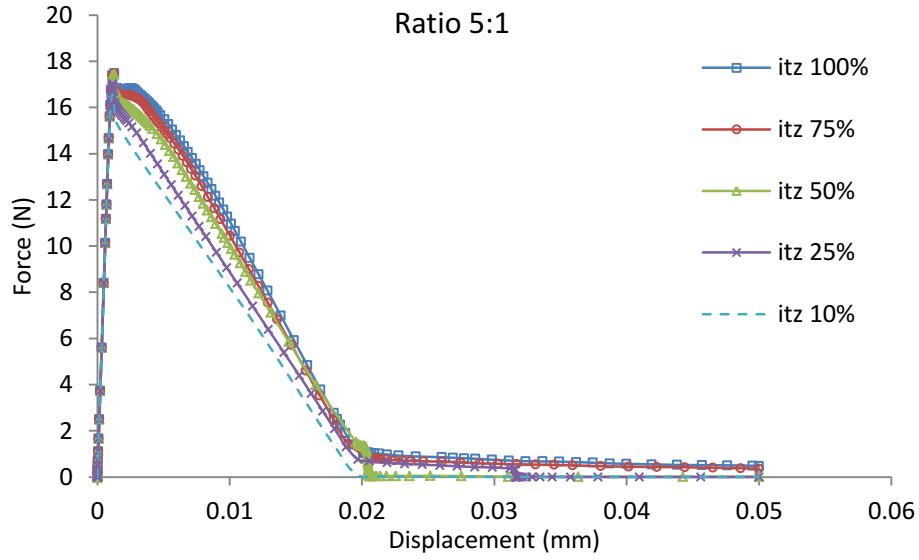


Figure 5.67: Load displacement curves for microcapsule core-shell ratio 5:1 with different itz values.

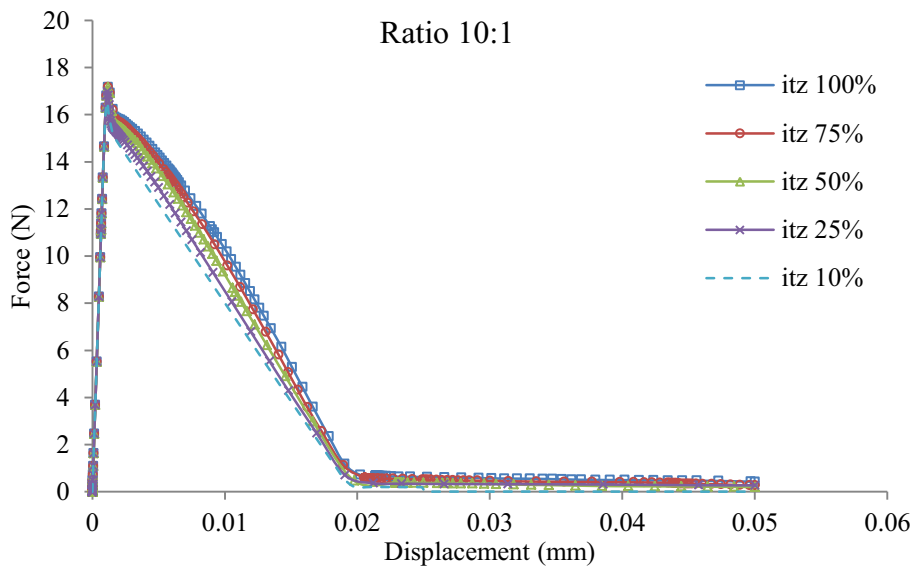


Figure 5.68: Load displacement curves for microcapsule core-shell ratio 10:1 with different itz values.

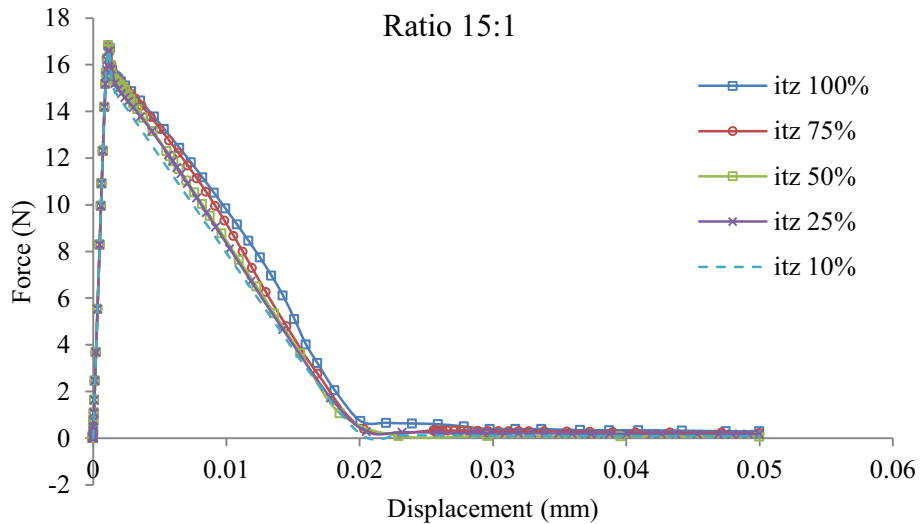


Figure 5.69: Load displacement curves for microcapsule core-shell ratio 15:1 with different itz values.

B. Effects of interfacial fracture properties and the microcapsule size on the maximum carrying load

The effects of the microcapsule size, which is defined by the core-shell ratio on the maximum carrying load for the four RVE samples with different interfacial fracture properties (itz) are shown in Figure 5.70. It is shown that the lower core-shell ratio (larger shell thickness) of the microcapsule, the higher maximum carrying load of the sample. On the other hand, the higher percentage of itz increases the maximum load of the RVE that it can withstand. It also shows that the varying effect of itz on the microcapsule with lower shell thickness is almost constant, as seen in microcapsules core-shell ratio 10:1 and 15:1.

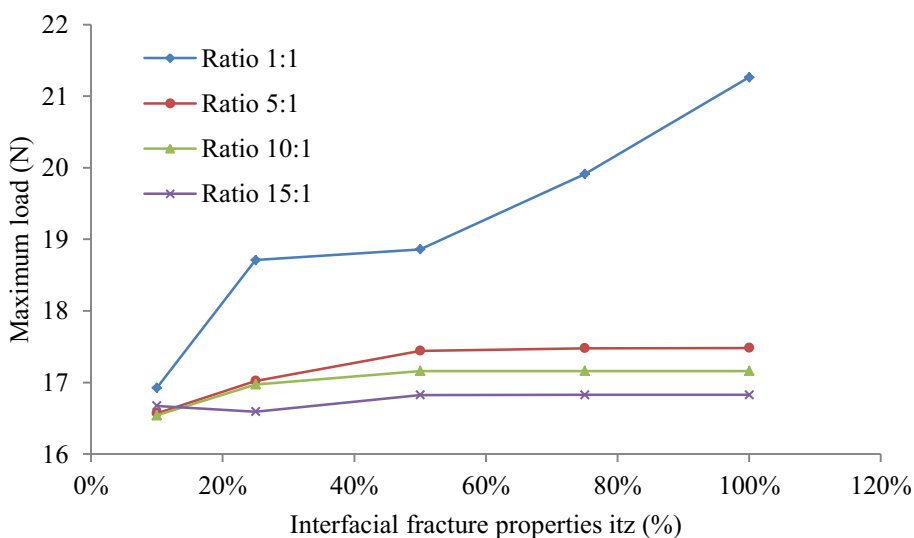


Figure 5.70: Effects of itz ratios to the maximum load with different microcapsule core-shell ratios.

C. Effects of interfacial fracture properties and the microcapsule size on the crack pattern

The effects of the interfacial fracture properties (itz) for RVE samples with volume fraction ($V_f = 5\%$), and microcapsule core-shell ratios 1:1, 5:1, 10:1, and 15:1 on the crack pattern are shown in Figure 5.71, Figure 5.72, Figure 5.73, and Figure 5.74 respectively. The effects of the interfacial fracture properties are represented by variation of itz from 10% of the concrete fracture properties ($\sigma^* = 0.6$ Mpa, $G_f = 0.006$ N/mm) to 100%; same as the concrete fracture properties ($\sigma^* = 6$ Mpa, $G_f = 0.06$ N/mm). Figure 5.71 illustrates that the RVE samples with microcapsule core-shell ratio 1:1 (the largest shell thickness) produced the same crack patterns as the microcapsule is debonded from the concrete matrix regardless of the ratio of the interfacial fracture properties (itz). The propagating crack couldn't break the microcapsule shell even when the interfacial fracture properties have the same values of the concrete matrix, see Figure 5.71 (a)-(e) as an interfacial crack occurs regardless the itz ratio. Figure 5.72 illustrates that the RVE samples with microcapsule core-shell ratio 5:1 and when the itz ratio of the concrete fracture properties ranging between 0%–50% an interfacial crack occurred, and the microcapsule is debonded from the concrete matrix, as shown in Figure 5.72 (a)-(c). When the itz is ranged between 75%-100% the propagating crack became an interfacial crack when it reached the microcapsule shell and broke it from the other side, as illustrated in Figure 5.72 (d)-(e). That means a partial fracture crack is developed when the microcapsule core-shell ratio is 5:1 and the ratio of the interfacial fracture properties between the microcapsule and the concrete matrix (itz) is ranging between 75%-100%. Figure 5.73 illustrates the fracture pattern for RVE with microcapsule core-shell ratio 10:1 and varying of itz ratios. When itz are ranging between 0%–25% an interfacial crack occurs and the microcapsule is debonded from the concrete matrix as shown in Figure 5.73 (a)-(b). However, when the itz is ranging between 50%-100% the propagating crack became an interfacial crack when it reached the microcapsule shell and broke it from the other side, as illustrated in Figure 5.73 (c)-(e). Figure 5.74 illustrates the fracture pattern for RVE with microcapsule core-shell ratio 15:1 and varying of itz ratios. When itz ranging between 0%–25% interfacial cracks occurred, and the microcapsule is debonded from the concrete matrix, as shown in Figure 5.74 (a)-(b). However, when the itz is ranging between 50%-100% the propagating crack could break the microcapsule, as illustrated in Figure 5.74 (c)-(e).

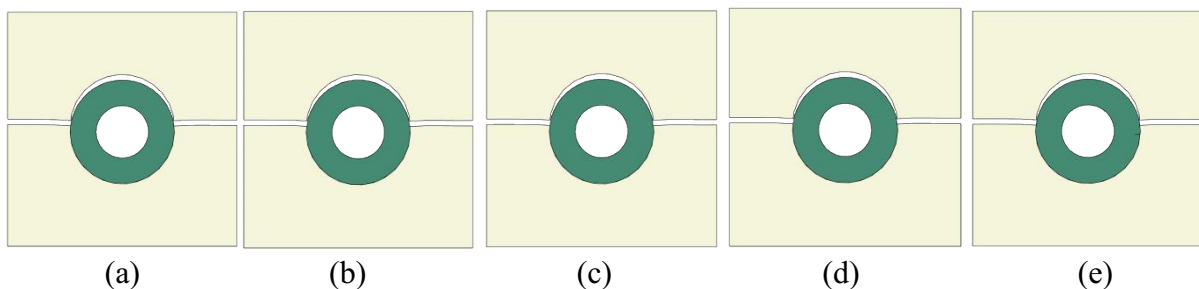


Figure 5.71: Crack pattern of microcapsule ratio 1:1 with different itz ratios. (a) itz 10% (b) itz 25% (c) itz 50% (d) itz 75% (e) itz 100%.

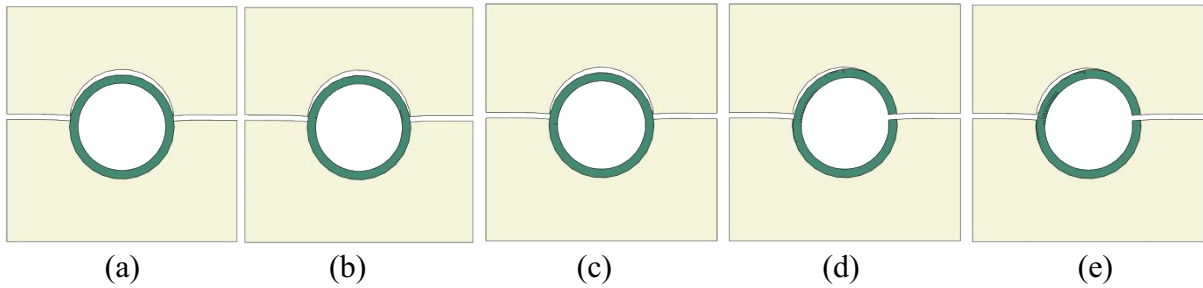


Figure 5.72: Crack pattern of microcapsule ratio 5:1 with different itz ratios. (a) itz 10% (b) itz 25% (c) itz 50% (d) itz 75% (e) itz 100%.

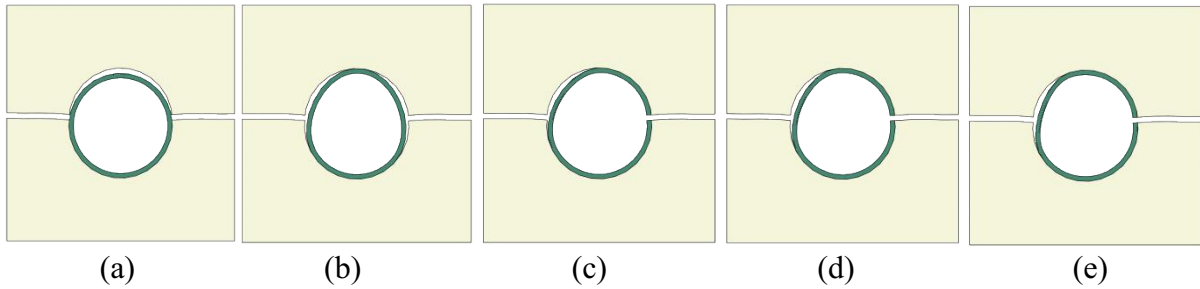


Figure 5.73: Crack pattern of microcapsule ratio 10:1 with different itz ratios. (a) itz 10% (b) itz 25% (c) itz 50% (d) itz 75% (e) itz 100%.

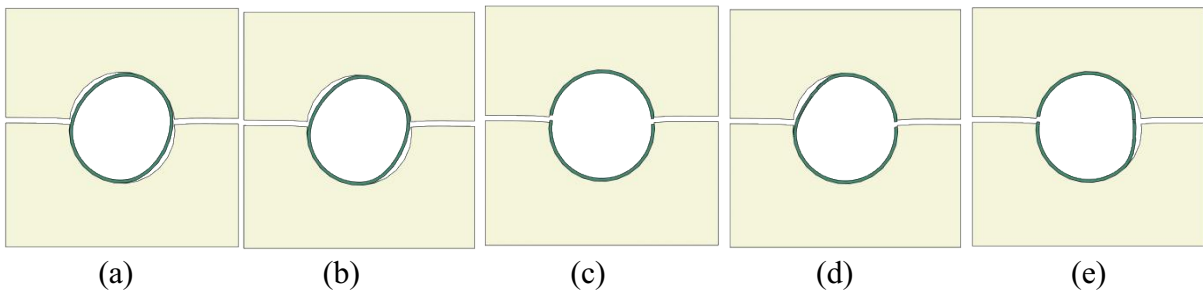


Figure 5.74: Crack pattern of microcapsule ratio 15:1 with different itz ratios. (a) itz 10% (b) itz 25% (c) itz 50% (d) itz 75% (e) itz 100%.

5.6.2 Volume Fraction ($V_f = 25\%$)

5.6.2.1 Description of the model

2D RVE body centred unit cell concrete samples with one microcapsule and volume fraction ($V_f = 0.25$) are loaded under uniaxial tension. The outer diameter of the microcapsule is 2 mm with four values of core-shell ratio; 1:1, 5:1, 10:1, and 15:1. The microcapsule with the largest core-shell ratio (15:1) has the smallest shell thickness and vice versa. The RVE dimensions of the samples is calculated according to eq. (4.13); $L_{uc} = 2.6$ mm. In order to investigate how the crack will initiate, a preexisting crack with this type of analysis is not required. The overall geometry dimensions of this specimen with the boundary conditions are shown in Figure 5.75. The PBC have been implemented along the four sides of RVE using equation constraint to connect each node with its corresponding node on the other side. Vertical displacement 0.05 mm is applied to the reference point (RP). The simulation was done in Abaqus/Static and assuming plane stress conditions. The material properties are the same which have been used in section 5.6.1 and listed in Table 5.7.

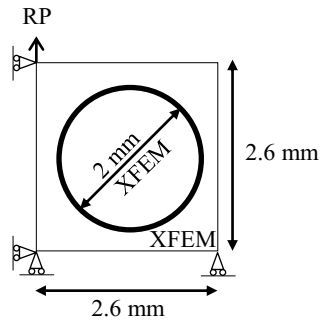


Figure 5.75: RVE geometry dimensions and modeling techniques.

Mesh convergence

Several preliminary calculations have been carried out to study mesh convergence similar to that performed in section 5.3.2.2, to compromise between accuracy and computational effort. The RVE samples are meshed with Quadrilateral elements (Q4) with full integration. In order to have a periodic mesh to facilitate applying PBC, the average mesh elements size of RVE is 0.26 mm, the number of elements for each side of RVE is fixed at 10, and the number of circumferential elements around the microcapsule opening is fixed at 25. The average mesh elements size for microcapsule core-shell ratio 1:1 is 0.1 mm with 5 elements through its thickness, for microcapsule core-shell ratio 5:1 is 0.0417 mm with 4 elements through its thickness, for microcapsule core-shell ratio 5:1 is 0.0303 mm with 3 elements through its thickness, and for microcapsule core-shell ratio 5:1 is 0.03125 mm with 2 elements through its thickness as shown in Figure 5.76.

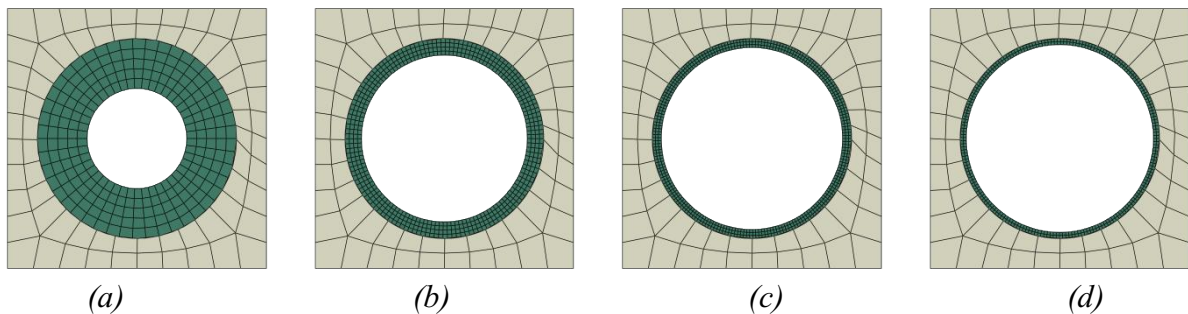


Figure 5.76: The mesh discretization with different microcapsule core-shell ratios, (a) Ratio 1:1 (b) Ratio 5:1 (c) Ratio 10:1 (d) Ratio 15:1.

5.6.2.2 Parametric studies

Parametric studies of different interfacial fracture properties are performed to study the effects of the interfacial transition zone (itz) between the microcapsule shell and the concrete matrix on the load carrying capacity and the crack patterns with four different microcapsule core-shell ratios; 1:1, 5:1, 10:1, and 15:1 as shown in Figure 5.76. The cohesive surface between the microcapsule shell and the concrete matrix is defined by only two parameters which represent the interfacial fracture properties; the maximum interfacial tensile strength σ^* which is known as the bonding strength as well and the interfacial fracture energy G_f . In order to investigate the effects of interfacial strength and fracture energy, parametric studies of five different material inputs for σ^* and G_f were carried out. These two parameters for the interfacial transition zone (itz) are varied relative to the properties of the concrete for each simulation

while the other parameters were constant; i.e. they are ranging from 10% ($\sigma^* = 0.6$ Mpa, $G_f = 0.006$ N/mm) to 100% ($\sigma^* = 6$ Mpa, $G_f = 0.06$ N/mm).

5.6.2.3 Results and discussion

A. Effects of interfacial fracture properties and the microcapsule size on the load carrying capacity

The effects of interfacial fracture properties (itz) for the RVE samples with core-shell ratios 1:1, 5:1, 10:1, and 15:1 on load carrying capacity, are represented by variation of itz from 10% of the concrete fracture properties ($\sigma^* = 0.6$ Mpa, $G_f = 0.006$ N/mm) to 100%; same as the concrete fracture properties ($\sigma^* = 6$ Mpa, $G_f = 0.06$ N/mm) are demonstrated in Figure 5.77-Figure 5.80. It is apparent that interfacial cohesive characteristics have a significant impact on the load carrying capacity of RVE samples. Figure 5.77 shows the effects of the interfacial fracture properties itz on the load carrying capacity of the RVE with the microcapsule core-shell ratio 1:1. The maximum load of the RVE decreased from 8.9 N for itz = 100% to 4.5 N for itz = 10%. Consequently, it is clear that the interfacial cohesive properties itz have a significant role for governing the load carrying capacity of the RVE samples. The same phenomenon also can be found in Figure 5.78, Figure 5.79, and Figure 5.80 for the microcapsule with ratios 5:1, 10:1, and 15:1, respectively. It is clear that when the interfacial cohesive fracture properties have the same values of the concrete matrix, the higher maximum load carrying capacity will be achieved. The results clearly show that the higher the itz, the higher the load carrying capacity and vice versa.

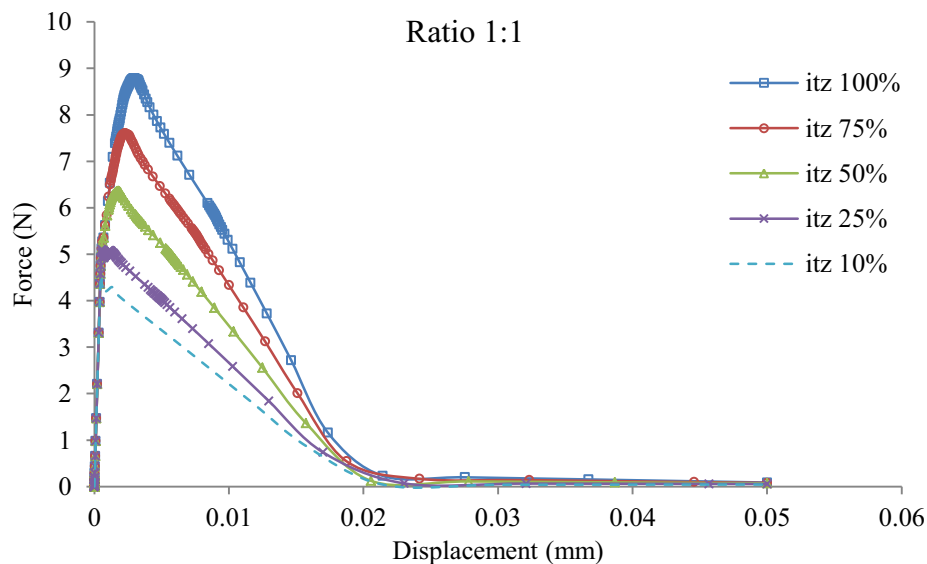


Figure 5.77: Load displacement curves for microcapsule core-shell ratio 1:1 with different itz values.

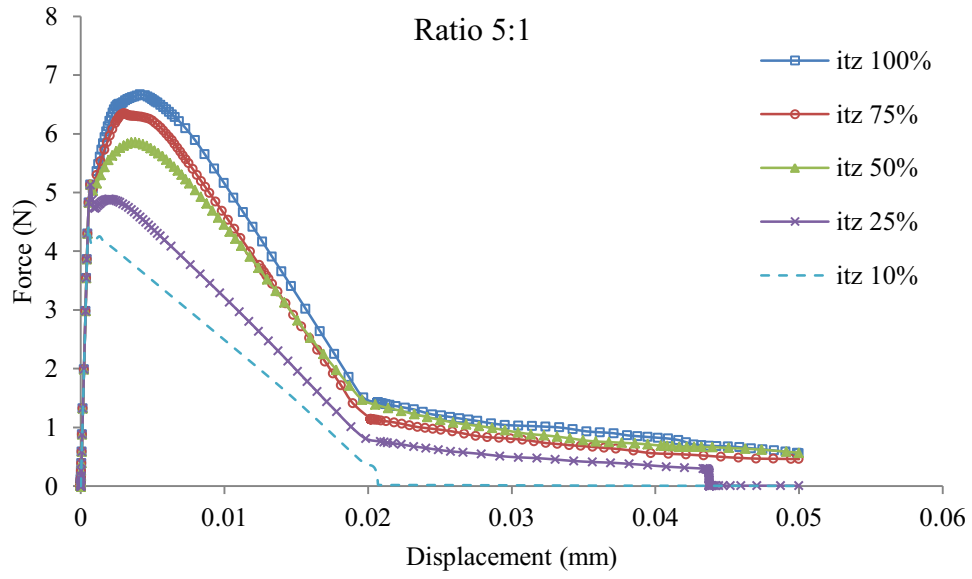


Figure 5.78: Load displacement curves for microcapsule core-shell ratio 5:1 with different itz values.

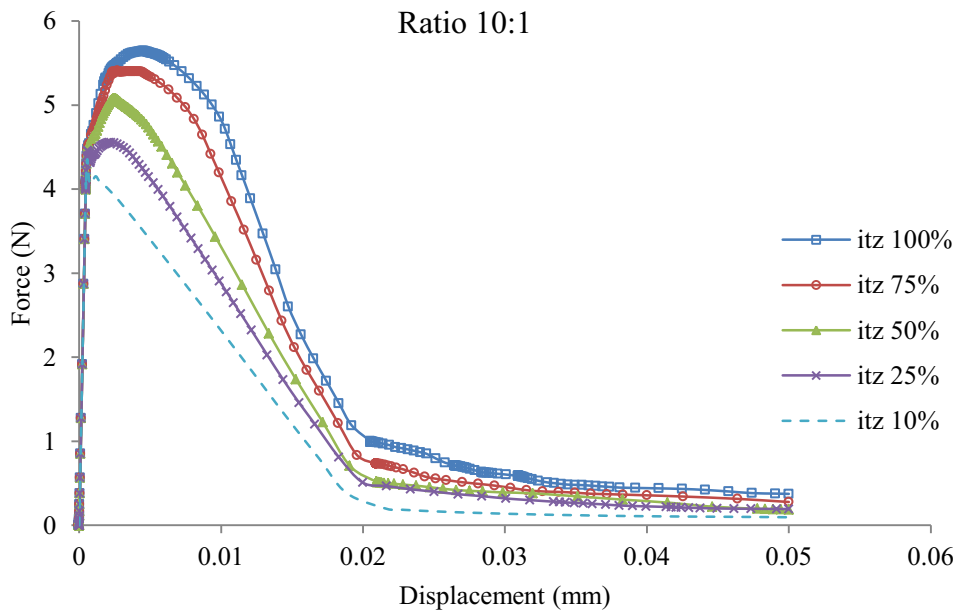


Figure 5.79: Load displacement curves for microcapsule core-shell ratio 10:1 with different itz values.

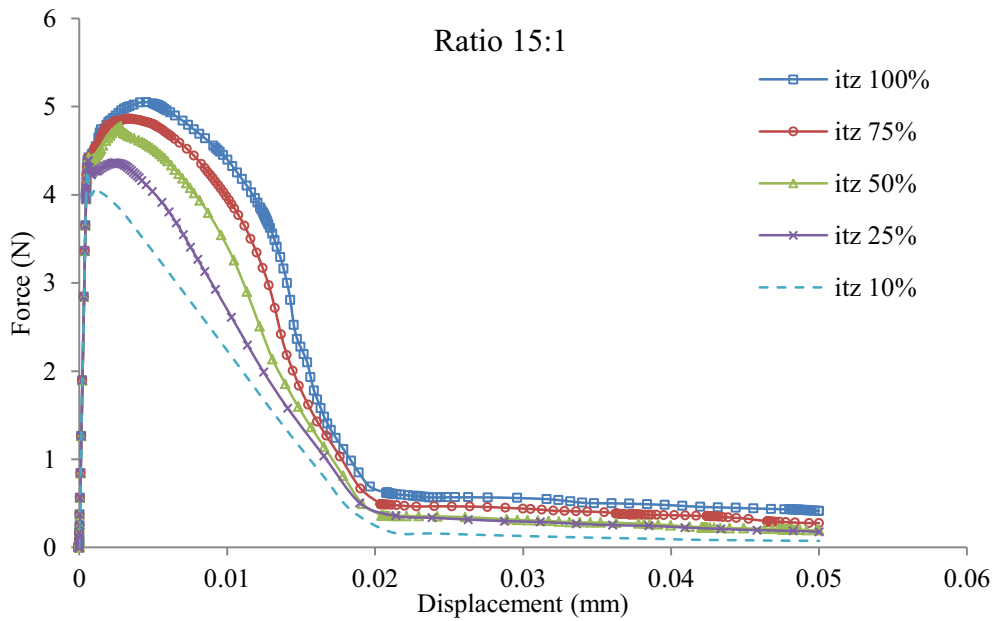


Figure 5.80: Load displacement curves for microcapsule core-shell ratio 15:1 with different itz values.

B. Effects of interfacial fracture properties and the microcapsule size on the maximum carrying load

The effects of the microcapsule size, which is defined by the core-shell ratio on the maximum carrying load for the four RVE samples with different interfacial fracture properties (itz) are shown in Figure 5.81. It is shown that the lower core-shell ratio (larger shell thickness) of the microcapsule, the higher the maximum carrying load of the sample. But on other hand, the higher percentage of itz increases the maximum load of the RVE that it can withstand.

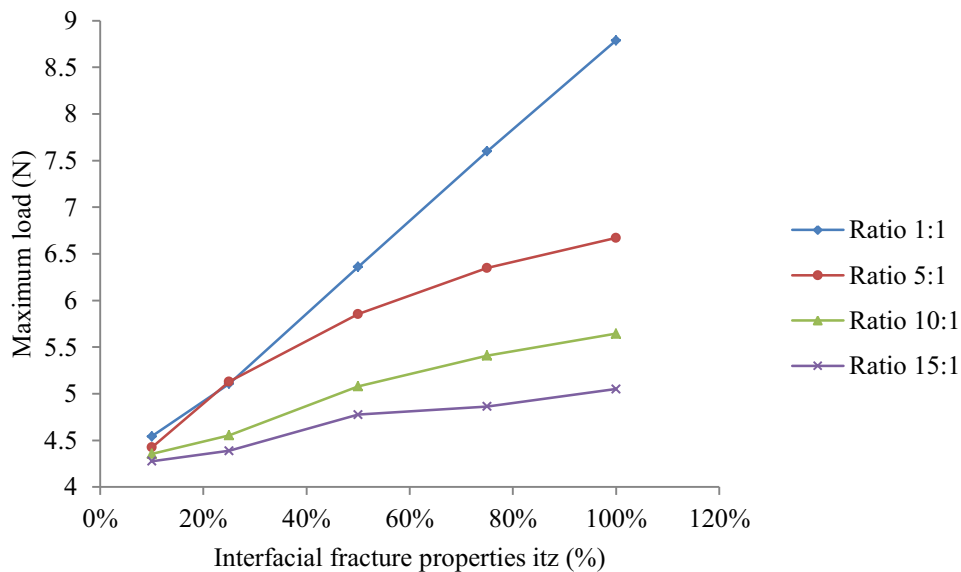


Figure 5.81: Effects of itz ratios to the maximum load with different microcapsule core-shell ratios.

C. Effects of interfacial fracture properties and the microcapsule size on the crack pattern

The effects of the interfacial fracture properties (itz) for RVE samples with volume fraction ($V_f = 25\%$) and microcapsule core-shell ratios 1:1, 5:1, 10:1, and 15:1 on the crack pattern are shown in Figure 5.82, Figure 5.83, Figure 5.84, and Figure 5.85 respectively. The effects of the interfacial fracture properties are represented by variation of itz from 10% of the concrete fracture properties ($\sigma^* = 0.6$ Mpa, $G_f = 0.006$ N/mm) to 100%; same as the concrete fracture properties ($\sigma^* = 6$ Mpa, $G_f = 0.06$ N/mm). Figure 5.82 illustrates that the RVE samples with microcapsule core-shell ratio 1:1 (the largest shell thickness) produced the same crack patterns as the microcapsule is debonded from the concrete matrix regardless of the ratio of the interfacial fracture properties (itz). The propagating crack couldn't break the microcapsule shell even when the interfacial fracture properties have the same values of the concrete matrix, see Figure 5.82 (a)-(e) as an interfacial crack occurred regardless the itz ratio. Figure 5.83 illustrates that the RVE samples with microcapsule core-shell ratio 5:1 and when the itz ratio of the concrete fracture properties ranging between 0%–50% an interfacial crack occurred, and the microcapsule is debonded from the concrete matrix, as shown in Figure 5.83 (a)-(c). When the itz are ranging between 75%–100% the propagating crack became an interfacial crack when it reached the microcapsule shell and broke it from the other side, as illustrated in Figure 5.83 (d)-(e). That means a partial fracture crack is developed when the microcapsule core-shell ratio is 5:1 and the ratio of the interfacial fracture properties between the microcapsule and the concrete matrix (itz) is ranging between 75%–100%. Figure 5.84 illustrates the fracture pattern for RVE with microcapsule core-shell ratio 10:1 and varying of itz ratios. When itz ranging between 0%–25% an interfacial crack occurs and the microcapsule is debonded from the concrete matrix as shown in Figure 5.84 (a)-(b). However, when the itz is ranging between 50%–75% the propagating crack became an interfacial crack when it reached the microcapsule shell and broke it from the other side, as illustrated in Figure 5.84 (c)-(d). While when the itz is 100% (same as concrete fracture properties) the propagating crack could break the microcapsule, as illustrated in Figure 5.84 (e). Figure 5.85 illustrates the fracture pattern for RVE with microcapsule core-shell ratio 15:1 and varying of itz ratios. When itz are ranging between 0%–25% interfacial cracks occurred and the microcapsule is debonded from the concrete matrix as shown in Figure 5.85 (a)-(b). However, when the itz is ranging between 50%–100% the propagating crack could break the microcapsule, as illustrated in Figure 5.85 (c)-(e).

Comparing between the crack patterns generate from this section for RVE with volume fraction ($V_f = 25\%$) and the crack patterns generate from the previous section 5.6.1 for RVE with volume fraction ($V_f = 5\%$), it shows that increasing the volume fraction leads to increase the possibility of the microcapsule being fractured.

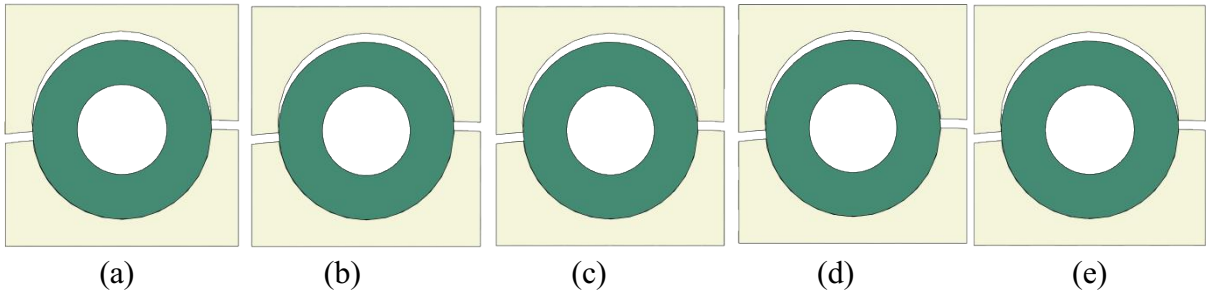


Figure 5.82: Crack pattern of microcapsule ratio 1:1 with different itz ratios. (a) itz 10% (b) itz 25% (c) itz 50% (d) itz 75% (e) itz 100%.

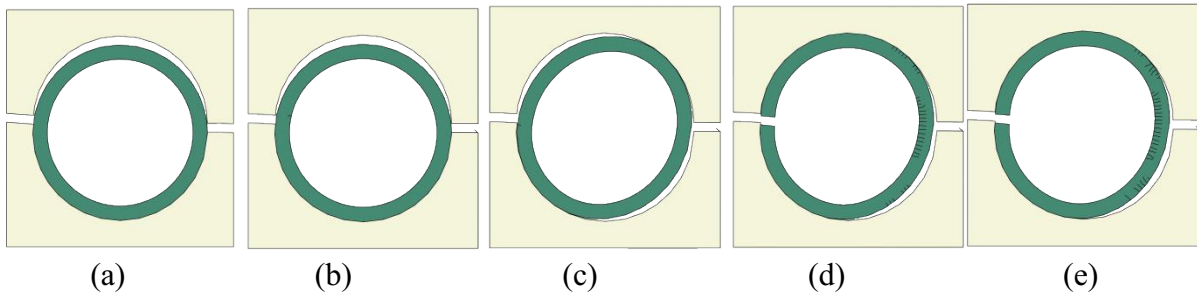


Figure 5.83: Crack pattern of microcapsule ratio 5:1 with different itz ratios. (a) itz 10% (b) itz 25% (c) itz 50% (d) itz 75% (e) itz 100%.

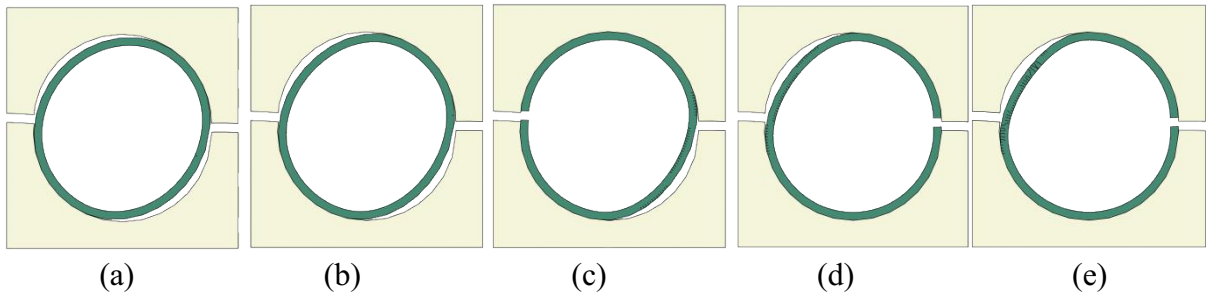


Figure 5.84: Crack pattern of microcapsule ratio 10:1 with different itz ratios. (a) itz 10% (b) itz 25% (c) itz 50% (d) itz 75% (e) itz 100%.

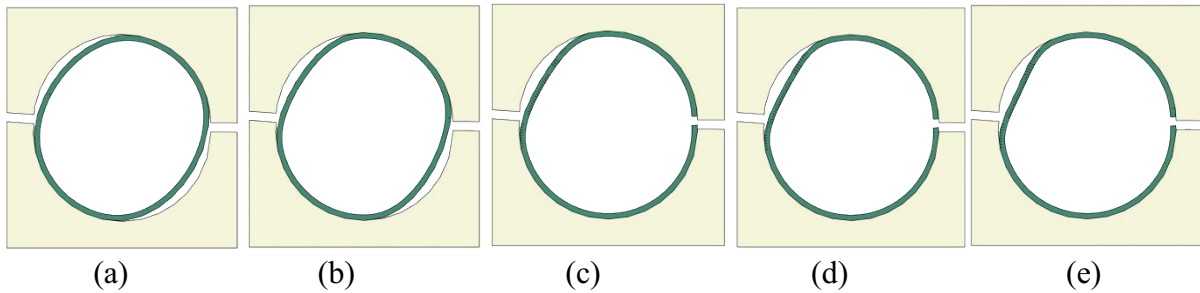


Figure 5.85: Crack pattern of microcapsule ratio 15:1 with different itz ratios. (a) itz 10% (b) itz 25% (c) itz 50% (d) itz 75% (e) itz 100%.

6 Conclusions

In this chapter, a short review of the entire research work in this thesis is given. Engineering contributions that this research made will be emphasised and summarized. At the end some prospective points for the future research work are demonstrated.

6.1 Summary and Conclusions

In this thesis, the extended finite element method (XFEM) and cohesive surface technique (CS) have been employed to study the healing efficiency and the potential of fracture and debond of the microcapsules, as well as the solidified healing agents. In addition to studying the accuracy of the proposed modeling techniques, a comparison with the zero thickness cohesive elements (CIE) has been conducted on the fracture modeling of encapsulated self-healing concrete. A simple proposed modeling approach to study the microcapsule clustering effect has been designed to investigate the effective contact surface between the microcapsule and the concrete matrix. 3D computational simulations are performed to study the possibilities of fracture and debonding of the microcapsule from the concrete matrix. This study has validated the 2D computational simulations and has estimated the accuracy difference ratio between 2D and 3D simulations. Also, a proposed design method for microcapsules is developed based on Unit Cell (UC), Representative Volume Element (RVE), Periodic Boundary Conditions (PBC), and associated them to the volume fraction (V_f) and the crack width as variables. From the proposed computational modeling performed and the results obtained in this thesis, the following conclusions may be drawn. Each point below summarizes the results of each simulation type. The summarized results go in the same sequence as the simulations performed in the previous chapter of this thesis:

1. The proposed healing efficiency simulations:
 - The healed-crack length (L_h) has a significant role for governing the specimen strength as the higher healed-crack length ratio, the higher maximum carrying load of the specimen.
 - The interfacial cohesive properties (itz) between the solidified healing agent and the cracked surfaces of the concrete specimen have a significant role for governing the load carrying capacity of the specimen. The higher the itz, the higher the load carrying capacity and vice versa.
 - The cracks will initiate and propagate through the concrete matrix only, when the itz ratio is 75%–100% from the fracture properties of the solidified healing agent and L_h 100% (equal to the total crack length).
 - The interfacial cracks occur and the solidified healing agent will be debonded from the concrete matrix, when the itz ratio is 0%- 25% from the fracture properties of the solidified healing agent.
 - There is a possibility for developing interfacial cracks and concrete cracks concurrently when the interfacial fracture properties are 50% of the solidified healing agent fracture properties.
 - The mixed crack patterns are developed when the L_h ratio ranges from 75%-25% and the itz ratio ranges from 100%–75%. As a concrete crack initiates first and propagates

through the concrete matrix then an interfacial crack propagates through the interface zone between the healing agent and the concrete matrix.

2. The proposed 2D microcapsules fracture simulations:

- The interfacial strength between the microcapsule shell and the concrete matrix has a significant influence on the load carrying capacity and the crack pattern of the sample.
- The interfacial fracture energy (G_f) has no significant impact on the load carrying capacity of self-healing concrete. However, it will affect on the fracture pattern whether fractured or debonded of the microcapsule from the concrete as when the G_f ratio lower than 10% of the concrete fracture energy, an interfacial crack occurs and the microcapsule will be debonded from the concrete matrix.
- The interfacial fracture properties (itz) between the microcapsule shell and the concrete matrix have a great impact on the maximum carrying load of the SHC samples. The higher the itz, the higher the maximum carrying load of the samples.
- The interfacial fracture properties (itz) also affect the crack pattern. However, it is not recommended that the microcapsule core-shell ratio is 1:1 which has the largest shell thickness but smallest volume of the healing agent. Consequently, the debonding of the microcapsule from the concrete will happen regardless the ratios of itz. Otherwise, when itz are lower than 50% of concrete fracture properties, it will result in a greater possibility for the debonding of the microcapsule from the concrete. Such a result proves the credibility of the proposed model, in comparison to the aforementioned study that was done by the zero thickness cohesive element approach. As this previous study concluded, if itz are less than the concrete fracture properties will lead to the debonding of the microcapsule from the concrete.
- A partial fracture crack develops when the interfacial strength is high value (same as concrete) and interfacial fracture energy is low value (i.e., 10 % of concrete). On the contrary, a partial interfacial crack develops when the interfacial strength is 25 % of concrete strength and fracture energy is high value (same as concrete matrix).
- The microcapsule size represented by core-shell ratio has a huge impact on the maximum carrying load of the SHC specimens. The lower core-shell ratio (larger shell thickness) leads to increase of the specimen maximum carrying load and vice versa. This result proves the accuracy of the proposed model, in comparison to a previous study for the same specimens' conditions that had modeled by the zero thickness cohesive element approach and had shown that there is no impact from the core-shell ratio on the maximum load carried by the specimen.
- The microcapsule core-shell ratio has also a great impact on the crack pattern, as it determines whether the microcapsule will fracture or debond from the concrete. The greater the core-shell ratio (smaller shell thickness), the greater the likelihood of microcapsules being fractured.
- It is important not only to take care of microcapsules size but also the surfaces texture during the manufacturing process to ascertain that a sufficient contact interaction surface between the microcapsule and the concrete will be developed to assure the breakage of the microcapsule and the subsequent release of the healing agent.
- It is important to note that the proposed modeling approach displays great accuracy in relation to the maximum carrying load and the crack pattern of the SHC specimens compared to the zero thickness cohesive element approach. Such results confirm its

disadvantages, such as artificial compliance and mesh dependency, which is reported in another study.

- Additionally, there is no implementation or special elements or script required for the proposed modeling as the XFEM and CS techniques already have been implemented into Abaqus software which it makes the modeling process simpler. On the contrary to the zero thickness cohesive element approach requires script in order to insert them between the meshed elements which create complications in the modeling process for practical engineers especially Re-analysis and testing of several design alternatives.
3. The proposed microcapsule clustering simulation:
- The capsular circumferential contact length (Lcs) between the microcapsule shell and the concrete matrix has a great impact on the maximum carrying load of the SHC samples. The higher the Lcs ratio, the greater the load carrying capacity of the specimen and vice versa.
 - The capsular clustering which is represented by the ratio of the contact length between the concrete matrix and the microcapsule (Lcs) to the microcapsule circumference length, has a significant role for determining whether the microcapsule will fracture or debond from the concrete matrix. As the higher the Lcs ratio, the higher probability of the microcapsule being fractured and vice versa.
 - The microcapsule debonds when Lcs ratio ranges from 0-25% as the propagating crack couldn't break the microcapsule shell. When Lcs 50% the propagating crack breaks the microcapsule shell from only one side and it debonded from the other side. While when the Lcs is 75%, an interesting crack pattern is generated as the propagating crack breaks the microcapsule shell completely from one side and partial fractures and debonded the microcapsule from the other side. The microcapsule is completely fractured when the Lcs 100%.
 - The developed modeling approach for studying the capsular clustering has a great advantage, as it is a simple 2D simulation for one single microcapsule but with it, every degree of clustering can be modeled without any complications of mesh discretization, which occurs for modeling the random distribution of microcapsules. In addition, there is the higher computational cost of the latter's modeling.
4. The proposed 3D microcapsules fracture simulation:
- The results obtained from the 3D simulation are in a good agreement with the results obtained from 2D simulations for studying the load carrying capacity and the crack pattern.
 - In order to reduce the computational cost resulting from 3D modeling, the results of 2D modeling for strong interface (itz 100%) and weak interface (itz 10%) could be increased by 3.9% and 3.4%, respectively to obtain the same accuracy if it would be modeled as 3D.
 - In order to simplify and generalize the reduction factor of accuracy between 3D and 2D simulations for microcapsules self-healing concrete, an average from both reduction percentages for strong and weak interfaces could be calculated (3.65%). As a result, for practical engineers, the reduction factor of accuracy 3.65% between 3D and 2D simulation should be considered without caring about the type of interface whether it is weak or strong. That means in order to depend only on the 2D modeling

for microcapsules self-healing concrete, the maximum carried load by the specimen from 2D simulations should be increased by 3.65% to obtain almost the same accuracy if it would be modeled as 3D.

- According to these findings from performing 3D simulations, the 2D simulations could be sufficient for modeling the fracture of the microcapsules self-healing concrete without increasing the computational cost by performing 3D simulations, especially for practical engineers.
5. The developed microcapsules design method simulation:
- The interfacial cohesive characteristics have a significant impact on the load carrying capacity of RVE samples as the higher the itz, the higher the load carrying capacity and vice versa.
 - The microcapsule size represented by core-shell ratio has an impact on the maximum carrying load of the RVE samples. The lower core-shell ratio (larger shell thickness) of the microcapsule, the higher maximum carrying load of the sample.
 - The interfacial cohesive characteristics (itz), is directly proportional to the RVE sample strength. On the contrary, the microcapsule core-shell ratio, and the volume fraction (V_f) are inversely proportional to the sample capacity. It has also been noticed that the varying of the itz on the microcapsule with higher microcapsule core-shell ratio and lower V_f almost has no effect on the RVE sample strength.
 - Increasing the volume fraction (V_f) leads to an increase in the possibility of the microcapsule being fractured.
 - The interfacial fracture properties (itz) and the microcapsule core-shell ratio, and the volume fraction (V_f) also affect the crack pattern as increasing them leads to an increase the possibility of the microcapsule being fractured. However, it is not recommended that the microcapsule core-shell ratio is 1:1, which has the largest shell thickness but smallest volume of the healing agent. Consequently, the debonding of the microcapsule from the concrete will happen regardless of the ratios of itz. Generally, when the itz are lower than 50% of concrete fracture properties, it will result in a greater possibility for the debonding of the microcapsule from the concrete. A partial fracture/ interfacial crack develops when the itz range between 50%-75%. The microcapsule fractures when the itz are range between 75%-100%.
 - Although the proposed design method for microcapsules is very simple and neglects the random distribution of the microcapsules. However, it is helpful tool to design the microcapsules size with the consideration of the sufficient volume of healing agent to heal a specific crack width. As it is based on unit cell (UC), Representative Volume Element (RVE), Periodic Boundary Conditions (PBC), and associates them with the volume fraction (V_f) and the crack width as variables. In addition, the results obtained from the computational simulations for the proposed design of microcapsules are in a good agreement with the previous proposed computational fracture modeling of encapsulated self-healing concrete.

6.2 Future Work

Here are some recommended topics which could be considered future work, such as:

- Fracture modeling with a random distribution of microcapsules inside the concrete matrix. A possible extension of this work is to apply Monte Carlo simulation in order to generate the random distribution of the microcapsules. However, these simulations would be computationally expensive in addition to the complications generated from mesh discretization and capsular clustering. Computational simulations for RVE samples could be a useful improvement to reduce the computational cost.
- Modeling the diffusion of healing agents from the microcapsules to the crack surface under capillary forces.
- Modeling the healing process (solidification) which is mainly phase transformation of healing agents inside the crack surfaces which are released after breakage of microcapsules from a liquid state to a solid state.

References

- [1] S. K. Ghosh, *Self-healing materials: fundamentals, design strategies, and applications*. Wiley Online Library, 2009.
- [2] T. Rabczuk, "Computational methods for fracture in brittle and quasi-brittle solids: State-of-the-art review and future perspectives," *ISRN Applied Mathematics*, vol. 2013, p. 849231, 2013.
- [3] Y. X. Tang and H. N. Chen, "Simulation of crack propagation in concrete based on extended finite element method," in *Key Engineering Materials*, 2018, vol. 783, pp. 165-169: Trans Tech Publ.
- [4] C. Dry, "Matrix cracking repair and filling using active and passive modes for smart timed release of chemicals from fibers into cement matrices," *Smart Materials and Structures*, vol. 3, no. 2, p. 118, 1994.
- [5] H. Mihashi, Y. Kaneko, T. Nishiwaki, and K. Otsuka, "Fundamental study on development of intelligent concrete characterized by self-healing capability for strength," *Transactions of the Japan Concrete Institute*, vol. 22, pp. 441-450, 2000.
- [6] S. R. Sharp and G. G. Clemeña, "State-of-the-art survey of advanced materials and their potential application in highway infrastructure," Virginia Transportation Research Council, 2004.
- [7] H. E. J. G. Schlangen, H. M. Jonkers, S. Qian, and A. Garcia, "Recent advances on self healing of concrete," presented at the FraMCoS-7: Proceedings of the 7th International Conference on Fracture Mechanics of Concrete and Concrete Structures, Jeju Island, Korea, 23-28 May 2010, 2010-05-23, 2010. Available: <http://resolver.tudelft.nl/uuid:46a578c8-de01-4044-92a9-fc814c7102e6>
- [8] K. Van Tittelboom and N. De Belie, "Self-healing in cementitious materials—A review," *Materials*, vol. 6, no. 6, pp. 2182-2217, 2013.
- [9] G. Souradeep and H. W. Kua, "Encapsulation technology and techniques in self-healing concrete," *Journal of Materials in Civil Engineering*, vol. 28, no. 12, p. 04016165, 2016.
- [10] M. Hussin *et al.*, "A review of self-healing concrete research development," 2014.
- [11] T. Westerbeek, "Self-healing Materials Radio Netherlands," ed, 2005.
- [12] T. Kishi, Ahn, T., Hosoda, A., Suzuki, S. and Takaoka, H., "Self healing behaviour by cementitious recrystallization of cracked concrete incorporating expansive agent," in *First International Conference on Self Healing Materials, Noordwijk, The Netherlands, 2007. 4*, 2007.
- [13] W. Zhong and W. Yao, "Influence of damage degree on self-healing of concrete," *Construction building materials*, vol. 22, no. 6, pp. 1137-1142, 2008.
- [14] H.-W. Reinhardt and M. Jooss, "Permeability and self-healing of cracked concrete as a function of temperature and crack width," *Cement concrete research*, vol. 33, no. 7, pp. 981-985, 2003.
- [15] M. Şahmaran and V. C. Li, "Durability of mechanically loaded engineered cementitious composites under highly alkaline environments," *Cement and Concrete Composites*, vol. 30, no. 2, pp. 72-81, 2008.
- [16] S. Jacobsen and E. J. Sellevold, "Self healing of high strength concrete after deterioration by freeze/thaw," *Cement and Concrete Research*, vol. 26, no. 1, pp. 55-62, 1996.
- [17] C. Edvardsen, "Water permeability and autogenous healing of cracks in concrete," in *Innovation in concrete structures: Design and construction*: Thomas Telford Publishing, 1999, pp. 473-487.

- [18] S. Mahmoodi and P. Sadeghian, "Self-healing concrete: A review of recent research developments and existing research gaps," in *7th International Conference on Engineering Mechanics and Materials, Laval, QC, Canada, 2019*: Canadian Society for Civil Engineering (CSCE).
- [19] C.-M. Aldea, W.-J. Song, J. S. Popovics, and S. P. Shah, "Extent of healing of cracked normal strength concrete," *Journal of materials in civil engineering*, vol. 12, no. 1, pp. 92-96, 2000.
- [20] M. Li and V. C. Li, "Cracking and Healing of Engineered Cementitious Composites under Chloride Environment," *ACI Materials Journal*, vol. 108, no. 3, 2011.
- [21] H. M. Jonkers, "Self healing concrete: a biological approach," in *Self healing materials*: Springer, 2007, pp. 195-204.
- [22] C. M. Dry, "Smart materials which sense, activate and repair damage; hollow porous fibers in composites release chemicals from fibers for self-healing, damage prevention, and/or dynamic control," in *First European conference on smart structures and materials, Glasgow, UK, 1992*, pp. 67-370.
- [23] S. White, S. Maiti, A. Jones, E. Brown, N. Sottos, and P. Geubelle, "Fatigue of self-healing polymers: multiscale analysis and experiments," presented at the 11th International Conference on Fracture 2005, ICF11, Turin, Italy, 20 - 25 March 2005.
- [24] T.-H. Ahn and T. Kishi, "Crack self-healing behavior of cementitious composites incorporating various mineral admixtures," *Journal of Advanced Concrete Technology*, vol. 8, no. 2, pp. 171-186, 2010.
- [25] Z. Yang, J. Hollar, X. He, and X. Shi, "A self-healing cementitious composite using oil core/silica gel shell microcapsules," *Cement & Concrete Composites* vol. 33, no. 4, pp. 506-512, 2011.
- [26] K. Van Tittelboom, K. Adesanya, P. Dubruel, P. Van Puyvelde, and N. De Belie, "Methyl methacrylate as a healing agent for self-healing cementitious materials," *Smart Materials and structures*, vol. 20, no. 12, p. 125016, 2011.
- [27] A. C. Balazs, "Modeling self-healing materials," *Materials today*, vol. 10, no. 9, pp. 18-23, 2007.
- [28] K. Van Tittelboom, P. Van den Heede, and N. De Belie, "Self-healing concrete with encapsulated polyurethane," in *Eco-Efficient Repair and Rehabilitation of Concrete Infrastructures*: Elsevier, 2018, pp. 429-466.
- [29] J. M. Asua, "Miniemulsion polymerization," *Progress in polymer science*, vol. 27, no. 7, pp. 1283-1346, 2002.
- [30] M. Kessler, N. Sottos, and S. White, "Self-healing structural composite materials," *Composites Part A: applied science and manufacturing*, vol. 34, no. 8, pp. 743-753, 2003.
- [31] E. N. Brown, S. R. White, and N. R. Sottos, "Retardation and repair of fatigue cracks in a microcapsule toughened epoxy composite—Part II: In situ self-healing," *Composites Science and Technology*, vol. 65, no. 15-16, pp. 2474-2480, 2005.
- [32] F. Xing *et al.*, "Self-healing mechanism of a novel cementitious composite using microcapsules," in *Proceedings of the International Conference on Durability of Concrete Structures, Hangzhou, China, 2008*, vol. 2627.
- [33] B. Dong, N. Han, M. Zhang, X. Wang, H. Cui, and F. Xing, "A microcapsule technology based self-healing system for concrete structures," *Journal of Earthquake and Tsunami*, vol. 7, no. 03, p. 1350014, 2013.
- [34] X. Wang, P. Sun, N. Han, and F. Xing, "Experimental study on mechanical properties and porosity of organic microcapsules based self-healing cementitious composite," *Materials*, vol. 10, no. 1, p. 20, 2017.
- [35] M. M. Pelletier, R. Brown, A. Shukla, and A. Bose, "Self-healing concrete with a microencapsulated healing agent," *Cem. Concr. Res*, 2011.

- [36] B. Aïssa, D. Therriault, E. Haddad, and W. Jamroz, "Self-healing materials systems: Overview of major approaches and recent developed technologies," *Advances in Materials Science and Engineering*, vol. 2012, 2012.
- [37] K. Van Tittelboom, N. De Belie, D. Van Loo, and P. Jacobs, "Self-healing efficiency of cementitious materials containing tubular capsules filled with healing agent," *Cement and Concrete Composites*, vol. 33, no. 4, pp. 497-505, 2011.
- [38] T. D. P. Thao, T. J. S. Johnson, Q. S. Tong, and P. S. Dai, "Implementation of self-healing in concrete—Proof of concept," *The IES Journal Part A: Civil & Structural Engineering*, vol. 2, no. 2, pp. 116-125, 2009.
- [39] P. Minnebo *et al.*, "A novel design of autonomously healed concrete: Towards a vascular healing network," *Materials*, vol. 10, no. 1, p. 49, 2017.
- [40] G. Anglani, P. Antonaci, S. I. C. Gonzales, G. Paganelli, and J.-M. Tulliani, "3D printed capsules for self-healing concrete applications," in *10th International Conference on Fracture Mechanics of Concrete and Concrete Structures (FraMCoS-X)*, Bayonne, France, 2019.
- [41] V. C. Li, Y. M. Lim, and Y.-W. Chan, "Feasibility study of a passive smart self-healing cementitious composite," *Composites Part B: Engineering*, vol. 29, no. 6, pp. 819-827, 1998.
- [42] E. Tsangouri, F. A. Gilabert, N. De Belie, D. Van Hemelrijck, X. Zhu, and D. G. Aggelis, "Concrete fracture toughness increase by embedding self-healing capsules using an integrated experimental approach," *Construction and Building Materials*, vol. 218, pp. 424-433, 2019.
- [43] C. Joseph, A. D. Jefferson, B. Isaacs, R. Lark, and D. Gardner, "Experimental investigation of adhesive-based self-healing of cementitious materials," *Magazine of Concrete Research*, vol. 62, no. 11, pp. 831-843, 2010.
- [44] V. C. Li and E. Herbert, "Robust self-healing concrete for sustainable infrastructure," *Journal of Advanced Concrete Technology*, vol. 10, no. 6, pp. 207-218, 2012.
- [45] H. M. Jonkers, "Bacteria-based self-healing concrete," *Heron*, vol. 56, 2011.
- [46] H. Huang, G. Ye, C. Leung, and K. Wan, "Application of sodium silicate solution as self-healing agent in cementitious materials," in *International RILEM conference on advances in construction materials through science and engineering*, 2011, pp. 530-536: RILEM Publications SARL: Hong Kong, China.
- [47] C. Dry and W. McMillan, "Three-part methylmethacrylate adhesive system as an internal delivery system for smart responsive concrete," *Smart Materials Structures*, vol. 5, no. 3, p. 297, 1996.
- [48] C. Dry, M. Corsaw, and E. Bayer, "A comparison of internal self-repair with resin injection in repair of concrete," *Journal of adhesion science technology*, vol. 17, no. 1, pp. 79-89, 2003.
- [49] A. Stewart. (March 7, 2016). *The 'living concrete' that can heal itself*. Available: <https://edition.cnn.com/2015/05/14/tech/bioconcrete-delft-jonkers/>
- [50] R. Mors and H. M. Jonkers, "Bacteria-based self-healing concrete: evaluation of full scale demonstrator projects," *RILEM Technical Letters*, vol. 4, pp. 138-144, 2019.
- [51] T. Van Mullem, E. Gruyaert, R. Caspeepe, and N. De Belie, "First large scale application with self-healing concrete in belgium: analysis of the laboratory control tests," *Materials*, vol. 13, no. 4, p. 997, 2020.
- [52] R. Davies *et al.*, "Large scale application of self-healing concrete: Design, construction, and testing," *Frontiers in Materials*, vol. 5, p. 51, 2018.
- [53] X. Zhang and C. Qian, "Engineering application of microbial self-healing concrete in lock channel wall," *Marine Georesources Geotechnology*, pp. 1-8, 2021.

- [54] T. Al-Mansoori, J. Norambuena-Contreras, R. Micaelo, and A. Garcia, "Self-healing of asphalt mastic by the action of polymeric capsules containing rejuvenators," *Construction and building materials*, vol. 161, pp. 330-339, 2018.
- [55] T. Rabczuk, J.-H. Song, X. Zhuang, and C. Anitescu, *Extended finite element and meshfree methods*. Academic Press, 2019.
- [56] T. Belytschko and T. Black, "Elastic crack growth in finite elements with minimal remeshing," *International Journal for Numerical Methods in Engineering*, vol. 45, no. 5, pp. 601-620, 1999.
- [57] J. M. Melenk and I. Babuška, "The partition of unity finite element method: basic theory and applications," *Computer Methods in Applied Mechanics and Engineering*, vol. 139, no. 1-4, pp. 289-314, 1996.
- [58] Dassault Systèmes Simulia Corp. (2017). *Abaqus documentation*.
- [59] N. Sukumar, Z. Huang, J. H. Prévost, and Z. Suo, "Partition of unity enrichment for bimaterial interface cracks," *International Journal for Numerical Methods in Engineering*, vol. 59, no. 8, pp. 1075-1102, 2004.
- [60] N. Sukumar and J.-H. Prévost, "Modeling quasi-static crack growth with the extended finite element method Part I: Computer implementation," *International Journal for Solids and Structures*, vol. 40, no. 26, pp. 7513-7537, 2003.
- [61] T. Elguedj, A. Gravouil, and A. Combescure, "Appropriate extended functions for X-FEM simulation of plastic fracture mechanics," *Computer Methods in Applied Mechanics and Engineering*, vol. 195, no. 7-8, pp. 501-515, 2006.
- [62] G. Zi and T. Belytschko, "New crack-tip elements for XFEM and applications to cohesive cracks," *International Journal for Numerical Methods in Engineering*, vol. 57, no. 15, pp. 2221-2240, 2003.
- [63] J. H. Song, P. M. Areias, and T. Belytschko, "A method for dynamic crack and shear band propagation with phantom nodes," *International Journal for Numerical Methods in Engineering*, vol. 67, no. 6, pp. 868-893, 2006.
- [64] J. J. Remmers, R. de Borst, and A. Needleman, "The simulation of dynamic crack propagation using the cohesive segments method," *Journal of the Mechanics Physics of Solids*, vol. 56, no. 1, pp. 70-92, 2008.
- [65] M. Stolarska, D. L. Chopp, N. Moës, and T. Belytschko, "Modelling crack growth by level sets in the extended finite element method," *International journal for numerical methods in Engineering*, vol. 51, no. 8, pp. 943-960, 2001.
- [66] A. Gravouil, N. Moës, and T. Belytschko, "Non-planar 3D crack growth by the extended finite element and level sets—Part II: Level set update," *International Journal for Numerical Methods in Engineering*, vol. 53, no. 11, pp. 2569-2586, 2002.
- [67] N. Moës and T. Belytschko, "Extended finite element method for cohesive crack growth," *Engineering fracture mechanics*, vol. 69, no. 7, pp. 813-833, 2002.
- [68] N. Sukumar, D. L. Chopp, E. Béchet, and N. Moës, "Three-dimensional non-planar crack growth by a coupled extended finite element and fast marching method," *International journal for numerical methods in engineering*, vol. 76, no. 5, pp. 727-748, 2008.
- [69] G. I. Barenblatt, "The mathematical theory of equilibrium cracks in brittle fracture," in *Advances in applied mechanics*, vol. 7: Elsevier, 1962, pp. 55-129.
- [70] S. A. Ponnusami, S. Turteltaub, and S. van der Zwaag, "Cohesive-zone modelling of crack nucleation and propagation in particulate composites," *Engineering Fracture Mechanics*, vol. 149, pp. 170-190, 2015.
- [71] X. Wang, "Computational technology for damage and failure analysis of quasi-brittle materials," Doctor of Philosophy, University of Manchester, 2015.
- [72] P. P. Camanho and C. G. Dávila, "Mixed-mode decohesion finite elements for the simulation of delamination in composite materials," *NASA/TM-2002-211737*, 2002.

-
- [73] L. M. Mauludin and C. Oucif, "The effects of interfacial strength on fractured microcapsule," *Frontiers of Structural and Civil Engineering*, vol. 13, no. 2, pp. 353-363, 2019.
- [74] W. Li, Z. Jiang, and Z. Yang, "Crack extension and possibility of debonding in encapsulation-based self-healing materials," *Materials*, vol. 10, no. 6, p. 589, 2017.
- [75] A. Tabiei and W. Zhang, "Cohesive element approach for dynamic crack propagation: Artificial compliance and mesh dependency," *Engineering Fracture Mechanics*, vol. 180, pp. 23-42, 2017.
- [76] W. J. Drugan and J. R. Willis, "A micromechanics-based nonlocal constitutive equation and estimates of representative volume element size for elastic composites," *Journal of the Mechanics and Physics of Solids*, vol. 44, no. 4, pp. 497-524, 1996.
- [77] S. Li and E. Sitnikova, *Representative Volume Elements and Unit Cells: Concepts, Theory, Applications and Implementation*. Woodhead Publishing, 2019.
- [78] M. Okereke and S. Keates, *Finite element applications: a practical guide to the FEM process*. Springer, 2018.
- [79] F. Gilibert, D. Garoz, and W. Van Paepegem, "Macro-and micro-modeling of crack propagation in encapsulation-based self-healing materials: Application of XFEM and cohesive surface techniques," *Materials & Design*, vol. 130, pp. 459-478, 2017.
- [80] M. S. Quayum, X. Zhuang, and T. Rabczuk, "Computational model generation and RVE design of self-healing concrete," *Frontiers of Structural and Civil Engineering*, vol. 9, no. 4, pp. 383-396, 2015.
- [81] L. Tu and D. Kruger, "Engineering properties of epoxy resins used as concrete adhesives," *Materials Journal*, vol. 93, no. 1, pp. 26-35, 1996.
- [82] A. Hillerborg, M. Mod er, and P.-E. Petersson, "Analysis of crack formation and crack growth in concrete by means of fracture mechanics and finite elements," *Cement and concrete research*, vol. 6, no. 6, pp. 773-781, 1976.
- [83] B. Hilloulin, K. Van Tittelboom, E. Gruyaert, N. De Belie, and A. Loukili, "Design of polymeric capsules for self-healing concrete," *Cement and Concrete Composites*, vol. 55, pp. 298-307, 2015.
- [84] X. Wang and A. P. Jivkov, "Combined numerical-statistical analyses of damage and failure of 2D and 3D mesoscale heterogeneous concrete," *Mathematical Problems in Engineering*, vol. 2015, 2015.

Ehrenwörtliche Erklärung

Ich erkläre hiermit ehrenwörtlich, dass ich die vorliegende Arbeit ohne unzulässige Hilfe Dritter und ohne Benutzung anderer als der angegebenen Hilfsmittel angefertigt habe. Die aus anderen Quellen direkt oder indirekt übernommenen Daten und Konzepte sind unter Angabe der Quelle gekennzeichnet.

Weitere Personen waren an der inhaltlich-materiellen Erstellung der vorliegenden Arbeit nicht beteiligt. Insbesondere habe ich hierfür nicht die entgeltliche Hilfe von Vermittlungs- bzw. Beratungsdiensten (Promotionsberater oder anderer Personen) in Anspruch genommen. Niemand hat von mir unmittelbar oder mittelbar geldwerte Leistungen für Arbeiten erhalten, die im Zusammenhang mit dem Inhalt der vorgelegten Dissertation stehen.

Die Arbeit wurde bisher weder im In- noch im Ausland in gleicher oder ähnlicher Form einer anderen Prüfungsbehörde vorgelegt.

Ich versichere ehrenwörtlich, dass ich nach bestem Wissen die reine Wahrheit gesagt und nichts verschwiegen habe.

Weimar, 03 Januar 2022

John Hanna

Academic Curriculum Vitae

John Nabil Mikhail Hanna

Institute of Structural Mechanics

Bauhaus-Universität Weimar

Marienstraße 15, 99423 Weimar, Germany

Email: john.nabil.mikhail.hanna@uni-weimar.de

Date of Birth: 27/11/1983

Place of Birth: Fayoum, Egypt

Education

- PhD: Institute of Structural Mechanics, Bauhaus-University Weimar, Germany, 2017–2022.
- M.Sc.: Master in Structural Engineering, Cairo University, Egypt, 2006 –2011.
- B.Sc.: Bachelor in Civil Engineering, Cairo University, Egypt, 2000 – 2005.

Research Interests

- Numerical modeling and Simulation, Reinforced concrete structures, Fracture mechanics, Self-healing Concrete

Publications

Published/Accepted International Journals

1. Hanna, John. 2022. "Computational Modelling for the Effects of Capsular Clustering on Fracture of Encapsulation-Based Self-Healing Concrete Using XFEM and Cohesive Surface Technique" *Applied Sciences* 12, no. 10: 5112. <https://doi.org/10.3390/app12105112>
2. John Hanna, "Accurate Computational Modeling for Impacts of Microcapsule Size and Interfacial Fracture Properties on the Fracture of Self-Healing Concrete", *International Journal of Hydromechatronics; Special Issue on Scientific Machine Learning: Application in Engineering Science*, (in press). DOI: 10.1504/IJHM.2022.10046752

International Conference/Workshop

1. John Hanna, "Computational Modeling for Effect of Crack Healing Pattern in Self-Healing Concrete", Conference Proceedings of Data Driven Computing and Machine Learning in Engineering (DACOMA-19). Advances in Computational Mechanics. Volume 4, 2019. ISSN: 1940-5820 (printed). ISSN: 1940-5839 (online abstract). China, September 2019.
2. John Hanna, "The Effects of Healed Crack Length on the Healing Efficiency of Self-Healing Concrete", International Conference on Recent Innovations in Mechanical Engineering and Civil (ICRIMEC), Dublin, Ireland, 20th Dec 2020 (Virtual Conference).
3. John Hanna, "The Effects of Fracture Energy on the Interfacial Strength of Self-Healing Concrete", 28th International Workshop on Intelligent Computing in Engineering (EG-ICE 2021), Berlin, Germany, June 30th, 2021 -July 2nd, 2021.
4. John Hanna, "Computational Modeling of Fracture in Self-Healing Concrete", International Conference on Mathematical, Computational Sciences and Management (ICMACOSCMA-21), Rome, Italy, 20th October 2021 (Virtual Conference).